# LINKAGES BETWEEN FLOW, MORPHODYNAMICS AND VEGETATION

**Dissertation**

submitted to and approved by the

Faculty of Architecture, Civil Engineering and Environmental Sciences
Technische Universität Braunschweig

and the

Department of Civil and Environmental Engineering
University of Florence

in candidacy for the degree of a
**Doktor-Ingenieurin (Dr.-Ing.) /**
**Dottoressa di Ricerca in Civil and Environmental Engineering**[*)]

by

Giada Artini
born 25 March 1991
from Montevarchi, Italy

| | |
|---|---|
| Submitted on | 11 September 2023 |
| Oral examination on | 20 November 2023 |
| Professorial advisors | Prof. Dr.-Ing. Jochen Aberle<br>Prof. Dr.-Ing. Luca Solari |

**2024**

*) Either the German or the Italian form of the grade may be used.

## Abstract

Over the past decades, the significant role of riparian vegetation in enhancing water quality and supporting biological diversity has gained increasing recognition. As a result, recent river management strategies have incorporated vegetation for various purposes, including flood mitigation, soil resistance enhancement, while pursuing ecological improvement in fluvial environments. Riparian areas are typically colonized by a wide variety of vegetation species and types, including woody trees, bushes, and shrubs. The presence of vegetation has a significant impact on the flow field, playing a key role in shaping river morphological evolution. The stems, branches, and leaves of riparian vegetation alter the flow dynamics, modify turbulence patterns, and affect bed shear stress and sediment processes. These vegetation-induced effects are further expected during overbank flows and floods, as the threshold for sediment mobility is often exceeded, resulting in dynamic changes to bedforms, bars, and channels. The combined influences of flow dynamics, sediment transport, and vegetation create a complex interplay within river environments. Understanding these intricate interactions is of utmost importance for accurately modeling the morphological evolution of channels and implementing effective management strategies for river environments.

This thesis is based on experimental activities conducted to investigate the flow dynamics and sediment transport characteristics in river environments featuring leafy flexible vegetation and large-scale bedforms. The experimental setup encompasses both mobile-bed and fixed-bed conditions, representing the final morphology of mobile-bed scenarios, enabling a novel analysis of flow characteristics, turbulent fields, and resistance composition in the different conditions. The obtained results highlight the notable influence of leafy flexible vegetation on controlling bedform geometry and sediment transport processes. Surprisingly, contrary to previous studies, the data demonstrate that the presence of vegetation increases dune celerity, consequently enhancing sediment transport. This effect is likely attributed to the increased turbulence caused by the presence of leaves. To model this process, a turbulence-based model for predicting

bed-load transport is corrected using the new dataset. Under mobile-bed conditions, this study reveals deviations from the linear superposition principle of the hydraulic resistance in setups incorporating leafy plants. This indicates the introduction of non-linear effects in the combined contribution of dune and vegetation form drag to the overall flow resistance. Accordingly, in fixed-bed conditions, direct measurements of the hydraulic forces exerted by both dunes and leafy flexible plants yield similar results, confirming the initial hypothesis.

This study demonstrates that the presence of leafy flexible vegetation significantly influences the hydrodynamics and morphodynamics of river systems, affecting bedform geometry and sediment transport processes. These findings deepen the understanding of the intricate interactions among flow, sediment transport, and vegetation within river environments, offering valuable insights for the development of improved river management strategies. A crucial aspect of this advancement involves the abandonment of rigid cylinder models in favor of more realistic representations of flexible vegetation.

# Zusammenfassung

In den letzten Jahrzehnten rückte die Signifikanz der Rolle von Vorlandvegetation zur Verbesserung der Wasserqualität und der biologischen Vielfalt in Fließgewässern immer mehr in den Vordergrund. Im Rahmen von aktuellen Flussmanagementstrategien wird Vegetation deshalb einerseits zur Verbesserung des ökologischen Zustands, andererseits aber auch zum Hochwassermanagement, z.B. in Auengebieten, oder auch zur Stärkung der Bodenresilienz genutzt. Vorländer werden in der Regel von einer Vielzahl von Pflanzenarten und -typen besiedelt, darunter Laubbäume und Büsche, die wiederum eine wichtige Rolle für die morphologische Entwicklung von Fließgewässern spielen. Die Stämme, Äste und Blätter der Vorlandvegetation beeinflussen die Strömungsdynamik, modifizieren Turbulenzmuster und haben Auswirkungen auf die Sohlenschubspannung und somit den Feststofftransport. Diese Effekte sind insbesondere bei Hochwasserereignissen von Bedeutung, d.h. wenn der Strömungsangriff großgenug ist um die Sohlensedimente in Bewegung zu setzen, sodass sich Transportkörper, Bänke und Abflusskanäle dynamisch verändern. Das verbesserte Verständnis der komplexen Interaktionen zwischen Strömungsdynamik, Feststofftransport und Vegetation auf Vorländern ist deshalb von größter Bedeutung für die Modellierung der morphologischen Entwicklung von Fließgewässern und somit für die Umsetzung wirksamer Managementstrategien unter Berücksichtigung ökologischer, hydrodynamischer und sedimentologischer Aspekte. Durch einen integrativen Ansatz lassen sich nachhaltige Lösungen für den Schutz und die Entwicklung von Flussökosystemen entwickeln.

Die vorliegende Arbeit basiert auf gegenständlichen Modelluntersuchungen, die mit dem Ziel durchgeführt wurden, die Strömungsdynamik und den Feststofftransport in Fließgewässern mit belaubter flexibler Vegetation unter Berücksichtigung des zusätzlichen Einflusses von großen Sohlenformen (Dünen) zu untersuchen. Der experimentelle Aufbau umfasste sowohl bewegliche als auch feste Sohlen, wobei die letzteren den Endzustand der Sohlenmorphologie der Versuche mit beweglicher Sohle darstellten. Die gewählte Vorgehensweise ermöglichte eine neuartige Analyse des turbulen-

ten Strömungsfeldes und des Widerstandsverhaltens von Vorländern unter der Berücksichtigung von verschiedenen Randbedingungen. Die erzielten Ergebnisse unterstreichen den Einfluss von belaubter flexibler Vegetation auf die Dünengeometrie und die Feststofftransportprozesse. Im Gegensatz zu früheren Studien zeigen die Ergebnisse, dass belaubte flexible Vegetation die Wandergeschwindigkeit von Dünen erhöhen und somit den Geschiebetransport verstärken kann, was auf die erhöhte Turbulenz infolge der Blätter zurückgeführt werden kann. Zur Modellierung dieses Prozesses wurde deshalb ein auf Turbulenzparametern basierender Ansatz zur Bestimmung des Geschiebetransports unter Verwendung des neuen Datensatzes weiterentwickelt. Im Fall von mobilen Sohlen mit belaubter flexibler Vegetation zeigten sich Abweichungen vom linearen Superpositionsprinzip zur Erfassung des hydraulischen Widerstands infolge der Oberflächenreibung, Dünen und Vegetation, was auf nichtlineare Effekte in Bezug auf den Formwiderstand von mobilen Dünen und Vegetation zurückgeführt wurde. Diese konnten durch mit festen Sohlen durchgeführte direkte Messungen der Widerstandskräfte von Dünen und belaubten flexiblen Pflanzen untermauert werden.

Die Arbeit verdeutlicht eindrücklich, dass belaubte flexible Vegetation die Hydro- und Morphodynamik von Fließgewässern erheblich beeinflusst und somit auch die Transportkörpergeometrie und die Feststofftransportprozesse verändert. Die gewonnen Erkenntnisse tragen zu einem besseren Verständnis der komplexen Interaktionen zwischen Strömung, Feststofftransport und Vegetation in Fließgewässern bei und bieten wertvolle Einblicke, die für die Entwicklung verbesserter Managementstrategien von Vorländern von Bedeutung sind. Ein entscheidender Aspekt dieser Weiterentwicklung beinhaltet die Empfehlung, in zukünftigen Untersuchungen Vorlandvegetation nicht wie bisher oftmals üblich durch starre Zylinder zu modellieren, sondern durch flexible Vegetationselemente.

# Contents

# List of Figures

# List of Tables

# List of Symbols

| | | |
|---|---|---|
| $\langle\rangle$ | horizontal-averaged | |
| $\langle\rangle_z$ | horizontal- and vertical-averaged | |
| $A_L$ | one-sided leaf area | $(m^2)$ |
| $A_s$ | stem and blossom frontal area | $(m^2)$ |
| $A_p$ | frontal projected area | $(m^2)$ |
| $A_{SP}$ | shear plate head plate area | $(m^2)$ |
| $a = \langle\overline{a}\rangle_z$ | depth-averaged frontal area per unit volume | $(m^{-1})$ |
| $aH$ | roughness density | $(-)$ |
| $C_D$ | drag coefficient | $(-)$ |
| $c'_f$ | grain-related resistance coefficient | (-) |
| $c_{f,b}$ | total bed resistance coefficient | (-) |
| $c_{f,d}$ | dune-related resistance coefficient | (-) |
| $c''_{f,T}$ | total resistance coefficient | (-) |
| $c''_{f,v}$ | vegetation-related resistance coefficient | (-) |
| $c_m$ | measured celerity | $(m/s)$ |
| $D_X$ | X% pass particle size | (m) |
| $D^*$ | $D_{50}\left[(s-1)g/\nu^2\right]^{1/3}$ particle parameter | (-) |
| $d_e$ | equivalent diameter | $(m)$ |
| $DFS$ | drag force sensor | |
| $F_D$ | drag force | (N) |
| $F_{SP}$ | force measured by SP | (N) |
| $F_{DFS}$ | force measured by DFS | (N) |
| $g$ | gravity acceleration | $9.81 m/s^2$ |
| $H$ | water depth | (m) |
| $h_p$ | plant height | (m) |

| | | |
|---|---|---|
| $k_t$ | turbulent kinetic energy | $(m^2/s^2)$ |
| $k_t^*$ | dimensionless turbulent kinetic energy | $(-)$ |
| $LAI$ | Leaf Area Index | (-) |
| $l_t$ | integral length scale | (m) |
| $m$ | plant density | $\#plants/m^2$ |
| $Q_{s,m}$ | measured sediment transport rate | (g/s) |
| $Q_{s,p}$ | predicted sediment transport rate | (g/s) |
| $q_s$ | volumetric sediment transport rate per unit width | $(m^2/s)$ |
| $q_s^*$ | dimensionless sediment transport rate per unit width | (-) |
| $R_b$ | bed-related hydraulic radius | (m) |
| $R_h$ | hydraulic radius | (m) |
| $R_p$ | $D_{50}\sqrt{(s-1)gD_{50}}/\nu$ particle Reynolds number | (-) |
| $s$ | $\rho_s/\rho$=2.65 specific or relative density | (-) |
| $s-1$ | $(\rho_s-\rho)/\rho$ submerged specific gravity of sediment | (-) |
| $S_b$ | bed slope | (%) |
| $S_E$ | energy slope | (%) |
| $S_{WSE}$ | water surface elevation slope | (%) |
| $SP$ | shear plate | |
| $T$ | $[(u'_*)^2-(u'_{*,cr})^2]/(u'_{*,cr})^2$ transport parameter | (-) |
| $U$ | channel-averaged velocity | (m/s) |
| $\langle\overline{u}\rangle_z$ | depth-averaged double-averaged velocity | (m/S) |
| $u'_*$ | grain-related friction velocity | (m/s) |
| $u_c$ | uncertainty | |
| $V_p$ | plant volume | $(m^3)$ |
| $W$ | flume width | (m) |
| $\omega_0$ | particle fall velocity | (m/s) |
| $\chi$ | Vogel coefficient | (-) |
| $\lambda_{crest}$ | dune wavelength | (cm) |
| $\Delta_\sigma$ | dune height | (cm) |
| $\kappa$ | von Karman constant | |
| $\phi$ | solid volume fraction | (%) |
| $\mu$ | water dynamic viscosity | $10^{-3}(Pas)$ |
| $\nu$ | $=\mu/\rho$ water kinematic viscosity | $10^{-6}(m^2/s)$ |
| $\rho$ | water density | $1000kg/m^3$ |
| $\rho_s$ | sediment density | $2650kg/m^3$ |
| $\sigma_g$ | geometric standard deviation | (-) |

| | | |
|---|---|---|
| $\tau$ | total fluid stress | (Pa) |
| $\tau_0$ | total boundary shear stress | (Pa) |
| $\tau_b$ | bed shear stress | (Pa) |
| $\tau_*$ | $\tau/(\rho_s - \rho)gD_{50}$ Shields number | (-) |
| $\tau'$ | skin friction | (Pa) |
| $\tau''$ | total form drag | (Pa) |
| $\tau''_v$ | vegetation-related form drag | (Pa) |
| $\tau''_d$ | dune-related form drag | (Pa) |
| $\tau_{SP}$ | form drag associated with SP measurements | (Pa) |
| $\tau_{DFS}$ | form drag associated with DFS measurements | (Pa) |
| $\tau_{EH}$ | result of Engelund and Hansen (1967) | $\tau' + \tau''_d$ |
| $\tau_{VR}$ | result of van Rijn (1984b) | $\tau' + \tau''_d$ |

# Chapter 1

# Introduction

The term "riparian" refers to zones that are characterized by their close proximity to rivers, representing the interface between aquatic and terrestrial ecosystems (Figure 1.1). These areas provide important habitat and refugia for a large variety of plant and animal species, supporting high levels of biological diversity and contributing to the overall ecological health of river systems. Particularly, vegetation, being an ubiquitous element in river systems, acts as a natural filter, absorbing pollutants and improving water quality (Rowiński et al., 2018; Yager and Schmeeckle, 2013)

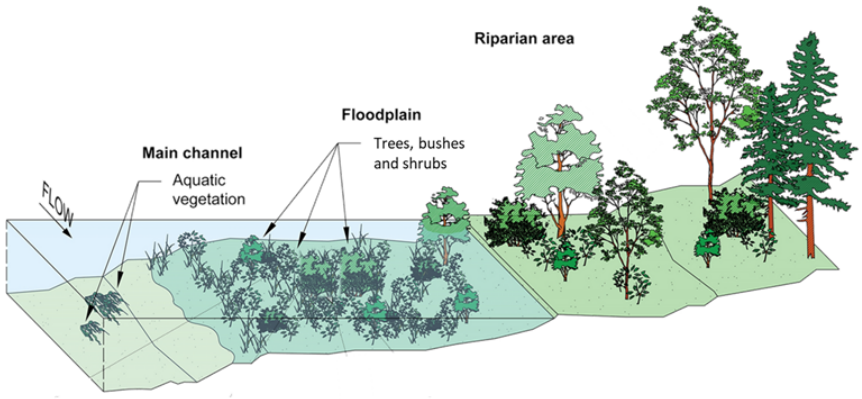


Figure 1.1: Riparian floodplains experience periodic inundation during high-flow events (modified from Caroppi et al. (2022)).

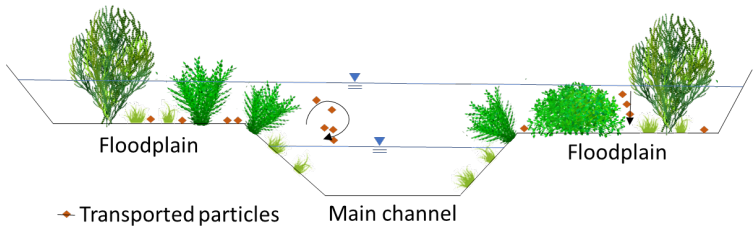


Figure 1.2: Schematization of two-stage channel (adapted from Rowiński et al. (2018); Västilä and Järvelä (2018))

Historically, riparian vegetation was commonly perceived negatively due to its connection with increased hydraulic resistance. This perception led to concerns about elevated flooding levels and reduced channel conveyance. Consequently, vegetation removal was frequently practiced. However, in recent years, there has been a significant shift towards sustainable river restoration projects in response to the growing awareness of environmental degradation. Particularly in Europe, the Water Framework Directive (2000) has played a pivotal role in promoting the enhancement of ecological status for water bodies. As a result, there has been a renewed focus on incorporating vegetation as a fundamental element in these projects to achieve multiple objectives, such as flood mitigation, terrain resilience enhancement, and ecological restoration within fluvial environments.

Straightened channels and drainage ditches are often characterized by a compound (two-stage) geometry. The main channel is designed to convey low flows, while floodplains are inundated at higher discharges, providing flood capacity. In these areas, the presence of vegetation plays a crucial role in retaining suspended sediments and nutrients, enhancing water quality (Figure 1.2); (Rowiński et al., 2018).

Natural rivers exhibit different planforms, such as braided and meandering patterns, whose development depends on the transport, deposition, and erosion of sediments. During periods of low-flow, deposition of alluvial soil leads to the formation of floodplains and sediment deposits (i.e., river bars) in the inner side of a bend, providing a substrate for ecosystem development (van Dijk, 2013; Richardson et al., 2007).

The dynamic equilibrium of rivers is strongly influenced by vegetation,

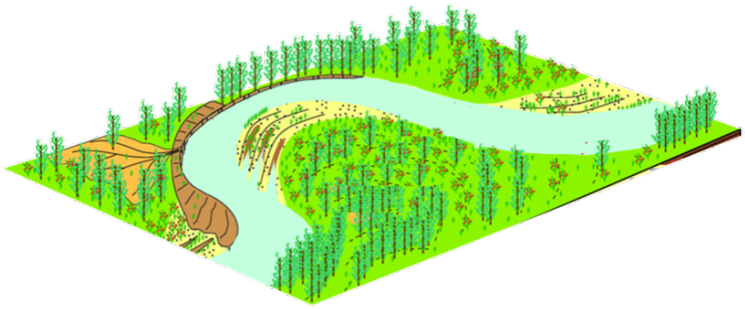

Figure 1.3: Floodplain schematization of a meandering river section. Modified from van Dijk (2013).

which controls erosion on the outside of bends, limits excessive sediment transport, and facilitates the growth and development of bars (Figure 1.3); (Tal and Paola, 2007).

Thus, the colonization of bare areas by vegetation profoundly alters the overall morphological evolution of river systems (Camporeale et al., 2013).

Moreover, vegetation is commonly used as a treatment system in drainage channels, mitigating pollution contamination and enhancing ecosystem quality (Västilä and Järvelä, 2018). The efficiency of drainage systems depends on the interconnected linkages between vegetation, flow, and sediment, which determine the crucial hydraulic parameters for their effectiveness.

During overbank flows and floods, the threshold for sediment mobility is commonly surpassed in sandy rivers, resulting in the mobilization of sediments (Figure 1.4); (Lightbody et al., 2019). This mobilization may lead to the formation of periodic undulations at the sand bottom, i.e., bedforms, such as dunes and ripples, which result from the interaction between the flow and the mobile sand bed. The shape and celerity of these bedforms serve as indicators for sediment transport rates (Lokin et al., 2022; Naqshband et al., 2017; Aberle et al., 2012). Therefore, modeling and predicting river dune dynamics play a crucial role in accurately assessing flow resistance, water levels, sediment processes, and consequently the overall morphological evolution of a channel.

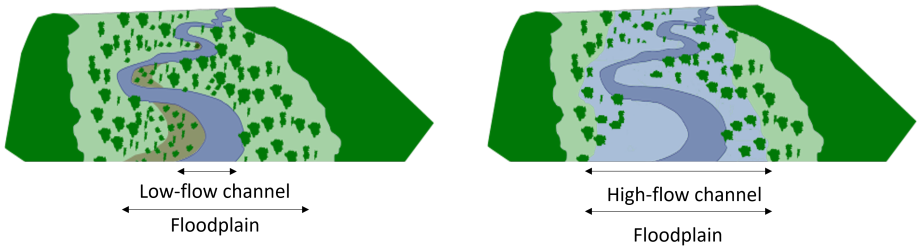


Figure 1.4: Schematization of a river section in low-flow and high-flow condition.

## 1.1 Motivation

During the last years, the impact of climate change on extreme events has become increasingly evident, with projections indicating a rise in both their frequency and intensity. Thus, river dynamics and drainage systems are increasingly impacted by these extreme events. This increased vulnerability highlights the need for a deeper understanding of the interactions between flow, vegetation, and sediment processes in river systems. Through a comprehensive understanding of these intricate relationships, the ability to forecast and mitigate the effects of floods on riparian areas may be enhanced, also enabling a better control over the overall morphological evolution of a channel.

Despite this increased recognition of the importance of vegetation, the current understanding of the intricate interactions among flow, vegetation, and sediment in river systems remains limited. Consequently, the ability to accurately predict and comprehend the responses of river systems to environmental changes is hindered.

It is crucial to highlight the need for in-depth studies that investigate the interconnected relationships among flow, bedforms, and vegetation in river environments. These three elements are vital components of the intricate system that defines river function (Gurnell, 2014), and understanding their interplay is of fundamental importance in gaining critical insights into the morphological evolution of river channels. On one hand, the presence and characteristics of vegetation alter flow velocity and direction, impacting sediment transport and consequently the formation and

stability of bedforms (Branß et al., 2022; Vargas-Luna et al., 2019). On the other hand, the geometry and evolution of these bedforms also influence local flow conditions and increase hydraulic roughness (van Rijn, 1984b), which, in turn, govern the transport of sediment. The interplay among flow, bedforms, and vegetation dictates the patterns of sediment erosion, transport, and deposition and thus the overall topography of the river system. This knowledge is indispensable for practical applications, such as managing riverbed composition, mitigating erosion, and safeguarding infrastructure.

Climate-induced changes in precipitation patterns and river flow regimes have the potential to disrupt the equilibrium of these systems (O'Briain, 2019). A complete understanding of these interconnections is fundamental for developing adaptive strategies to mitigate the adverse impacts of climate change.

The general aim of this research is to advance the understanding of morphodynamic processes in natural fluvial environments considering realistic vegetation model and bedform geometries. This thesis specifically aims to investigate scenarios where floodplains and sediment deposits are covered by leafy flexible plants, such as shrubs and bush vegetation, during high-flow events, when sediment is prone to motion. After exploring the actual knowledge gaps and defining the research questions that serve as the foundation for this research (Chapter 2), this study has been built upon a series of laboratory experimental activities conducted under both mobile and fixed bed conditions. It delves into the influence of varying plant leaf mass on morphodynamics and dune characteristics in mobile bed conditions (Chapter 3). Additionally, experiments conducted under fixed bed conditions, where the topography replicated that observed in mobile-bed conditions, provide an innovative opportunity to compare flow field and turbulence characteristics with the results obtained from mobile-bed experiments (Chapter 4). Furthermore, hydraulic forces from vegetation and dunes were independently measured to comprehend the distribution of flow resistance in scenarios where both exist (Chapter 5).

# Chapter 2

# Background

This chapter presents a summary of the theoretical background on hydrodynamics in vegetated channel (Section 2.1), over dunes (Section 2.2), turbulence-based bed-load model (Section 2.3), and flow resistance prediction (Section 2.4), while emphasizing the existing gaps in the current understanding. Furthermore, a detailed literature review is elaborated in the subsequent chapters, with a particular focus on the specific topics.

## 2.1 Hydrodynamics in Vegetated Channels

Vegetation that grows in riparian areas is usually classified using a depth-related vertical zonation (Hoppenreijs et al., 2022; Aberle and Järvelä, 2015). Aquatic vegetation, such as macrophytes, grows under the water surface (Calvani et al., 2022). Amphibious vegetation occupies the transition zone between terrestrial and aquatic environments. Emergent vegetation refers to plants rooted in shallow water but protruding through the water surface. Woody trees, shrubs, bushes, and grassy vegetation commonly grow between low- and high-water marks (Aberle and Järvelä, 2015), being influenced by flow interactions only during overbank flows.

Riparian vegetation can be categorized as either flexible, including grasses and shrubs, or rigid, such as woody species. For submerged flexible vegetation, the process of reconfiguration is referred to the mechanism by which vegetation adjusts its shape, frontal area, and size in order to

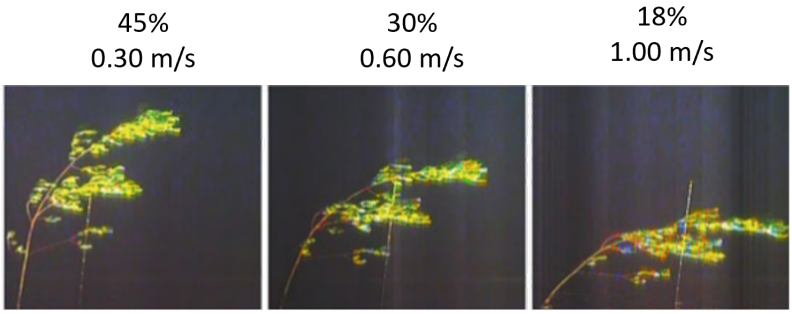


Figure 2.1: Frontal area shares (in percentage) of a submerged flexible willow at different flow velocity, from experiments conducted by Jalonen and Järvelä (2014) (modified from Aberle and Järvelä (2015)).

attain a balance between the drag force and the restoring force associated with its stiffness (Figure 2.1). As the flow velocity increases, submerged flexible plants undergo a notable transformation. They transition from an upright position to a gentle swaying motion, then progress to a coherent wavying motion, and ultimately become prone. This coherent waving, known as the "monami," occurs in response to the passage of vortices. The waving action helps reduce drag within the canopy, enabling higher velocities and turbulent stresses within it (Ghisalberti and Nepf, 2009). The prone position is predominantly observed in the presence of grassy vegetation and highly flexible aquatic plants (Kouwen et al., 1981).

Vegetation-related flow resistance depends on hydraulic parameters such as water depth and flow velocity, as well as specific plant characteristics including density, rigidity/flexibility, and submerged/emergent conditions (Aberle and Järvelä, 2013; Nepf and Vivoni, 2000). The morphology of vegetation exerts a significant influence on velocity profiles shape: uniform vegetation density along the vertical direction leads to a uniform velocity distribution. On the contrary, if the density of vegetation varies along the vertical direction, it leads to more complex velocity profiles due to the different resistance imposed at different layers (Lightbody and Nepf, 2006; Aberle et al., 2011).

The presence of vegetation significantly impacts velocity profiles and turbulence intensities deviating from those related to flows over bare beds

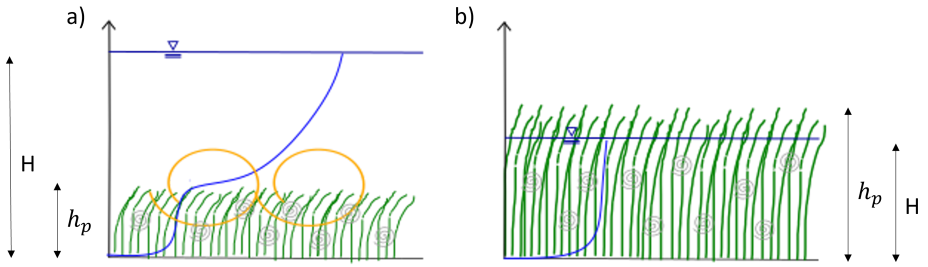


Figure 2.2: Velocity profiles (blue curve) for a) submerged and b) emergent vegetation. As the relative submergence decreases, the turbulence scale shifts from predominantly shear-generate to wake-generated (modified from Nepf and Vivoni (2000)).

(Yager and Schmeeckle, 2013; Nepf and Vivoni, 2000; Aberle et al., 2011; Afzalimehr et al., 2019; Caroppi et al., 2022). Particularly, vegetation plays a crucial role in generating coherent flow structures that impact the flow field at various scales, ranging from leaf-scale to channel-scale (Nepf, 2012; Aberle and Järvelä, 2015).

The velocity distribution and turbulence field within a vegetation canopy vary according to ratio between water depth $H$ and plant height $h_p$, namely relative submergence (Figure 2.2).

In submerged conditions ($H/h_p > 1$), the flow within vegetation is characterized by zones of reduced velocity within the vegetation and a high-velocity zone above it. This velocity gradient gives rise to a shear layer at the top of the vegetation canopy, which enhances vertical momentum exchange. At the interface between the vegetation canopy and the flow, Kelvin-Helmholtz instabilities generally arise, governing the vertical transport processes within the channel at canopy scale (Beudin et al., 2017). The intensity of the momentum absorption is determined by the canopy density, commonly defined as the product of drag coefficient ($C_D$), frontal area per unit volume ($a$), and plant height ($h_p$). In cases of dense vegetation with a high value of $C_D a h_p$ (greater than 0.1), significant momentum absorption occurs at the shear layer, resulting in an inflection point in the velocity profile at the top of the canopy. On the other hand, sparse vegetation with a lower value of $C_D a h_p$ (much

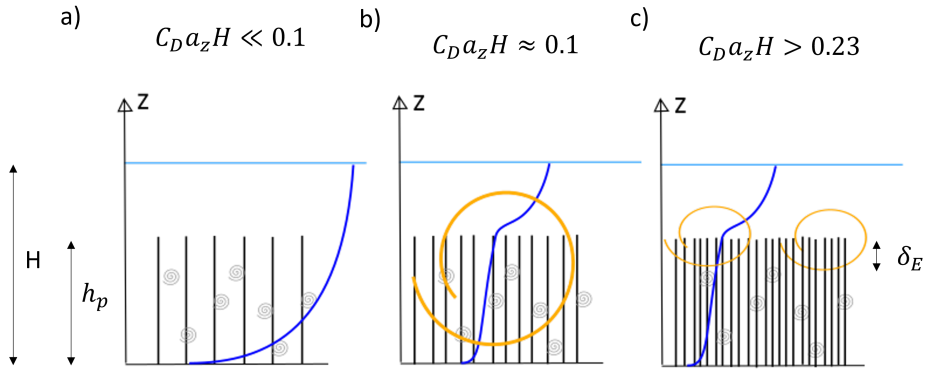


Figure 2.3: Velocity profiles in sparse and dense canopy (according to Nepf (2012); adapted from Aberle and Järvelä (2015)). Blue profile represent velocity distribution. Grey vortices represent stem wake turbulence, while orange eddies represent Kelvin-Helmholtz instabilities.$\delta_E$ is the penetration depth of these instabilities.

less than 0.1), characterized by lower momentum exchange, typically exhibits a turbulent boundary profile. For vegetation with an intermediate, $0.1 < C_D a h_p < 0.23$, the flow structure demonstrates transitional characteristics between two distinct conditions. In this range, the canopy-scale Kelvin-Helmholtz instabilities penetrate the bed dominate and influence the turbulence pattern within the entire canopy region. However, as the canopy density increases beyond $C_D a h_p > 0.23$, the penetration depth of these instabilities $\delta_E$ towards the bed gradually decreases (Nepf and Vivoni, 2000). Nepf et al. (2007) reported that $\delta_E$ is inversely proportional to the drag length scale of the canopy $(C_D a)^{-1}$. In emergent conditions $(H/h_p \leq 1)$, the velocity profile exhibits a shape that is independent of the relative submergence but is strongly influenced by density, similar to the case of submerged vegetation. However, in emergent conditions, the velocity profile is not influenced by free-stream effects (Aberle and Järvelä, 2015; Nepf, 2012).

Characterizing natural vegetation for hydraulic analyses is challenging because plants consist of various components such as branches and leaves, creating a heterogeneous structure (Västilä and Järvelä, 2014; Wu and He, 2009). Several studies have emphasized the significance of leaves in

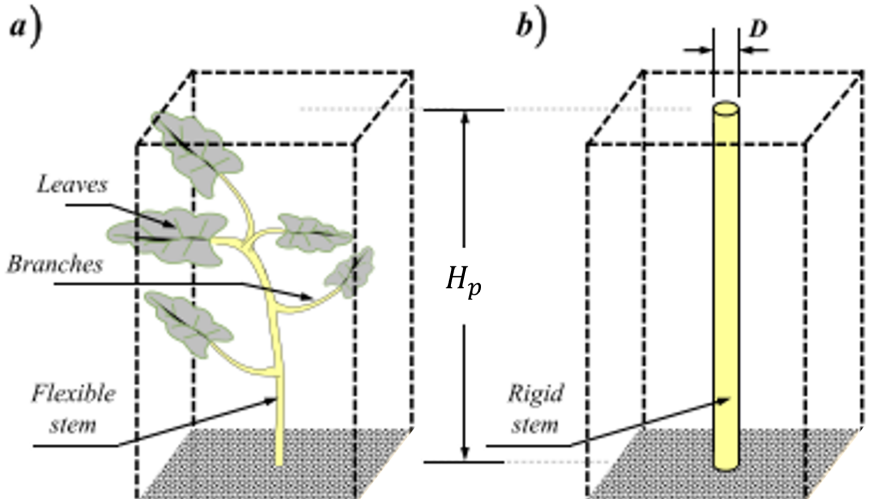


Figure 2.4: Vegetation model types: a) flexible; b) rigid (modified by Vargas-Luna et al. (2015)).

determining the flow resistance of leafy vegetation (Jalonen et al., 2013; Aberle and Järvelä, 2013). As a result, Leaf Area Index (LAI), defined as the total one-sided leaf area per unit bed area, is increasingly being employed as a measure of vegetation density in estimating flow resistance (Västilä and Järvelä, 2018).

However, most of the models to predict the vegetative drag were developed within laboratory studies and their application in the field is not straightforward (Armanini et al., 2005). Experimental studies frequently employ simplified vegetation models to investigate the flow field in vegetated channels. In nature, plants canopy can exhibit a diverse range of spatial density, foliage stage, height, branch structure, and vertical variations in morphology. Additionally, the overall drag force is influenced by the spacing and arrangement of plants (Tanino and Nepf, 2008a; Schoneboom, 2011). However, in river modeling, vegetation is often simplified and represented as an array of uniform rigid cylinders that are uniformly distributed (Vargas-Luna et al., 2015; Aberle and Järvelä, 2015) (Figure 2.4).

Rigid stems exhibit hydraulic behaviors that differ from those of nat-

ural vegetation. Unlike rigid vegetation, flexible vegetation undergoes a dynamic reconfiguration process in response to the flow (Nepf, 2012). In natural environments, vegetation often comprises leafy plants that exhibit complex and varied shapes, which cannot be accurately represented by simple cylindrical models (Caroppi et al., 2021; Aberle and Järvelä, 2015).

To date, only few studies considered natural-like leafy vegetation (Caroppi et al., 2019; Tang et al., 2020; Jalonen et al., 2013; Schoneboom and Aberle, 2009). Most of the studies investigating the effects of vegetation on the flow field have primarily focused on vegetation represented by rigid cylinders or regular flexible blades (Ghisalberti and Nepf, 2006; Huai et al., 2019; Tanino and Nepf, 2008a; Le Bouteiller and Venditti, 2015; Xu and Nepf, 2020; Lei and Nepf, 2021; Yang and Nepf, 2018). For this reason, there is a pressing need to expand the understanding of the effects of leafy vegetation on flow dynamics by moving away from the simplified rigid cylinder approach and adopting more realistic models.

## 2.2 Hydrodynamics over River Dunes

Under steady flow conditions, a plane sand bed is unstable and tends to exhibit undulations in its surface. The formation and growth of these bedforms are influenced by the bed shear stress and the Froude number ($Fr$). As the Froude number increases, small ripples initially form, which then transition into larger dunes. As the stream power further increases, the dunes tend to flatten, resulting in a plane bed configuration (washing out of the dune). The evolution of bedforms for increasing bed shear stress is commonly represented in form of stability diagrams that differs for the considered hydraulic parameters and sediment transport capability of the flow, such as flow velocity, grain size or Shields parameter (Van den Berg and van Gelder, 1993; Southard and Boguchwal, 1990; Simons and Richardson, 1961; Allen, 1985).

Generally, dunes controlled by bed load are asymmetric with low-angled stoss-side and steep lee-side, while dunes generated in flows dominated by suspended sediment transport are more symmetric (Naqshband, 2014). Flow over an asymmetric dune separates at the crest generating a turbulent shear layer dominated by Kelvin-Helmholz structures that even-

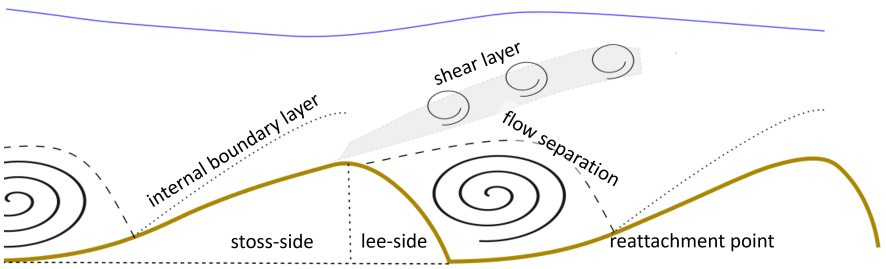


Figure 2.5: Structure of flow over dune (adapted from Naqshband (2014); Best (2005)).

tually dissipate downstream. The flow reattachment point is usually located at 4-6 dune heights downstream of the crests (Best, 2005; Dey et al., 2020). From here, a boundary layer grows along the stoss side toward the next crest. The pressure gradient between the high-pressure stoss side and low-pressure lee side produces form drag, which controls hydraulic resistance in flows over dunes (Best, 2005; Maddux et al., 2003b).

Dunes migrate downstream, exhibiting a bed-surface profile that is out-of-phase with the free surface (Simons and Richardson, 1966; Engelund and Fredsoe, 1982). The flow velocity accelerates on the stoss-side of the dune, transporting bed grains up to the crest. Once reaching the crest, the sediment deposits on the steep lee-side, leading to the downstream migration of the dune (Heydari et al., 2014; Ferraro and Dey, 2015). The stoss-side of the dune features zones with positive mean vertical velocity, while the lee-side is characterized by zones with negative mean vertical velocity. The areas of highest turbulence intensities are primarily concentrated between the lower lee-side and the reattachment point of the flow separation zone in asymmetric dunes (Dey et al., 2020; Best and Kostaschuk, 2002).

Over the past years, numerous studies have focused on the flow dynamics over fixed two-dimensional dunes, providing important insights into flow structure and the turbulence field over such bedforms (Best,

2005; Bennett and Best, 1995; Mendoza and Wen Shen, 1990 and references therein). Lyn (1993) studied turbulence over 2D fixed dunes and reported that the near-bed turbulence characteristics are influenced by the dune geometry. Moreover, Bennett and Best (1995) studied the turbulence structure over a 2D fixed dune and found that the highest turbulence intensity occurs in the separation zone along the shear layer between the recirculating flow and the free flow. This phenomenon is associated with the frequent occurrence of Kelvin-Helmholtz instabilities, which are also responsible for the generation of large-scale eddies. In a study conducted by Venditti and Bennett (2000), measurements of velocity fluctuations and suspended sediment flux were performed over fixed 2D dunes. The findings highlighted that the flow separation zone and the shear layer formed at the dune crest are the primary sources of turbulence.

However, insufficient attention has been given to the turbulent flow patterns occurring over three-dimensional bedforms. Allen (1968)'s seminal work remains the most comprehensive examination of near-bed flow behavior in the context of 3D bedforms. Allen (1968) effectively elucidated the intricacies inherent in the flow patterns over 3D bedforms and emphasized the significant influence exerted by near-bed flow characteristics, particularly flow separation patterns, on sediment transport phenomena. In fact, 2D dunes exhibit a simpler shape with aligned parallel crests and troughs, while 3D dunes possess a more complex shape characterized by inclined profiles and a shield-like morphology. Significant advancements in this field have been achieved by Maddux et al. (2003b,a), who conducted an extensive investigation of the flow field over sinusoidal fixed dunes. Their research findings demonstrated that quasi-3D bedforms exhibit higher resistance compared to their 2D counterparts. Turbulence levels within these sinusoid bedforms were significantly reduced due to the form-induced stresses resulting from secondary flow circulations (Venditti, 2007).

Venditti et al. (2005) claimed that all 2D bedforms observed in flume studies have the potential to evolve into 3D geometries given a sufficient amount of time. It is crucial to acknowledge that the results obtained from studying 2D fixed dunes may not fully capture the intricate characteristics exhibited by natural river bedforms that generally present a 3D

geometry (McLean et al., 2008; Venditti, 2007; Maddux et al., 2003b,a). Furthermore, most of the experimental studies conducted on fixed dunes have overlooked the alterations in flow structure caused by bed mobility (Hanmaiahgari and Balachandar, 2016). Nikora and Goring (2000) demonstrated that the flow structure over a sediment bed with weakly bed load significantly differs from that on a fixed bed due to distinct boundary conditions. Bridge and Best (1988) reported an increase in streamwise turbulence intensities near the bed on the lee-side during the washing out of the dune. Additionally, Schindler and Robert (2005) observed that suspended sediment transport increases during the transition from ripples to dunes, attributed to the generation of separation zones and shear layer turbulence.

Nevertheless, only a few works focused on measurements of flow and turbulence characteristics over mobile 3D bedforms. Hanmaiahgari and Balachandar (2016) measured velocity and turbulence fields over non-equilibrium mobile 3D dunes. The authors observed that streamwise turbulence intensities near the bed were twice as high as transverse turbulence intensities, and transverse turbulence intensities were, in turn, twice as high as vertical turbulence intensities. Additionally, the authors noted that the region encompassing the trough and the reattachment point exhibited peak values of turbulent kinetic energy and Reynolds stresses. Furthermore, another important finding from their research was the increase in turbulence anisotropy with the size of mobile bedforms. The anisotropy was observed to extend up to the free surface, indicating that the entire depth of the flow is disturbed by the presence of mobile dunes.

As a result, there is a noticeable gap of knowledge about the intricate interplay between 3D mobile bedforms and the associated flow and turbulence fields. Specifically, there is a lack of studies that focus on investigating the effective changes occurring in flow and turbulence fields between mobile and fixed 3D dunes. Enhancing the comprehension of these effective changes is essential for gaining a deeper understanding of the associated hydro-morphological phenomena.

## 2.3 Sediment Transport in Presence of Vegetation and Bedforms

Bed load transport occurs when the value of the bed-shear exceeds the critical threshold for the incipient motion of sediment (critical Shields parameter), causing sediment particles to begin rolling and saltation along the bed (van Rijn, 1984a). Classical bed load transport models in river systems are based on time-averaged bed shear stress. However, various authors have adopted different approaches in their studies to investigate sediment transport. Some researchers have placed emphasis on the influence of gravity forces as the primary driving mechanism (van Rijn, 1984a; Bagnold, 1973), while others have recognized the intermittent nature of bed load transport, which is associated with turbulent fluctuations (Einstein, 1950). Among the numerous models available, the van Rijn (1984a) model is widely utilized for estimating bed load transport rate in sand-bed channels (Baranya et al., 2023). Another commonly referenced model is the Einstein-Brown (Einstein, 1950; Brown, 1950) formulation, which has undergone modifications in several studies to account for the effects of vegetation on sediment transport processes (Armanini et al., 2005; Yang and Nepf, 2018). van Rijn (1984a) derived a formulation that expresses the bed load transport rate per unit width $q_s$ for particle size in the range $0.2 \div 2$ mm that reads:

$$\frac{q_s}{[(s-1)g]^{0.5} D_{50}^{1.5}} = 0.053 \frac{T^{2.1}}{D_*^{0.3}} \tag{2.1}$$

where $s = \rho_s/\rho$ the specific density, with $\rho$ the water density, $\rho_s$ the sediment density, $D_{50}$ is the particle size and $D^*$ is the particle parameter and $T$ is the transport parameter:

$$D^* = D_{50} \left[ \frac{(s-1)g}{\nu^2} \right]^{1/3}, \qquad T = \frac{[(u'_*)^2 - (u'_{*,cr})^2]}{(u'_{*,cr})^2} \tag{2.2}$$

with $\nu$ the kinematic viscosity ($\mu/\rho$), with $u$ = mean flow velocity, $u'_{*,cr}$ = critical bed-shear velocity according to Cao et al. (2006). $u'_*$ is the bed-shear velocity related to grains, that is the effective shear that drives bed load transport. The bed shear stress can be divided into two components: i) shear stress due to grain roughness or skin friction, $\tau'_b$, and

ii) form-related bed shear stress or form drag, $\tau_b''$ (van Rijn, 1984a; Yen, 2002). When bedforms are present, $\tau_b''$ is associated with the pressure drag caused by the bedform geometry (Einstein and Barbarossa, 1952; van Rijn, 1984b).

The equation proposed by Brown (1950) is a simplified version of the probabilistic formulation published in Einstein (1950), and it is cited herein as Einstein-Brown. This equation incorporates the assumption that the probability of a sediment particle being eroded is closely connected to the likelihood of the particle experiencing a lift force. The equation reads:

$$q_s* = \begin{cases} 2.15e^{-0.391/\tau_*}, & \text{if } \tau_* < 0.18. \\ 40\tau_*^3, & \text{if } 0.18 < \tau_* < 0.52. \end{cases} \tag{2.3}$$

where $q_s*$ and $k_t*$ are the dimensionless transport rate and turbulent kinetic energy, respectively:

$$q_s* = \frac{q_s}{\rho_s \omega_0 D_{50}}, \quad \tau_* = \frac{\tau}{(\rho_s - \rho) g D_{50})} \tag{2.4}$$

where $q_s$ is the sediment transport per unit width and $\omega_0$ particle fall velocity.

Dunes, which have been found the most common feature in alluvial channels, influence the entire flow field and represent a main source of hydraulic roughness (Naqshband, 2014; Branß and Aberle, 2022). In presence of bedforms, sediment transport rate is typically quantified using the migration rate and bedforms height (Simons et al., 1965; van Rijn, 1984b; Leary and Buscombe, 2020). This approach assumes that migration serves as the predominant mechanism driving dune sediment transport and that migration rates exhibit a positive correlation with the transport stage (Lin and Venditti, 2013; Yalin and Karahan, 1979). To maintain a constant sediment transport rate, it follows that the migration rate of an individual dune would exhibit an inverse relationship with its height, resulting in a decline in migration rate as dune height escalates (Coleman and Melville, 1994; Lin and Venditti, 2013).

Several studies suggest the possibility to relate turbulence characteristics and sediment transport rate. McLean et al. (1994) investigated turbulence characteristics over a two-dimensional dune and emphasized

the nonlinearity of bed load transport, which is strongly influenced by temporal velocity statistics. Nelson et al. (1995) explored the relationship between turbulent bursting events and sediment particle movement during bed load transport, highlighting the energetic role of flow separation zones in dune development. McLean et al. (1999) measured turbulent characteristics over a fixed two-dimensional dune, further emphasizing the influence of temporal velocity fluctuations on bed load transport in the near-bed flow zone. However, currently, there is a lack of a valid turbulence-based model for accurately predicting sediment transport in the presence of a sand bed with bedforms.

The presence of riparian vegetation plays a crucial role in shaping sediment dynamics within rivers, affecting erosion, resuspension, and deposition processes and subsequently impacting the morphological evolution of river systems (Gurnell, 2014). Vegetation increases the overall flow resistance, leading to reduced bed shear stress and increased sediment deposition, thereby affecting the capacity for bed load transport (Le Bouteiller and Venditti, 2015; Nepf, 2012). Thus, vegetation drag enhances the potential for sediment trapping and resuspension, with denser vegetation enhancing these processes (Wu and He, 2009; Tinoco and Coco, 2016). Notably, the bed resistance in channels with riparian vegetation can be significantly lower compared to non-vegetated channels with the same discharge (Duan and Al-Asadi, 2022).

Existing models based on bed shear stress have been found to be inaccurate in the presence of obstacles such as vegetation and bedforms (Yager and Schmeeckle, 2013; Vargas-Luna et al., 2015). In vegetated settings, equations developed for bare bed conditions are commonly employed by introducing additional parameters without modifying the bed load transport formula. Bonilla-Porras et al. (2021) presented a modified bed load transport equation that extends Einstein-Brown model by adding parameters that explicitly include the effect of vegetation, whether emergent or submerged. Similarly, Armanini and Cavedon (2019) modified the Einstein-Brown formula aiming to extend its applicability to both bare bed conditions and the presence of emergent vegetation. This was achieved by redefining the dimensionless flow intensity parameter $\Psi = (g\rho_s/\rho D_{50})/(u_*)^2$ and sediment transport rate $\Phi = q_s/(D_{50}\sqrt{g\rho_s/\rho D_{50}}$ (Einstein, 1950) and

extending them to incorporate the effect of vegetation.

Recent studies have highlighted the influence of vegetation-generated turbulence on sediment transport. Vegetation has been found to increase turbulence intensities, potentially leading to a greater transport rate (Nepf, 1999; Nelson et al., 1995). It has been observed that vegetation-generated turbulence plays a crucial role in the resuspension of sediment (Yang and Nepf, 2018; Tinoco and Coco, 2016), highlighting the need to incorporate this phenomenon in sediment transport models. These findings challenge the conventional bed-shear-stress-based models, which do not account for the turbulence generated by vegetation.

Yang and Nepf (2018) developed a novel model to predict bed-load transport based on near-bed turbulent kinetic energy. The authors modified the bed-shear-stress-based Einstein-Brown equations to incorporate turbulence-based formulations. In the absence of vegetation, sediment transport in bare beds is primarily driven by the turbulence-induced lift force, which exhibits a proportional relationship with the bed shear stress (Einstein, 1950; Yang and Nepf, 2018). However, the authors emphasized that turbulence-induced lift force and bed shear stress are not linearly correlated in the presence of vegetation. The development of this model was based on experimental activities conducted in the presence of rigid cylinders and ripples, limiting its applicability to scenarios involving larger bedforms or vegetation with more complex morphology, such as leafy flexible plants. By addressing these limitations, it is possible to enhance the understanding of sediment transport dynamics in natural environments and improve the accuracy of predictive models for managing vegetated river systems.

Recent field work by Afzalimehr et al. (2019) has highlighted the impact of vegetated bedforms within a river reach, demonstrating that the presence of vegetation enhances turbulence anisotropy. Some studies have also pointed out that aquatic vegetation might suppress bedforms in rivers (Nepf, 2012), reducing their role in migrating bedforms for sediment transport (Yang and Nepf, 2019). Furthermore, Le Bouteiller and Venditti (2014) investigated the response of sediment transport and morphodynamics to flexible submerged blade-shaped vegetation, showing that plants reduce the sediment transport capacity. This reduction leads to the ad-

justment of the bed by increasing its slope to facilitate sediment passage through the plant patch.

Despite these advancements, there is still a significant lack of knowledge regarding the morphodynamic response of sand beds in the presence of vegetation, particularly natural-like vegetation. Specifically, there is insufficient understanding of how vegetation density and morphology can influence bedform characteristics and migration rates (Yang and Nepf, 2019). Furthermore, the lack of a valid model to predict sediment transport in the presence of leafy flexible vegetation, including turbulence-based models, highlights the need for further research and development in this field. It is crucial to enhance the understanding of the complex interactions between vegetation, hydrodynamics, and morphodynamics, in order to develop more accurate models and efficient management strategies for vegetated river systems. By incorporating the intricate interactions among flow, vegetation, and sediment, the prediction of sediment transport can be improved, leading to a better understanding of the morphological changes that occur in river systems (Box et al., 2021).

## 2.4 Predicting Flow Resistance in Presence of Vegetated Bedforms

Flow resistance in a vegetated channel is composed of two main components: boundary resistance and vegetation resistance. Boundary resistance encompasses sidewall resistance, grain roughness, and bedform resistance on a mobile bed surface. Grain resistance refers to the friction resulting from the roughness of the bed surface, which is influenced by the size of the bed sediment. On the other hand, bedform resistance is the drag force arising from flow separation at the lee side of bedforms, and it is influenced by the height of the bedforms (Engelund, 1966; Yalin, 1964). The drag exerted by the vegetation elements is a critical factor in accurately determining the flow resistance in vegetated areas (Aberle et al., 2011). In traditional approaches, the presence of vegetation is typically addressed by assigning a higher value to Manning coefficient of the channel bed (Arcement and Schneider, 1989; Chow, 1959). This approach is appropriate for 1D analysis and not for detailed investigation of the ef-

fects of vegetation on flow resistance (Schoneboom et al., 2010). For rigid cylinders, the drag force can be estimated following the classical definition of drag force $F_D$ (Chow, 1959). Thus, in the case of an array of rigid cylinders, the drag force ($F_D$) and flow velocity ($U$) exhibit a quadratic relationship, expressed as $F_D = 0.5\rho A_f C_D U^2$, assuming a constant water depth and drag coefficient ($C_D$) within the vegetation canopy. Here, $A_f$ represents the frontal projected area, which is used to quantify the vegetation density (Västilä and Järvelä, 2014). For an array of rigid cylinders, the bulk drag is also affected by the spacing and the pattern of the elements (Tanino and Nepf, 2008a; Schoneboom et al., 2011). The rigid cylinder model is commonly employed to represent the resistance exerted by a woody trunk. However, this simplification becomes inadequate in the presence of leafy flexible plants.

Several alternative approaches have been developed to account for different vegetation structure and flexibility in predicting flow resistance (Västilä and Järvelä, 2018; Järvelä, 2004). The flexibility of both leafy and leafless riparian vegetation introduces modifications to the relationship between $F_D$ and flow velocity $U$. In this case, the frontal projected area ($A_f$) decreases as the flow velocity increases due to the leaves adopting a more streamlined configuration with the main flow direction. Consequently, there is a reduction in the drag force, and the relationship between $F_D$ and $U$ becomes closer to linear rather than quadratic (Järvelä, 2004; Schoneboom et al., 2011). To capture this non-quadratic relationship, it is common to utilize the reconfiguration parameter or Vogel coefficient ($\chi$), which modifies the relationship to $F_D \propto U^{(2+\chi)}$. The value of $\chi$ typically ranges between -0.2 and -1.2 (Jalonen et al., 2014; Västilä and Järvelä, 2014). Järvelä (2004) suggested to estimate the density of the leafy vegetation using the leaf area index (LAI). Moreover, Jalonen et al. (2013) found that the density, the spatial variability and the ratio of foliage area over stem area have a significant impact on drag force.

The linear superposition is commonly employed to combine the resistance from different factors in flow resistance studies (Schoneboom et al., 2010; Aberle and Järvelä, 2013; Le Bouteiller and Venditti, 2015). This approach, initially introduced by Meyer-Peter and Müller (1948) and Einstein and Banks (1950) for bed roughness, is based on the assumption that,

using the momentum concept, the bed shear can be separated linearly into a reference plane-bed shear and an additional bed shear. However, the linear superposition approach should be applied with caution when dealing with multiple resistance factors. In this case, each factor is typically determined independently, without considering the influence of other factors, even though the relationship among them may be nonlinear. As a result, employing a linear combination using these individually calculated factors often results in an overestimation of the combined resistance factor (Yen, 2002).

Moreover, over the past years, conflicting results have been reported in the scientific literature regarding the effect of bed-load movement on flow resistance. Song et al. (1998) found that the observed friction values in the mobile bed experiments are higher than those predicted by the law of the wall. The presence of sediment transport was found to increase flow resistance due to particle-bed and particle-particle collisions, as well as the horizontal acceleration of particles (Rebai et al., 2022; Gao and Abrahams, 2004; Recking et al., 2008).

In the context of utilizing a bed-shear-stress model for sediment transport prediction, it is important to eliminate the influence of form drag, as it does not play a role in bed load transport. This exclusion can be accomplished by solely considering the grain-shear stress (van Rijn, 1984a). In scenarios where numerous sources of flow resistance coexist, it is a customary practice to employ the linear superposition principle as a means to derive the grain-shear stress (Le Bouteiller and Venditti, 2015).

However, our current understanding of flow resistance composition in the presence of multiple sources of roughness remains limited. There exists a significant knowledge gap concerning the interactions and contributions of various resistance factors to the overall flow resistance, in such complex scenarios. Further research is necessary to thoroughly investigate and characterize the intricate composition of flow resistance when multiple sources of resistance are present, both in fixed and mobile bed conditions.

## 2.5 Specific Objectives

The main motivation of this work was to investigate the intrinsic process between flow, vegetation and morphodynamics particularly in scenarios where vegetation and large-scale bedforms, such as dunes, could coexist. Predicting turbulence characteristics, sediment transport, and morphodynamics evolution in these scenarios can be highly complex due to the combined effects of the involved factors. The presence of vegetation has a significant impact on the flow field, which, in turn, influences the characteristics of the bedforms and contributes to an increase in flow resistance.

The primary objective of this thesis is to provide insights into the interactions among the flow field, morphodynamics, and leafy flexible vegetation. Based on the aforementioned gaps in knowledge, the objective of this research is to bridge these lacks of understanding by specifically addressing the following questions:

1. How does leafy flexible vegetation impact dune characteristics and subsequently sediment transport processes? (Chapter 3)

2. What is the combined influence of leafy flexible vegetation and dune on the flow field? What are the differences in the flow field when considering mobile or fixed bed conditions? (Chapter 4)

3. What is the composition of flow resistance in the presence of vegetation and dune? Is the linear superposition principle still valid? (Chapter 5)

## 2.6 Structure of the Thesis

After reviewing the existing literature and identifying the existing knowledge gaps regarding the interaction between natural-like vegetation and morphodynamics, different experimental activities were defined and conducted (Figure 2.6).

Experimental activities were performed in mobile bed conditions and in the presence of leafy flexible vegetation with the aim to investigate the

effects of varying plant leaf mass on morphodynamics and dune characteristics (Chapter 3). Complementary experimental activities were conducted using fixed bed conditions. The physical model utilized in these experiments was designed to replicate the final morphology observed in the mobile bed conditions. This was achieved by 3D-printing a digital model obtained through the Structure-from-Motion technique. By conducting a valuable comparison with previous results, this study offers novel insights into the consequences that arise from considering fixed bed conditions rather than mobile bed conditions (Chapter 4) . Additional activities were dedicated to directly measure the hydraulic forces exerted from both vegetation and dune aiming to deepen the understanding of how flow resistance is distributed and partitioned among different sources (Chapter 5).

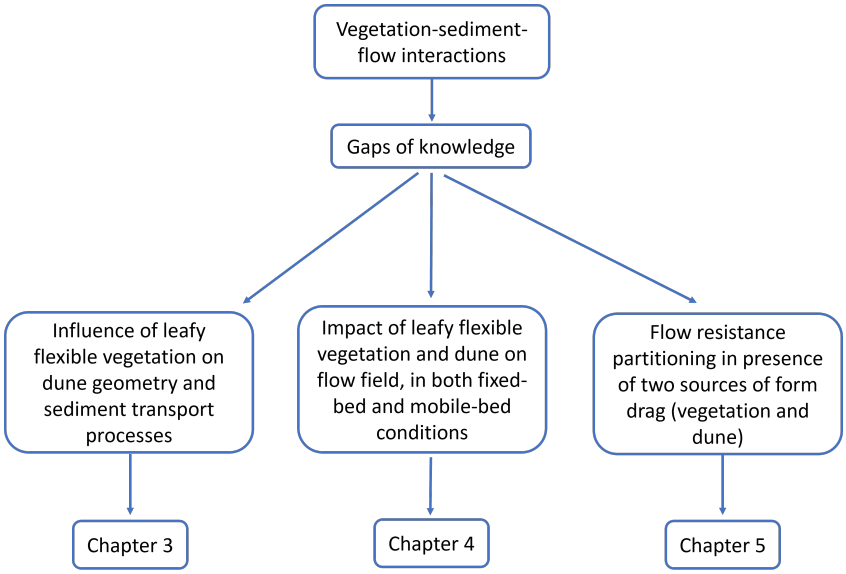


Figure 2.6: Thesis organization. Each research question is addressed in separate chapters.

# Chapter 3

# The Effects of Vegetation on River Dunes

## 3.1 Introduction

Recently, river restoration strategies have increasingly focused on rehabilitation, using vegetation to reduce erosion, increase bank stability, and enhance habitat quality (Yager and Schmeeckle, 2013). Unlike traditional approaches that involved vegetation removal, it is now recognized that such practices are counterproductive for successful river restoration in ecological terms (Schoneboom et al., 2008; Palmer et al., 2005). However, the understanding of the complex physical processes governing fluvial environments remains incomplete (Wang et al., 2023). Huai et al. (2021) reviewed recent progress in understanding the role of vegetation in flow dynamics and sediment movement and pointed out that the majority of studies on the interaction between vegetation and flow considered only flat bed conditions. Since bedforms or ripples were only taken into account in very few works (Yang and Nepf, 2019; Le Bouteiller and Venditti, 2015), the authors emphasized the urgent need to consider both the role of vegetation and bed topography on flow dynamics to increase the reliability and efficiency of river restoration projects. In other words, the design of restoration projects should be based on trustworthy tools to predict the morphodynamic evolution of the river system in order to prevent ineffec-

tiveness or failure of the restoration measures (D'Ippolito et al., 2023).

Conducting detailed analyses and controlled laboratory experiments is essential to acquire comprehensive knowledge about the physical processes involved in the interactions between vegetation, sediment processes, and flow dynamics. This knowledge serves as a crucial foundation for developing models that accurately represent and predict real-world phenomena, enabling their practical application in field environments. However, current approaches for estimating sediment transport in vegetated channels often rely on simplified methods, and the availability of models incorporating vegetation is limited. Many existing models were developed or adapted for specific conditions, limiting their applicability to a wider range of scenarios. Realistic representation of vegetation is crucial, as natural riparian vegetation in alluvial floodplains consists of diverse combinations of woody plants, flexible leafy shrubs, and grasses that cannot be accurately represented by rigid cylinder simplification (Box et al., 2021; Järvelä, 2004; Aberle and Järvelä, 2013).

Experimental studies of Chen et al. (2012) investigated the effects of submerged bundled plastic fibers on flow characteristics and the formation of scour holes. The authors observed that vegetation density had a direct impact on various aspects, such as scour depth, dune height, length of the scour hole, horizontal distance of the maximal scour depth, and horizontal distance of the dune crest. Specifically, a decrease in vegetation density resulted in an increase in these parameters.

Similarly, Follett and Nepf (2012) conducted a laboratory study to examine sediment patterns around a patch of reedy emergent vegetation in a sand bed. Their findings supported the notion that dense patches of vegetation caused significant flow diversion, leading to increased downstream sediment transport before deposition along the centerline of the vegetation patch.

The studies conducted by Tang et al. (2013) and Yang et al. (2016) focused on the effects of emergent rigid vegetation in open channels. Both studies reported that the presence of vegetation reduced the incipient motion of sediment compared to channels without vegetation, highlighting the influence of vegetation on sediment dynamics.

Furthermore, Yager and Schmeeckle (2013) conducted experiments in-

volving rigid cylinders and mobile sand. Their findings indicated that the presence of vegetation influenced the formation of non-migrating bedforms, which scaled with the distance between vegetation patches. Moreover, conventional models that rely on bed shear stress to predict sediment transport rates have been found to be inaccurate in the presence of vegetation and depositional bedforms (Yager and Schmeeckle, 2013). Nevertheless, a significant knowledge gap remains regarding the morphodynamic response of sand beds to vegetation, especially when dealing with natural leafy vegetation.

In a bare dunes bed, the geometry and migration rate of bedforms are often correlated to sediment transport rate (Simons et al., 1965). However, this correlation does not hold true in the presence of vegetation. Field and experimental studies have observed that vegetation can decrease the migration rate or even suppress bedforms (Przyborowski et al., 2018; Nepf, 2012; Yang and Nepf, 2019). Hence, understanding how vegetation influences the geometry and migration rate of bedforms is crucial for accurately estimating sediment transport in vegetated channels (Yang and Nepf, 2019).

In this chapter, the results of experiments conducted under mobile bed conditions, which led to the formation of dunes, are presented. For these experiments, leafy flexible artificial vegetation with removable branches was used, maintaining just-submerged conditions. The primary objective of this analysis was to examine the effects of leafy flexible vegetation on sediment transport rate and bedform characteristics, with a specific focus on their geometry and celerity. The applicability and validity of various existing models and methods for predicting sediment transport and bedform characteristics were assessed. By comparing the outcomes of these approaches with empirical data obtained from the experimental activities, the inherent limitations in these methodologies were identified, providing valuable insights into the influence of vegetation on sediment dynamics.

## 3.2 Material and Methods

### 3.2.1 Experimental Setup

Experiments were performed in a tiltable sediment recirculating flume located in the hydraulic laboratory of the Leichtweiß-Institut für Wasserbau at the Technische Universität Braunschweig. The flume had dimensions of 2 m width, 0.8 m height, and 30 m length. However, the flume width was reduced to $W = 0.6\ m$ in order to replicate the conditions of previous fixed-bed experiments conducted using the same artificial plants (described below) (Jalonen et al., 2013; Schoneboom and Aberle, 2009; Schoneboom, 2011). A PVC plate was securely attached to the flume bottom and featured pre-located holes through which the plants were affixed using 15 cm-long rigid carbon extensions. Figure 3.1 shows a portion of the extension, labeled with a red rectangle. To prevent potential scouring from reaching the bottom of the PVC plate during the experimental runs, a layer of mobile bed sand with a thickness of 15 cm was meticulously arranged on top of the PVC plate. The sand had a characteristic diameter of $D_{50} = 0.84$ mm, and geometric standard deviation, $\sigma_g = (D_{84}/D_{16})^{0.5} = 1.32$. During the experiments, the sand was collected in a sediment trap at the downstream end of the flume, recirculated, and fed back as water-sediment mixture at the inlet section of the flume (Figure 3.2).

The origin of the coordinates system is located at the inlet section, at the hydraulic left-handed side of the flume, on the bottom of the flume (Figure 3.3). Flow straightening tubes were placed at the inlet section of the channel to reduce turbulence in the incoming flow discharge. Additional rows of rigid cylinders were installed after the tubes to accelerate the development of the flow (Figure 3.3).

A total of 297 artificial flexible vegetation elements of 23 cm height were employed for the experiments. The artificial plants used in this work are commercially available elements whose hydrodynamic characteristics were known from previous studies (Schoneboom and Aberle, 2009; Aberle et al., 2011). The plants consisted of a 3 mm thick coated wire stem with a bending stiffness of $K = 6965 N/mm^2$, four removable branches, and a blossom. Each branch featured three leaves made of highly flexible

dyed textile, for which the individual single-side leaf area was determined through image analysis in Schoneboom and Aberle (2009).

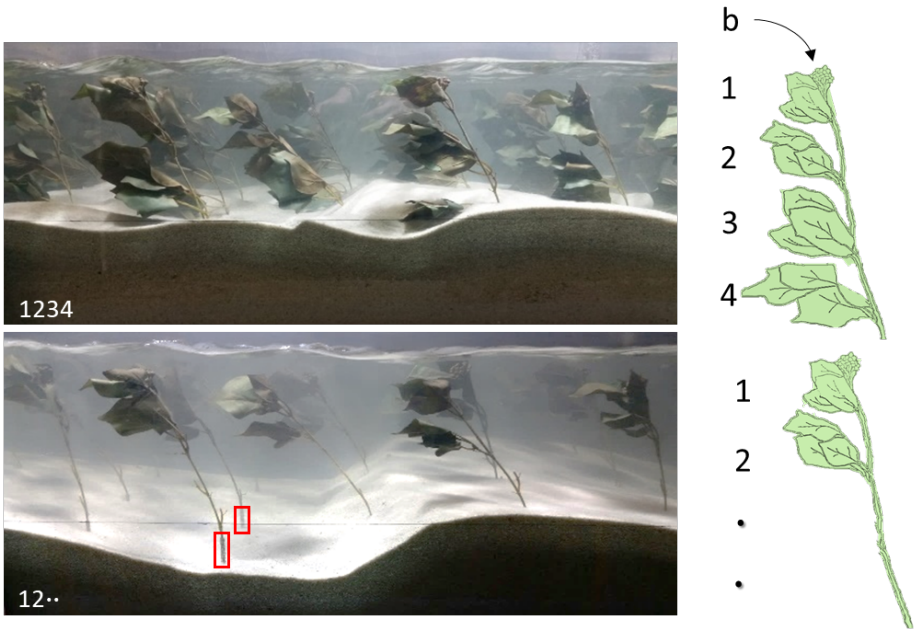


Figure 3.1: Side view photos of two different plant stages: fully foliated setup (1234) on the top, mid leafed setup (12••) on the bottom. Red rectangles highlight the rigid extensions used to secure the plants at the bottom of the flume.

For the experiments, seven different foliage configurations were considered and obtained by removing one or more branches from the plants. Therefore, each setup had a different one-sided leaf area $A_L$ (Table 3.1) and consequently a different Leaf Area Index ($LAI$), that is defined as:

$$LAI = \frac{A_L}{A_b} \tag{3.1}$$

where $A_b$ is the ground area. In Table 3.1, $A_{tot}$ represents the total one-sided area, which was obtained by summing the one-sided area $A_L$ and the stem area $A_s$. The stem area includes the frontal area of the stem and the frontal area of the blossom (if present). The solid volume fraction $\phi$ was calculated as the ratio of the vegetation volume $V_p$ to the water

volume $V$ (Lei and Nepf, 2021; Zinke, 2012). The vegetation volume ($V_p$) was determined using the Archimedes principle (Xu and Nepf, 2020). The resulting $\phi$ values were validated with the data reported in Jalonen et al. (2013).

Table 3.1: Plants foliage configuration and specific parameters. $A_L$ is the one-sided leaf area, $A_s$ is the sum of the stem frontal area and blossom frontal area, $A_{tot} = A_L + A_s$. $V_p$ is the vegetation volume. $\phi$ is the solid volume fraction.

| Setup | $A_L$ ($cm^2$) | $A_s$ ($cm^2$) | $A_{tot}$ ($cm^2$) | $A_L/A_s$ (-) | LAI (-) | $\phi$ (%) | $\langle a \rangle_z$ ($m^{-1}$) | $V_p \pm S.E.$ ($cm^3$) |
|---|---|---|---|---|---|---|---|---|
| 1234 | 373.6 | 20 | 393.7 | 18.6 | 0.93 | 0.15 | 0.93 | 13.47 ± 0.15 |
| 123• | 237.8 | 20 | 257.9 | 11.8 | 0.59 | 0.11 | 0.86 | 8.91 ± 0.26 |
| 12•4 | 264.3 | 20 | 284.4 | 13.2 | 0.66 | 0.10 | 0.73 | 9.65 ± 0.09 |
| 12•• | 128.5 | 20 | 148.6 | 6.4 | 0.32 | 0.08 | 0.55 | 6.63 ± 0.15 |
| 1••• | 66.0 | 20 | 86.1 | 3.3 | 0.17 | 0.06 | 0.34 | 5.57 ± 0.09 |
| b•••• | - | 20 | 20 | - | - | 0.04 | 0.16 | 4.03 ± 0.04 |
| •••• | - | 10 | 10 | - | - | 0.02 | 0.08 | 1.60 ± 0.09 |

The setup name provides information about the foliage configuration of the plants. Numbers 1 to 4 indicate the level of attached branches, with 1 representing the top-most level and 4 the bottom-most. The letter "b" denotes the blossom located at the apex of the plant, while "•" identifies the removed branch (Figure 3.1). The blossom was present in all plant setups, except for the •••• configuration. Additionally, a reference experiment, named "bare bed," was conducted without any vegetation.

The plants were arranged in a staggered pattern, starting at a distance of 4.2 meters from the flume inlet. This pattern extended over a flume section of 20 meters, with a spacing of 20 cm in both directions between the plants (Figure 3.2). The plant density $m$ was maintained uniformly across the entire flume, with a value of $m = 25\text{plants}/m^2$. The same pattern and density were used in previous experiments conducted with the same plants (Jalonen et al., 2013; Aberle et al., 2011).

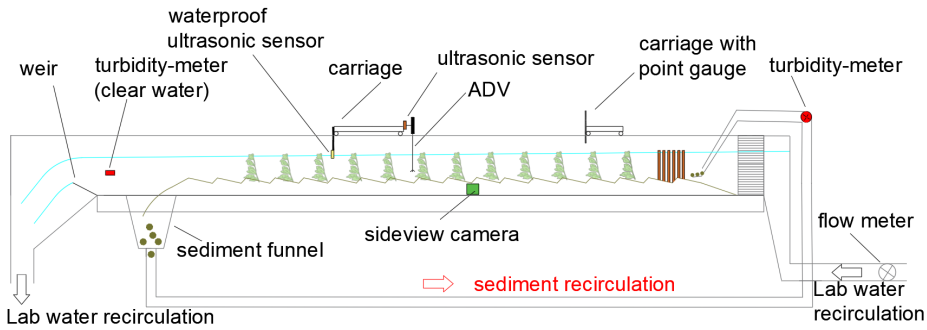


Figure 3.2: Schematic side view of the flume. Flow direction right to left. The figure is not to scale.

### 3.2.2 Measurement Instruments

During the experimental runs, the sediment transport rates were measured by means of two turbidity-meter sensors (Fischer & Porter magnetic flow meters, accuracy ± 0.5 %), one at the flume outlet after the sediment drain and one in the return pipe of the sediment recirculating system (Figure 3.2). A calibration formula was employed to establish a relationship between the voltage difference ($\Delta$) observed in the signals of the two turbidity meters and the corresponding sediment transport rate $Q_s$ (described in Section 3.2.3). The water discharge $Q$ was continuously measured during the experimental runs with a Krohne magnetic flow meter (accuracy ± 0.3%). The water surface was scanned using mic +130/IU/TC ultrasonic sensor with a resolution of 1 mm (accuracy ± 0.57 mm). The sensor was mounted on an automated carriage system and scans were conducted along the middle line of the channel.

The bottom topography was scanned with a submerged Sonometer05 ultrasonic sensor with a resolution of 1 mm (accuracy of up to 1%). The measurements were performed in clear water conditions achieved by increasing the weir height at the end of the flume to suppress sediment transport. To minimize interference with the ongoing experiment, the bed profiles were scanned only at the end of each experimental day, which lasted approximately 8 hours. The bed profiles were scanned along three longitudinal lines: y=15 cm, y=30 cm (middle line), and y=45 cm (where

y=0 corresponds to the hydraulic left-handed side of the flume). The effective measurement section, highlighted as a pink rectangle in Figure 3.3, spanned 15.3 m, located between x=7.5 m and x=22.8 m (where x=0 is situated at the inlet section of the flume). These measurements were used to evaluate the average bed slope and water surface slope.

Moreover, the scanned bed profiles were used to estimate the bedforms characteristics. In this case, only the scan measurements between $x = 12$m and $x = 21$m were taken into account, excluding the channel sections influenced by the inlet and outlet conditions. This selection resulted in a total of 9000 samples for each bed elevation profile. Moreover, a side view camera was employed to record the lateral evolution of the bed elevation during each experimental run (Figure 3.1). This served for a further analysis of the bedforms characteristics, particularly their celerity (Section 3.3.3). All the side-view videos recorded during the experiments are available at the provided repository by Artini (2023), offering insights into the experiments dynamics. At the end of each experiment, the flume was carefully emptied, and photographs of the bed topography were taken. These images were then utilized to reconstruct a digital elevation model (DEM) using the Structure-from-Motion technique (Morgan et al., 2017). Further detailed information is reported in Section 4.4.

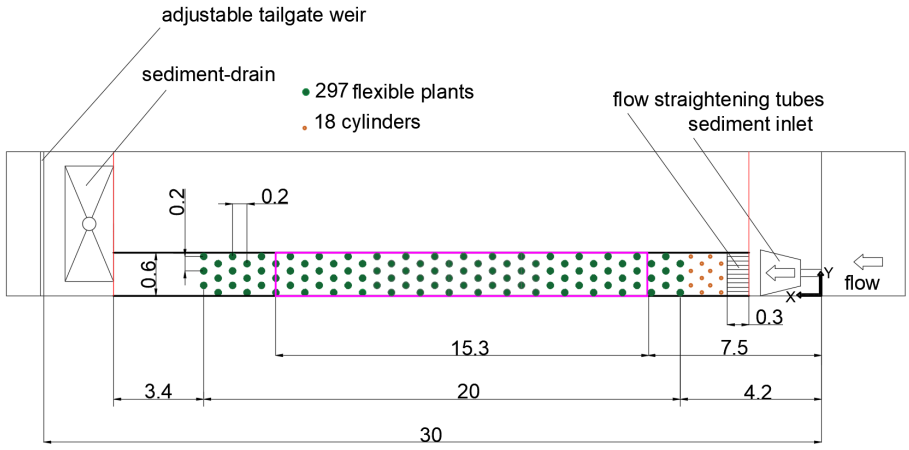


Figure 3.3: Schematic plan view of the flume. Flow direction right to left. The figure is not to scale.

### 3.2.3 Calibration of the Sediment Recirculating System

The calibration of the sediment recirculating system consists of two main phases. The first phase determined the quantity of sand introduced into the system, which is needed for the second phase aimed to determine the bed load transport rate using the two turbidity meters. The first phase involves investigating the correlation between the bed-load transport rate exiting a sand-filled tank and various outlet diameters. The tank was positioned above the system inlet and eight distinct outlet diameters were selected (as detailed in Table 3.2). The dry sand discharged from the tank over a one-minute period is carefully collected and weighed. The second phase aimed to determine the bed load transport rate using the two turbidity meters. The sediment recirculating system was fed with sand exiting from the tank at a known rate, and the outputs of the turbidity meters were recorded simultaneously. To precisely control the sand input into the system, an obstacle board was fixed at the sediment recirculating system inlet to prevent any undesired sediment from entering. The mean of the measurements from the two turbidity sensors was then evaluated, considering only the stable data range and disregarding voltage signal fluctuations that stabilize over time. The difference in voltage $\Delta_V$ between the data from the two turbidity meters is assessed using the following equation:

$$\Delta_V = T_s - (T_B + offset) \tag{3.2}$$

Where $T_s$ refers to the measurements taken by the turbidity meter placed at the outlet of the sediment recirculating system, $T_B$ refers to a "background" value measured by the turbidity meter placed after the sediment drain, resulting in a reference for clear water state, and the $offset$ is a reference value for a state in the absence of sediment transport, which is estimated as:

$$offset = T_s - T_B \tag{3.3}$$

This value was assessed daily at the start of each experimental day, before any sediment transport measurements were taken

The difference in volts expressed as Equation 3.2 was correlated with the known amount of sand introduced into the sediment recirculating system, i.e., the sediment transport rate. Through curve fitting of the data

Table 3.2: First phase of the calibration

| Diameter (mm) | Time (s) | Sand (g) | Mean Sand (g) | Qs (g/s) | st.dev. Qs |
|---|---|---|---|---|---|
| 6 | 60 | 318 | | | |
| 6 | 60 | 317 | 316 | 5.27 | 0.68% |
| 6 | 60 | 313 | | | |
| 7 | 60 | 482 | | | |
| 7 | 60 | 480 | 476 | 7.93 | 0.91% |
| 7 | 60 | 472 | | | |
| 8 | 60 | 725 | | | |
| 8 | 60 | 729 | 725 | 12.09 | 0.34% |
| 8 | 60 | 723 | | | |
| 9 | 60 | 1004 | | | |
| 9 | 60 | 996 | 998 | 16.63 | 0.47% |
| 9 | 60 | 993 | | | |
| 10 | 60 | 1242 | | | |
| 10 | 60 | 1236 | 1 247 | 20.79 | 0.97% |
| 10 | 60 | 1264 | | | |
| 11 | 60 | 1790 | | | |
| 11 | 60 | 1801 | 1 804 | 30.07 | 0.74% |
| 11 | 60 | 1822 | | | |
| 13 | 60 | 2826 | | | |
| 13 | 60 | 2869 | 2 866 | 47.77 | 1.11% |
| 13 | 60 | 2904 | | | |
| 15 | 60 | 4141 | | | |
| 15 | 60 | 4198 | 4 196 | 69.93 | 1.04% |
| 15 | 60 | 4248 | | | |

obtained from the process, the calibration equation was derived to convert $\Delta_V$ into measurements of $Q_s$, as reported in Table 3.3 and Figure 3.4:

$$Q_s = 46.11{\Delta_V}^2 - 72.49\Delta_V \tag{3.4}$$

The average percentage error between the known and estimated sediment transport rates $Q_s$ is 3% ( Table 3.3). The "$EstimatedQ_s$" values were obtained through the Equation 3.4.

Table 3.3: Second phase of the calibration. The offset measured for the calibration process was equal to -0.054.

| Known $Q_s$ (g/s) | $T_B$ | $T_s$ | $\Delta_V$ (Volts) | Estimated $Q_s$ (g/s) | Percentage error (%) |
|---|---|---|---|---|---|
| 0 | -1.084 | -1.137 | 0 | 0 | |
| 5.27 | -1.090 | -1.194 | -0.051 | 3.848 | 27 |
| 7.93 | -1.098 | -1.249 | -0.098 | 7.560 | 5 |
| 12.09 | -1.105 | -1.307 | -0.150 | 11.870 | 2 |
| 16.63 | -1.115 | -1.386 | -0.218 | 17.980 | -8 |
| 20.79 | -1.129 | -1.440 | -0.259 | 21.840 | -5 |
| 30.07 | -1.139 | -1.515 | -0.323 | 28.246 | 6 |
| 47.77 | -1.150 | -1.707 | -0.504 | 48.285 | -1 |
| 69.93 | -1.156 | -1.882 | -0.674 | 69.792 | 0 |

### 3.2.4 Methods for Data Analysis

The bed and water surface scans were subjected to post-processing, including de-spiking and gap-filling tools, in Matlab environment (R2019b). These post-processed scans were then utilized to estimate the bed and energy slopes (Figure 3.5). The mean bed level is determined by identifying the z-coordinate of a line where the areas above and below the bed profile intersecting that line are equal in magnitude. The water depth $H$ is estimated as the average difference between the water surface elevation and the bed level (Figure 3.5).

The depth-average frontal area of a canopy is defined as $\langle a \rangle_z = mA_f/h_p$, where $A_f$ is the streamlined frontal area of a plant and $h_p$ is the deflected height. In the present case, the $A_f$ occurred during the experiments was estimated indirectly by referencing the corresponding channel-averaged velocity $U = Q/(WH)$ to the $A_f$ values obtained from Jalonen et al. (2013) experiments for different foliage setups (Figure 6 in Jalonen et al. (2013)). In the case of the •••• setup, the streamlined frontal area $A_f$ is determined by the product of the plant deflected height $h_p = 0.18m$ and the stem diameter $d = 3mm$. For the b•••• setup, $A_f$ was determined using an image analysis procedure described in Xu and Nepf (2020) (Figure 3.6). For this analysis, two plants were selected and photographed against a white background from five different angles. The original plant images were transformed into black and white images, and the number of black pixels was counted at each vertical coordinate. By using a reference

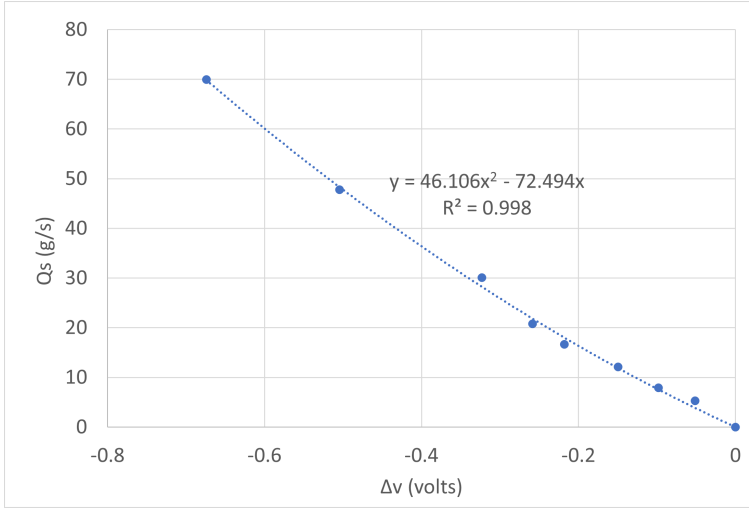


Figure 3.4: Calibration formula for the sediment recirculating system.

scale, the pixel count was converted into length obtaining the frontal area distribution $A(z)$. The cumulative frontal area $A_f$ for a single plant was calculated by integrating $A(z)$ over the plant height $h_p$.

The equivalent diameter, defined as the diameter of a cylinder that has the same frontal area as the leafy plants, can be calculated as $d_e = A_f/h_p$ (Xu and Nepf, 2020; Järvelä, 2004). In just submerged condition, where the water depth $H$ is approximately equal to $h_p$, the depth-averaged frontal area can be expressed as $\langle a \rangle_z = md_e$.

The measured sediment transport rates were compared to predicted values using three classical sediment transport models based on bed shear stress. The models considered in this analysis are the bed load transport equation by van Rijn (1984a), the equation proposed by Einstein (1950) and Brown (1950), and the equation by Wong and Parker (2006) that corrects the Meyer-Peter and Müller (1948) formula. The formula is based on the excess of dimensionless bed shear stress over a critical value. The considered amended expression is the Equation 22 in Wong and Parker (2006). In applying the aforementioned formulations, only parameters related to grain stress were considered to estimate the bed shear stress, as sediment transport is primarily influenced by skin friction (van Rijn,

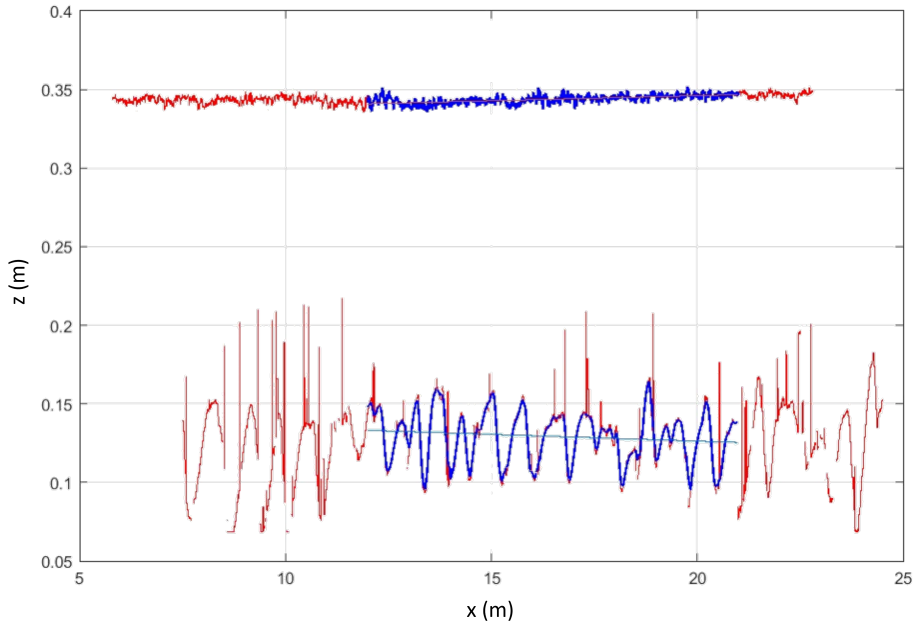


Figure 3.5: Bed and water surface profiles scanned during the 12•4 run, specifically on day 4, at y=30 cm. The raw signal undergoes de-spiking and smoothing to remove plant interference, and any missing values are interpolated using a moving mean method.

1984a). Specifically, the grain-related friction velocity $u'_*$ was estimated using the formula proposed by Engelund (1966), which has been recognized as effective in the presence of dunes (Van der Mark, 2009) (further details in Chapter 5).

The estimation of bedform wavelengths was conducted using the zero-crossing technique proposed by Van der Mark and Blom (2007). This method involves removing the average bed slope from the bed elevation profiles and considering only bedforms that crossed the mean bed level. The wavelength of each bedform, denoted as $\lambda_{crest}$, was determined as the distance between consecutive crests, following the recommendation by Van der Mark and Blom (2007). All observed bedforms were classified as dunes, as their average wavelength exceeded 0.6 $m$ (Zanke and

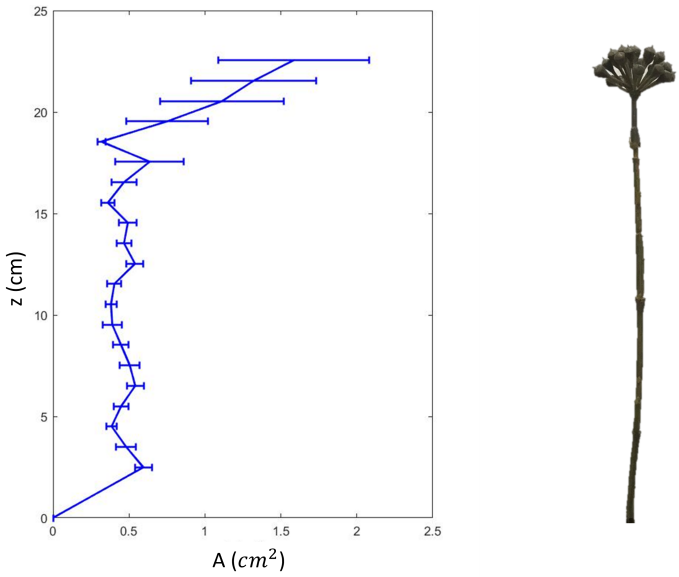


Figure 3.6: Measured frontal area $A(z)$ for the b●●●● setup.

Roland, 2021; Perillo et al., 2014). The heights of the dunes, denoted as $\Delta_\sigma$, were estimated using an empirical formulation proposed by Coleman et al. (2011). This formulation establishes a relationship between the dune height and the standard deviation ($\sigma$) of the bed elevation profile, given by $\Delta_\sigma = 2.2\sigma$. The coefficient 2.2 was empirically derived from laboratory data and field measurements.

Alternative methodologies were considered to validate the measurements related to the bedforms. Lisimenka and Kubicki (2017) proposed a method based on spectral moments of the bed elevation profiles. This approach utilizes the analogy between ocean waves and bedforms, where dune heights are evaluated based on the spectral peak and characteristic dune lengths are associated with the peak frequency. In this study, wavenumbers larger than 0.2 $m^{-1}$, corresponding to wavelengths larger than 5 m, were not considered.

The dune celerity was estimated using the side-view camera recordings. The recorded time period for the experiments ranged from 45 to 90 minutes. This duration was intentionally chosen to be longer than the dune

migration period, which varied from 4.5 to 12 minutes, with the longer duration observed in setups with denser vegetation. A minimum of five complete dunes were tracked in each video. A complete dune is defined as a bed elevation variation that passes through the mean bed level, encompassing the full crest-trough profile. Two different sections were selected in each video frame, and relative bed elevation profiles were extracted using a MATLAB routine. The time lag between the two bed evolution profiles was determined as the first positive peak of the cross-correlation function at a lag greater than zero. By knowing the distance between the two sections, the celerity of the dunes could be estimated (Figure 3.7). These measured celerity values were compared to predictions from three different formulations: the empirical relationship proposed by Tang and Knight (2006) that expresses celerity as a function of hydraulic conditions (water depth $H$ and Froude number $Fr$), the relationship proposed by Heydari et al. (2014) based on dimensional analysis, and the equation proposed by Coleman and Melville (1994) that relates the bedform height to the celerity depending on the shear stress related to the grains. It is worth noting that the Tang and Knight (2006) formulation was developed based on experimental data characterized by sediment sizes ranging from 0.18 to 2.28 mm, slope values in the range of 0.015% to 1.15% and Froude numbers between 0.2 and 0.8. We note also that the Heydari et al. (2014) formulation specifically takes into account sediment with a size of 0.85 mm and Froude numbers ranging from 0.24 to 0.73, and Coleman and Melville (1994) considered sediment sizes of 0.082 and 0.20 mm, Froude numbers spanning from 0.267 to 0.787, and slopes ranging from 0.05 to 0.4 %. Importantly, the experimental data from this present study fall within the ranges covered by all the aforementioned works.

Through a comparative analysis between the measured values and predictions derived from the aforementioned formulations, which were originally developed for non-vegetated conditions, significant insights can be gained into the complex interplay among vegetation, sediment transport, and bedform characteristics, thereby enhancing the understanding of these complex relationships.

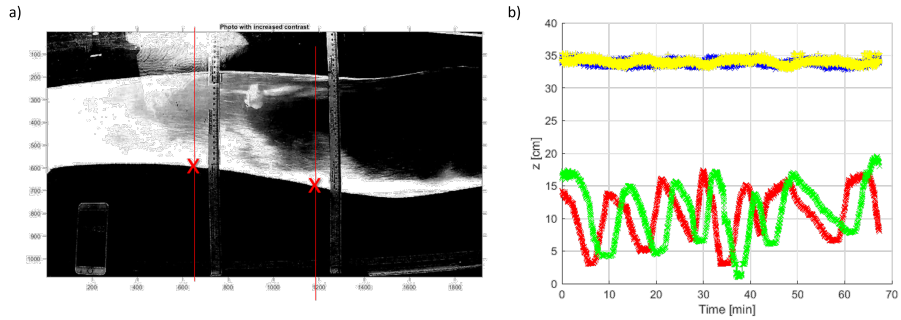


Figure 3.7: Estimation procedure of dune celerity: a) frame of the side-view video, with increased contrast; b) extracted bed evolution profiles (red and green lines) and water surface elevation (yellow and blu lines).

### 3.2.5 Experimental Procedure

The experimental procedure began by setting the foliage configuration of the plants. Once the plants were arranged, the water flow was initiated, and the water discharge and depth were adjusted to achieve just submerged conditions. The hydraulic conditions identified for each experimental run were maintained constant throughout the duration of the experiments until reaching morphological equilibrium (Table 3.4). Morphological equilibrium was assessed by examining the correspondence between the average bed and energy slopes and by monitoring the constancy of sediment transport and bedform characteristics over time, following the criteria established by Simons and Richardson (1966) and Baas (1994). Once morphological equilibrium was achieved, additional data were collected for subsequent analyses. These measurements were obtained during the final four days of each experimental run, providing an average representation of the observed phenomena. Since recirculating flume lumps were observed during the experimental runs through visual analysis of the bed profile evolution, the time required to assess equilibrium for each setup was predicted using the method proposed by Parker (2003). However, these duration predictions $t_0$ were significantly shorter, with a maximum of approximately 12 hours (for the 12•4 setup), compared to the actual duration of the experiments, which ranged between 4 and 10 days (Table

3.4). Differently, bare bed run was conducted over a shorter time period of approximately three hours, consistent with the predicted time duration based on Parker (2003). The flow regime during this run was highly turbulent with significant suspended sediment transport. For this reason, the definition of equilibrium conditions for this specific run relied solely on the constancy of the measured sediment transport over time. To optimize time efficiency, the experiments were conducted sequentially, with each experimental run building upon the final bed conditions of the previous run. The experimental sequence started with the fully foliated setup 1234 and concluded with the bare bed scenario, enabling a gradual increase in flow discharge values from run to run.

All experiments were carried out under spatially-averaged steady uniform flow conditions in which the plants were just submerged. In each experimental run, flow conditions were adjusted by regulating the water level, using a weir located at the end of the flume, and controlling the discharge through a valve. The flume slope was maintained at a constant value of $S = 0.9\%$ for all experimental runs. This slope was predetermined to ensure sediment transport in all setups. To design the experimental conditions, the bed-load transport rate was estimated using the formula proposed by Meyer-Peter and Müller (1948), with the critical Shields number derived using the formulation given by Cao et al. (2006). Thus, all experiments were characterized by comparable total shear stress.

Table 3.4: Experimental hydraulic conditions.

| Setup | Q (l/s) | H (m) | U (m/s) | Fr (-) | $t_0$ (h) | $S_b \pm$ RMSE (%) | $S_E \pm$ RMSE (%) | $a_z H$ (-) | $\Delta Q$ (%) |
|---|---|---|---|---|---|---|---|---|---|
| 1234 | 47.8 | 0.22 | 0.36 | 0.24 | 10.2 | 0.90 ± 0.12 | 0.91 ± 0.01 | 0.207 | -63 |
| 123• | 51.5 | 0.22 | 0.38 | 0.26 | 6.2 | 0.88 ± 0.16 | 0.89 ± 0.01 | 0.194 | -61 |
| 12•4 | 53.0 | 0.23 | 0.39 | 0.26 | 11.2 | 0.85 ± 0.13 | 0.86 ± 0.01 | 0.165 | -59 |
| 12•• | 60.5 | 0.22 | 0.46 | 0.31 | 6.6 | 1.01 ± 0.20 | 0.90 ± 0.02 | 0.120 | -54 |
| 1••• | 73.4 | 0.22 | 0.55 | 0.37 | 5.8 | 0.98 ± 0.19 | 0.87 ± 0.04 | 0.076 | -44 |
| b•••• | 94.1 | 0.23 | 0.69 | 0.46 | 3.6 | 0.86 ± 0.18 | 0.84 ± 0.05 | 0.036 | -28 |
| •••• | 106.1 | 0.22 | 0.81 | 0.55 | $-^*$ | 0.76 ± 0.13 | 0.76 ± 0.06 | 0.016 | -19 |
| bare bed | 130.5 | 0.23 | 0.97 | 0.65 | 2.8 | 0.48 ± 0.14 | 0.52 ± 0.08 | - | 0 |

$*$: the calculation procedure did not converge.

## 3.3 Results

Concerning the turbidity sensors, the output of the measurement system clearly displayed the variability of sediment transport over time. Figure 3.8 illustrates an example of the sinuous trend observed in the instantaneous sediment transport rate, which fluctuated around a mean value and corresponded to the succession of dunes. The time-dependent variability of the measurements, indicated by the standard deviation of the signal $std(Q_s)$, exhibited an increasing trend with the height of the bedforms (Table 3.5).

The relative submergence during the experimental runs was calculated as the ratio of the water depth ($H$) to the deflected plant height ($h_p$) at the highest point of the blossom, both measured at the same vertical. For this estimate, 20-24 different plants within the measurement area were considered. The resulting values for all the setups fell within the range of $1.13 < H/h_p < 1.16$, indicating that the experiments were conducted under similar just-submerged conditions.

In Table 3.4, $\Delta Q$ represents the relative reduction in channel conveyance resulting from the presence of vegetation, relative to the discharge $Q$ observed in the bare-bed setup. Notably, the leafiest setup exhibited a substantial reduction in discharge, approximately 60%, to attain the same just submerged conditions as the other setups. The hydraulic conditions in the bare bed scenario led to increased levels of suspended transport, suggesting an approach towards the upper regime, as further examined in subsequent analyses. This significant deviation from the discharge observed in the bare-bed scenario was unintended and unexpected, as the experimental procedure initially started with the 1234 configuration and concluded with the bare bed scenario. This highlights the influential role of vegetation on flow characteristics and emphasizes the critical need to accurately account for its effects in hydraulic modeling and analysis.

### 3.3.1 Morphological Equilibrium

Regarding the assessment of morphological equilibrium, Figure 3.9 illustrates the temporal evolution of the percentage deviation between the daily-averaged sediment transport measurements $Q_s$ and the value ob-

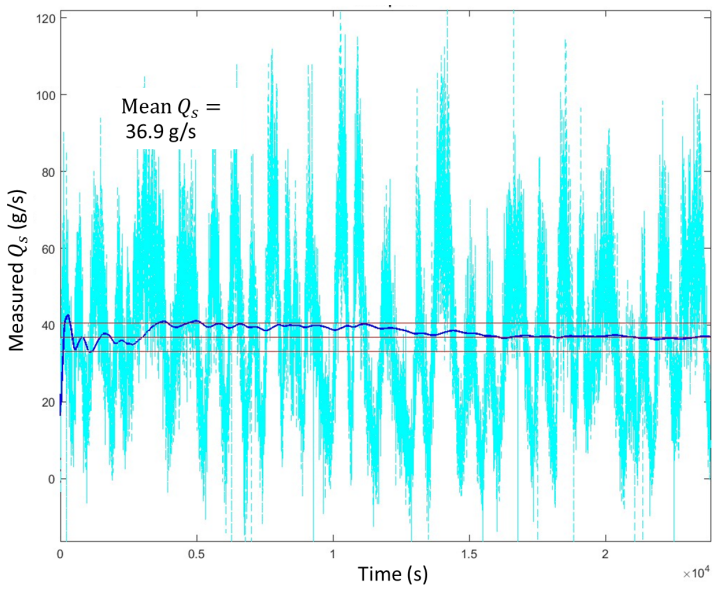


Figure 3.8: The instantaneous sediment discharge is represented by the light blue line, while the dark blue line depicts the cumulative mean sediment discharge over time.

tained from the final measurement. The x-axis represents the duration of the experiment in terms of days, while the y-axis represents the percentage deviation. The plot reveals a fluctuating trend in the percentage deviation over time. Generally, the deviation remains relatively low, with a maximum variation of approximately 4%.

Furthermore, the percentage variation of the dune characteristics over time reflects the trend observed in sediment transport, with a maximum deviation of up to 20% recorded in the final four days of the experiment for both bedform height and wavelength. However, the wavelength measured during b●●●● setup showed a significant deviation of 75% (Figure 3.10).

Thus, a temporal discrepancy in the attainment of the morphological equilibrium was observed in b●●●● setup specifically for the mean dune wavelength.However, this did not imply the unreliability of the collected measurements, as these setups were characterized by an high Froude number, indicating a transition towards the upper regime, as confirmed by

subsequent analyses.

As a result, for the subsequent analyses, the average of measurements taken over the last four days of the experimental runs is considered to represent the morphological equilibrium state. By considering the average over multiple days, the influence of daily variations is mitigated, leading to a more reliable estimate of the overall characteristics of sediment processes.

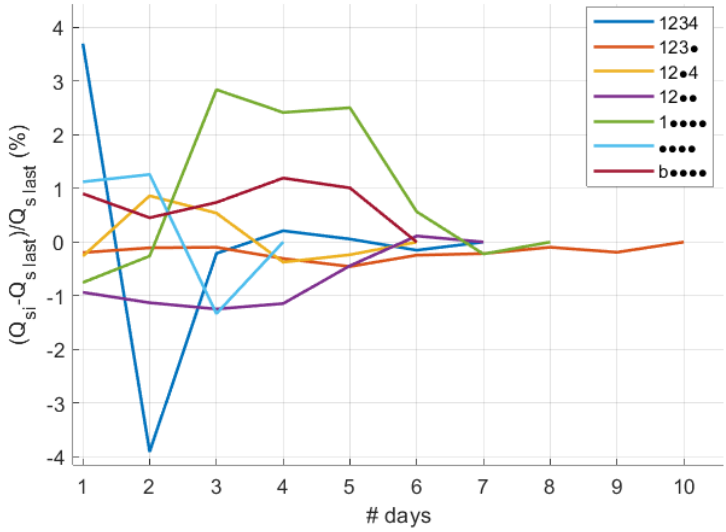


Figure 3.9: Percentage errors between the daily measured sediment transport $Q_s$ and the last-day measure. Each day represents 8 hours.

The energy line was estimated as $E(x) = WSE(x) + \alpha\frac{U(x)^2}{2g}$ where $\alpha \approx 1$ is the Coriolis coefficient (Chow, 1959; Yen, 2002), $U(x)$ is the local flow velocity, $g$ is the gravitational acceleration and $WSE(x)$ is the local water surface elevation measured by means of the scans. The $U(x)$ is calculated considering the local water depth $H(x)$, which is approximated as the difference between the water surface elevation and the bed elevation at x coordinate. As anticipated, the scans of $WSE$ and bed elevation were not performed simultaneously due to the need to suppress sediment transport for accurate measurement of the bed topography. However, the error in estimating the water depth as the difference between these quantities was deemed acceptable. This assessment was based on the

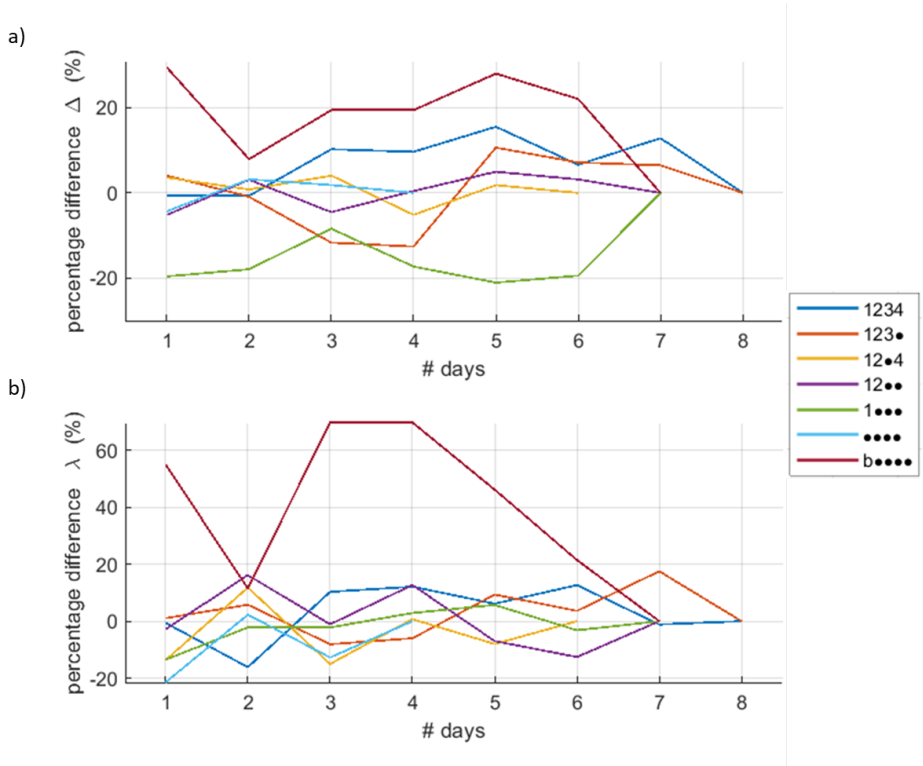


Figure 3.10: Percentage error between the daily measures of dune characteristics and the last-day measure: a) dune height; b) dune wavelength.

observation that the presence of vegetation suppressed the traditional out-of-phase behavior between the bed elevation profile and the water surface. The water surface elevation is influenced by surface waves generated by the presence of vegetation and, in the leafless setups, by the specific hydraulic conditions characteristic of the transition to the upper flow regime.

The uncertainty $u_c$ associated with the energy and average bed slopes is estimated using the 95% confidence interval of the linear fit parameters. On average, the uncertainty is found to be 0.009% for the bed slope $S_b$ and 0.002% for the energy slope. It is worth noting that setups with higher Froude numbers $Fr$, which are associated with surface effects, exhibited larger surface waves, leading to a more pronounced impact on the water surface elevation (Naqshband et al., 2014). In particular, the uncertainty

of the energy slope observed in the bare bed setup ($u_c = 0.004\%$) is 9 times higher than that observed in the 1234 setup ($u_c = 0.0005\%$).

The impact of surface and bed waves on slope determination was evaluated using the root mean square error (RMSE) of the linear regression. The uncertainty for both slopes is calculated using the error propagation theory (Muste et al., 2017), given by:

$$u_c^2(S) = \frac{u_c^2(z)}{(\Delta x)^2} \tag{3.5}$$

The uncertainty $u_c(z)$ associated with the water or bed surface measurement is the RMSE between the measured data $z$ and the regression line data point $z_{fit}$:

$$RMSE = \sqrt{\frac{\sum_{i=1}^{N} (z(i) - z_{fit}(i))^2}{N}} \tag{3.6}$$

The average RMSE was found to be 0.16% for the bottom slope and reduced to 0.04% for the energy slope. These values reflect the uncertainty introduced by both bed and surface waves in the determination of the slopes. It is observed that 12●● and 1●●● setups exhibit a slight deviation of approximately 0.10% from a perfect match between the average bed slope $S_b$ and energy slope $S_E$ (Table 3.4). However, it is important to note that this deviation can be considered negligible in the context of the study. The presence of bedforms in the flow field introduces local non-uniformity, which impacts the flow dynamics across the entire water depth. As a result, minor discrepancies between the measured bed slope and energy slope can arise.

### 3.3.2 Sediment Transport

The measured sediment transport was compared with the predicted values using considered classical sediment transport models based on bed shear stress. The result are summarized in the Table 3.5 and Figure 3.11. The percentage difference between the predicted $Q_{s,p}$ and measured values $Q_{s,m}$ is estimated as:

$$e(\%) = \frac{(Q_{s,p} - Q_{s,m})}{Q_{s,m}} * 100 \tag{3.7}$$

Both the Einstein-Brown (Einstein, 1950; Brown, 1950) and van Rijn (1984a) bed load models provided predictions within a ±30% deviation from the actual sediment transport rates for bare bed or low vegetation frontal area configurations (i.e., 1●●● and lower frontal area). However, for the ●●●● configuration, the deviation between predicted $Q_{s,p}$ and measured $Q_{s,m}$ exceeded 30%. This discrepancy may be attributed to a deviation from morphological equilibrium due to the shorter duration of the experimental run, compared with the others. Furthermore, in b●●●●, ●●●● and bare bed setups, the intensified suspended load and potential limitations in capturing sediments by the drain of the recirculating system may have contributed to this deviation.

In contrast to the other two models, the Wong and Parker (2006) model exhibited substantial differences between the predicted and actual sediment transport rates, for all the setups. This discrepancy suggests that the formula may not accurately capture sediment transport in the presence of dunes. However, it is worth noting that the Wong and Parker (2006) approach has been successfully used in field studies to estimate bed-load transport rates (Cilli et al., 2021). This highlights the need for further investigation to better understand the applicability and limitations of sediment transport models.

Furthermore, it was observed that for the setups with leafy vegetation, there was an increasing deviation from the agreement line as the LAI increased, with deviations reaching up to +80% for the setups with the highest vegetation density. This indicates that the presence of vegetation introduces additional complexities in sediment transport processes that are not captured by the considered bed-shear-stress-based models.

As a result, the measured sediment transport rates in the leafy configurations are significantly higher than the predicted values. These findings contradict previous studies suggesting that vegetation diminishes sediment transport (Yager and Schmeeckle, 2013; Vargas-Luna et al., 2015; Le Bouteiller and Venditti, 2015). Given that bed-load models based on bed shear stress provided reasonable predictions for the setups with lower vegetation density (i.e., 1●●●, b●●●● and ●●●●), it implies possibility of establishing a more precise validity threshold for these models even when vegetation in present.

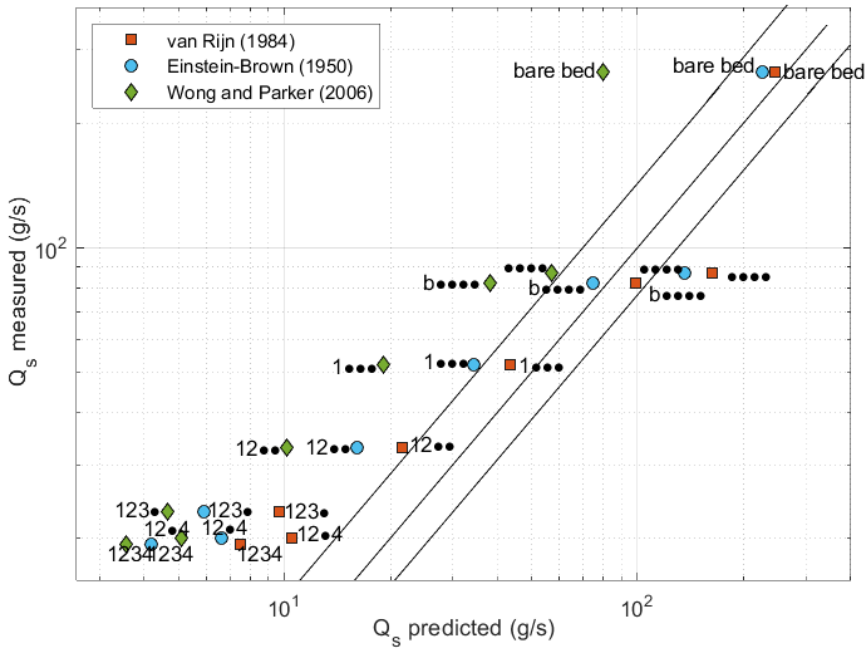


Figure 3.11: Comparison between predicted and measured sediment transport rates. The black lines are the perfect agreement line and those corresponding to a ± 30% deviation.

Considering the conditions of just-submerged vegetation ($H \approx h_p$), the roughness density can be estimated as $\langle a \rangle_z H$, and for the present cases, it ranged from 0.2 to 0 (Table 3.4). Thus, for a roughness density $\langle a \rangle_z H$ <0.08, corresponding to the plant configuration with only the upper branch (1•••• setup), both the Einstein-Brown (Einstein, 1950; Brown, 1950) and van Rijn (1984a) models predicted the measured bed load rate with percentage errors within ± 33% and ± 16%, respectively. These findings suggest that the bed-shear stress-based bed load model remains valid in the presence of vegetation as long as the roughness density $\langle a \rangle_z H$ is less than 0.08.

Moreover, the results obtained in this study emphasize that the presence of leafy vegetation has a notable impact on the flow field, leading to enhanced sediment transport for $\langle a \rangle_z H > 0.08$. This enhancement can be attributed to the significant role of vegetation-generated turbulence

Table 3.5: Sediment transport estimates. Comparison with the outcomes of the "vRijn" van Rijn (1984a) , "EB" Einstein (1950); Brown (1950) and "WP" Wong and Parker (2006) bed load methods. $e$ is the percentage difference between the measured and predicted values.

| Setup | $\tau'_*$ (-) | $Q_s \pm \text{std}(Q_s)$ (g/s) | $Q_s$ (EB) (g/s) | $Q_s$ (vRijn) (g/s) | $Q_s$ (WP) (g/s) | $e$ (EB) (%) | $e$ (vRijn) (%) | $e$ (WP) (%) |
|---|---|---|---|---|---|---|---|---|
| 1234 | 0.082 | 19.3 ± 11.0 | 4.2 | 7.5 | 3.6 | -78 | -61 | -82 |
| 123• | 0.088 | 23.1 ± 13.6 | 5.9 | 9.7 | 4.7 | -74 | -58 | -80 |
| 12•4 | 0.090 | 20.0 ± 13.0 | 6.6 | 10.5 | 5.1 | -67 | -47 | -75 |
| 12•• | 0.114 | 32.9 ± 20.4 | 16.1 | 21.6 | 10.1 | -51 | -34 | -69 |
| 1••• | 0.146 | 52.2 ± 33.3 | 34.4 | 43.6 | 19.0 | -34 | -16 | -64 |
| b•••• | 0.200 | 82.0 ± 56.1 | 74.6 | 99.3 | 38.2 | -9 | 21 | -53 |
| •••• | 0.244 | 87.14 ± 54.5 | 135.6 | 162.4 | 57.3 | 56 | 86 | -34 |
| bare bed | 0.289 | 266.0 ± 177.0 | 226.2 | 244.5 | 79.8 | -15 | -8 | -70 |

in promoting sediment movement. It is important to note that previous studies, which primarily used rigid cylinders as a simplified representation of vegetation, reported a reduction in sediment transport with vegetation. However, it should be noted that these findings are specifically related to the considered vegetation density.

### 3.3.3 Dune Characteristics

The dune characteristics exhibited variations in response to the different hydraulic conditions across the setups. As flow discharge increased and the leaf area index decreased, the dune height ($\Delta_\sigma$) showed an initial phase of rapid growth followed by a subsequent decay. This decay became more pronounced in the 1••• and subsequent setups. Based on these observations, it can be inferred that the setups with higher flow discharges, starting from 1••• setup, are transitioning towards the upper stage plane bed regime. The decay or washing out of the dunes, as observed during these runs, is commonly associated with the erosion of dune crests, which is facilitated by higher suspended load (Naqshband et al., 2017).

A comparison was made between the estimated dune wavelengths $\lambda_{crest}$ and heights $\Delta_\sigma$ and the outcomes obtained from the spectral method (de-

noted with subscript "psd") developed by Lisimenka and Kubicki (2017). Table 3.6 and Figure 3.12 illustrates the comparisons between these estimates. The percentage error deviation between the "psd" estimate and the values of $\lambda_{crest}$ and $\Delta_\sigma$ was calculated using the following equation:

$$e(\lambda) = \frac{\lambda_{psd} - \lambda_{crest}}{\lambda_{psd}} \qquad e(\Delta) = \frac{\Delta_{psd} - \Delta_\sigma}{\Delta_{psd}} \tag{3.8}$$

Generally, both methods resulted in similar estimates of average heights and wavelengths for the dunes, thereby confirming the measurements. However, it is important to notice that the average percentage error between the two estimates of wavelength was higher compared to that obtained for the dune heights, specifically 12.7% compared to 1.5%. This deviation in the wavelength estimates may be attributed to the different employed methods. The method proposed by Lisimenka and Kubicki (2017) relates the characteristic length of the dune to the peak of the spatial spectra, which could be influenced by the presence of secondary bedforms or the presence of plants. Furthermore, the higher percentage error observed for the bare bed scenario may be associated with the fact that the dunes might still be in the development stage during the measurements (as discussed in Section 3.2.5).

Existing formulations for predicting bedform characteristics have traditionally been developed in the absence of vegetation. Consequently, conducting a comparison between the predicted values obtained from these models and the measured values derived from the experimental activities offers valuable insights into the influence of vegetation on bedform geometry and dynamics.

The observed dune dimensions were compared with the estimates predicted by means of van Rijn (1984b) formulation for wavelength and heights. The comparison is reported in Figure 3.13. Significantly, the measured data demonstrate a consistent trend with the original curves, despite a noticeable shift.

Regarding the dune height, it is noteworthy that the 123• and 12•• setups exhibit closer agreement with the predicted values. However, in setups with the presence of the lowest leaves, there is a percentage error of 50÷60% (Table 3.6) between the observed and predicted dune heights.

Table 3.6: Estimated dunes characteristics. $e(\Delta)$ and $e(\lambda)$ are the percentage errors between the measured and predicted dune height and wavelength; $e(\Delta/H)$ and $e(\Delta/\lambda)$ are the percentage errors between the observed data and the predictions obtained from van Rijn (1984b) formulations.

| Setup | $\Delta_{psd}$ (cm) | $\Delta_{\sigma}$ (cm) | $e(\Delta)$ (%) | $\lambda_{psd}$ (cm) | $\lambda_{crest} \pm {}^{a}S.E.$ (cm) | $e(\lambda)$ (%) | $e(\Delta/H)$ (%) | $e(\Delta/\lambda)$ (%) |
|---|---|---|---|---|---|---|---|---|
| 1234 | 3.56 | 3.46 | 2.8 | 69.42 | 62.82 ± 4.56 | 9.5 | -62 | 37 |
| 123• | 5.68 | 5.43 | 4.4 | 82.88 | 79.71 ± 5.16 | 3.8 | -12 | 46 |
| 12•4 | 4.24 | 4.13 | 2.6 | 78.00 | 68.50 ± 6.83 | 12.2 | -51 | 37 |
| 12•• | 7.06 | 6.88 | 2.5 | 103.62 | 94.74 ± 9.99 | 8.6 | -5 | 38 |
| 1••• | 6.94 | 6.71 | 3.3 | 111.68 | 105.93 ± 7.79 | 5.1 | -21 | 21 |
| b•••• | 6.24 | 6.27 | -0.5 | 148.99 | 127.96 ± 12.50 | 14.1 | -37 | -5 |
| •••• | 4.60 | 4.53 | 1.5 | 112.18 | 92.66 ± 9.33 | 17.4 | -79 | -3 |
| bare bed | 4.88 | 5.10 | -4.5 | 200.92 | 138.72 ± 15.92 | 31.0 | -53 | -29 |

*a*: standard error S.E.= $SD/\sqrt{n}$ with n numbers of dunes observed in the considered profile.

This suggests that the lower branch may have a potential impact on sediment motion and consequently affect the resulting dune heights. Considering a decreasing vegetation density order and starting from the 1••• setup, the predicted values deviate significantly from the measured data as illustrated in Figure 3.13a. The predicted curve consistently exhibits values approximately 50% lower than the original data. This deviation is in line with the observed reduction in dune height, which reflects the transition towards the upper flow regime that characterizes these specific setups, as already discussed. Nevertheless, it is possible to note that starting from 1••• setup and reducing the vegetation frontal area until bare bed conditions, the Froude number in these setups exceeded 0.37. According to Naqshband et al. (2014), Froude numbers within the range of 0.32 to 0.84 are associated with large free surface undulations that have a significant impact on bed morphology. These undulations lead to a rapid decrease in bedform height as suspended transport increases.

Regarding dune steepness and considering the predicted height values, the graphical comparison indicates that the presence of vegetation tends to

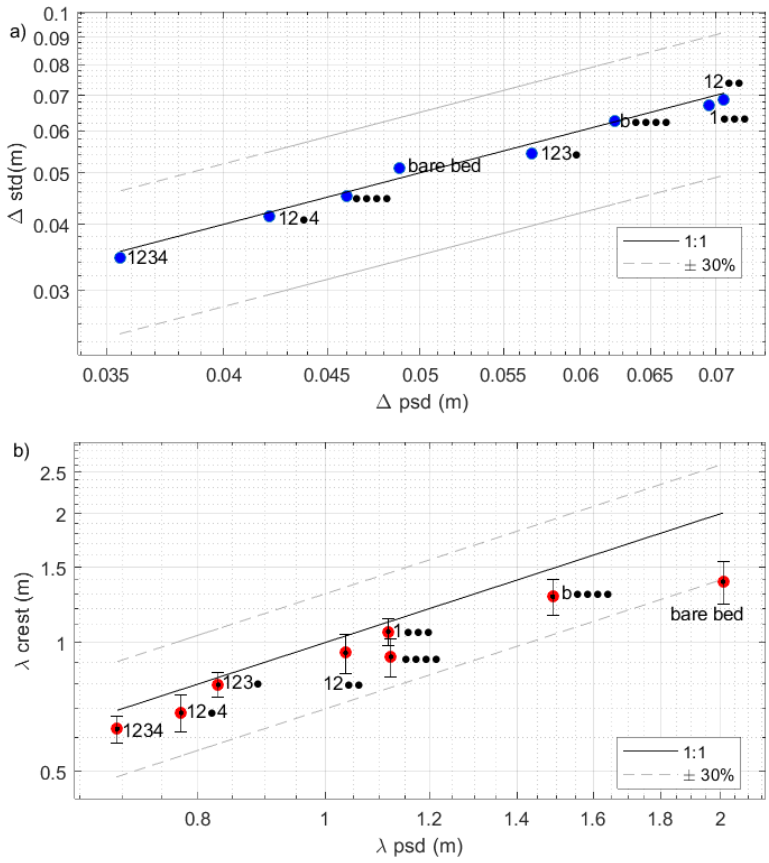


Figure 3.12: Comparison of the average dune characteristics obtained from the considered methods: a) dune heights; b) dune wavelength. The error bars represent the standard error of the estimated values.

increase dune steepness and thus reduce average wavelengths by approximately 60% for leafy setups. In contrast, the steepness predicted under leafless conditions aligns with the measured values, suggesting that the presence of leafless vegetation not only reduces the average dune height but also affects the wavelength. Moreover, it is hypothesized that for the bare bed scenario, the increased deviation is due to the specific hydraulic conditions.

In bare bed channels, the bed load transport rate can be expressed

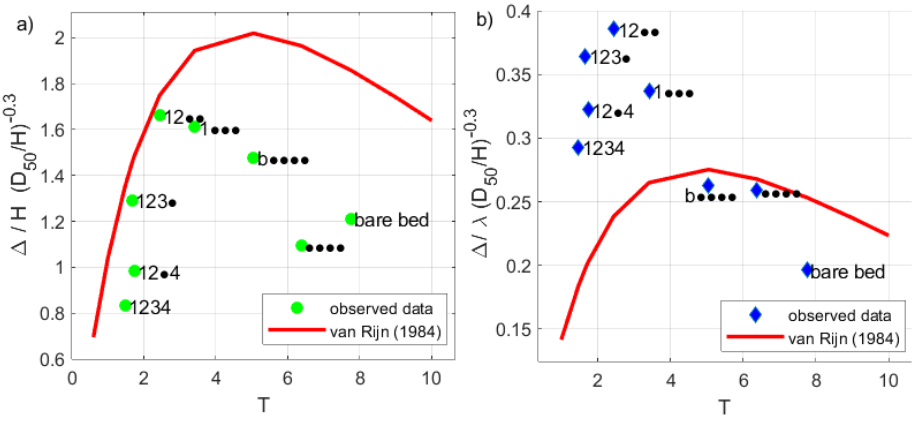


Figure 3.13: Comparison between observed and predicted values from van Rijn (1984b) formulations: a) dunes heights; b) dunes steepness.

as a volumetric sediment flux associated with the migration of bedforms (Simons et al., 1965):

$$Q_{s,dune} = \beta \rho_s (1-p) c \Delta \tag{3.9}$$

where $\beta = 0.5$ is the shape coefficient factor, assuming triangular shape, $p = 0.4$ is the sand porosity, $c$ and $\Delta$ is the bedform celerity and height, respectively. Table 3.7 reported the percentage error $e(Q_s)$ between the measured sediment transport rates and the values calculated using the sediment mass conservation principle (Simons et al., 1965). The average percentage error is $\approx 20\%$, suggesting that the method is generally valid for obtaining an approximation of the bed load rates based on the dune geometries, even in the presence of complicated bed morphology as herein considered. Therefore, the average dune height estimated through longitudinal scans appears to be a reliable indicator of dune geometry, even for three-dimensional (3D) dunes (see Section 3.3.4). In contrast, the slightly higher percentage error observed for b●●●●, ●●●● and bare bed setups may be attributed to the increased presence of suspended sediment, that is not considered in the Simons et al. (1965) model.

Concerning the observed dune celerity and the potential effects exerted by the presence of vegetation on it, the measured values were compared with the predictions based on the considered empirical relationships,

namely Tang and Knight (2006),Heydari et al. (2014) and Coleman and Melville (1994). The results are reported in Table 3.7 and Figure 3.14a. The comparison indicates that only the bare bed and bare stem setups deviate within 30% from the agreement line. This suggests that the validity of the method may be compromised in the presence of leafy vegetation and that the bare stem setups have a minimal influence on bedform celerity. The formulation introduced by Heydari et al. (2014) generally lacks strong correspondence with the observed celerity. In contrast, the empirical equation proposed by Coleman and Melville (1994) demonstrates notable alignment between predicted and observed celerity for most of the considered setups. Furthermore, the formulation presented by Tang and Knight (2006) consistently underestimates celerity in setups characterized by leafy vegetation. Assuming that predictive formulations for bedform celerity are meant to represent conditions without vegetation, and considering the results obtained for the bed-load transport rate, wherein the measured bed load transport exceeded the predicted values for the leafiest setups, it can be inferred that the Tang and Knight (2006) formulation provides a better fit to the present data. Similarly to the results obtained for the bed-load transport rate, the percentage error between the observed celerity and the predicted values through the Tang and Knight (2006) formula increases with increasing LAI. In other words, the presence of leafy vegetation seems to result in increased bedform celerity compared to the predictions made by available formulations that represent related non-vegetated conditions.

To further examine the influence of vegetation on bedform celerity, Figure 3.14b shows the ratio of measured bed-load transport rate $Q_{s,m}$ to the predicted bed-load transport rate $Q_{s,dune}$ based on the Simons et al. (1965) equation. The ratio is plotted as a function of the solid volume fraction $\phi$ of the plants. Notably, as $\phi$ increases, the measured sediment transport rates $Q_{s,m}$ gradually approach and even surpass the values estimated based on bedform geometry $Q_{s,dune}$, particularly for setups with higher LAI. This trend is more evident as the vegetation density increases. Consequently, the collected data suggest that bed load transport rates appear to be enhanced in the presence of leafy flexible plants, especially when the leaves are in close proximity to the bottom (fourth branch). This phe-

nomenon may be attributed to increased turbulence resulting from the presence of leaves, which leads to sediment resuspension and facilitates its transportation.

Contrary to the findings reported by Duan and Al-Asadi (2022), which suggested that the presence of vegetation decreases sediment transport, the present study reveals a different trend. As the solid volume fraction $\phi$ of the plants increases, indicating a higher density of vegetation, an enhancement in sediment transport rates is observed. Similarly, the study by Yang and Nepf (2019) also reported the suppression of bedform development by vegetation, further contrasting the findings of this study. It's important to note that both the studies by Duan and Al-Asadi (2022) and Yang and Nepf (2019) considered rigid cylinders.

Moreover, it is worth noting that both bare stems and bare bed setups exhibited bed-load rates that exceeded the predicted values. This discrepancy could be attributed to the occurrence of suspended sediment transport during these runs, which cannot be accurately predicted solely based on bedform geometry using the Simons et al. (1965) equation.

Additionally, the ratio of the observed celerity and the predicted values through Tang and Knight (2006) model were plotted as a function of the vegetation frontal area $\langle a \rangle_z$ in Figure 3.14c. It is possible to note that the data points align along a line given by the equation:

$$c_m/c_{p,TK} = 10.24\langle a \rangle_z \tag{3.10}$$

For the ●●●● and bare bed setup, $c_m/c_{p,TK} \approx 1$, suggesting that the estimates closely approximate the predicted values assumed for a bare bed scenario. This suggests that the presence of bare stems has minimal impact on the flow structure and does not significantly alter the celerity of the dunes. On the other hand, for setups with leafy plants, the observed celerity is significantly enhanced compared to the predictions made in the absence of vegetation.

As a result, this study suggests that the presence of vegetation seems to play a significant role in augmenting sediment transport rates. This phenomenon can be attributed to the combined effects of vegetation-induced turbulence and the presence of bedforms, highlighting the intricate interplay between vegetation and bedform dynamics in sediment transport

processes.

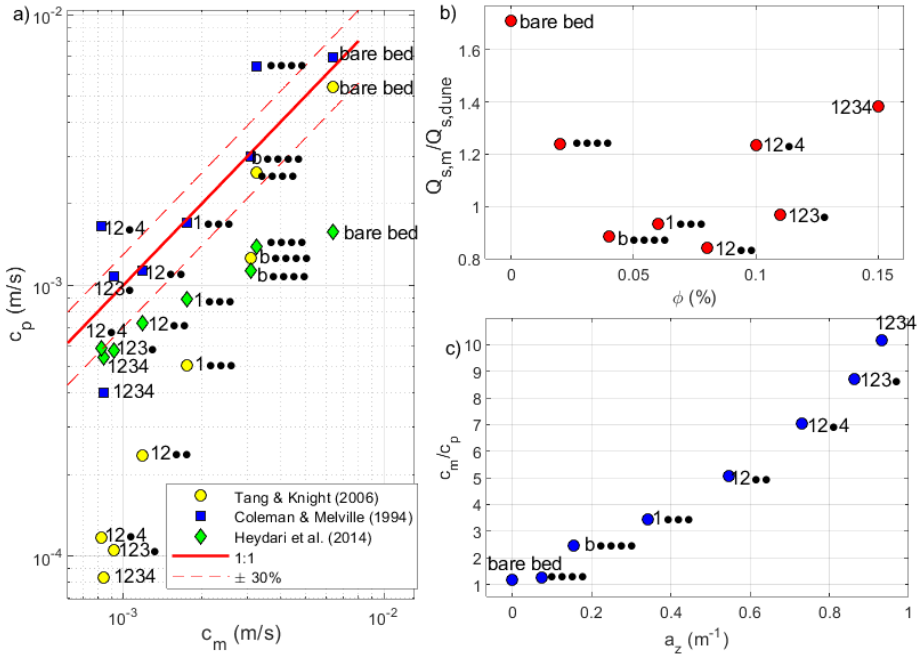


Figure 3.14: Dunes celerity estimates: a) comparison between measured and predicted values; b): ratio of measured bed-load $Q_{s,m}$ and estimated values $Q_{s,dune}$ based on dune geometry using Simons et al. (1965) equation; c: ratio of observed celerity $c_m$ and predicted values through Tang and Knight (2006) model.

### 3.3.4 Impact of Vegetation on Three-Dimensional Geometry

In addition of the results presented so far, a further analysis was conducted to investigate the influence of vegetation on the three-dimensionality of the dune geometry. In this analysis, bedform stability diagrams available in the literature were examined, with a specific focus on the phase diagram proposed by Southard and Boguchwal (1990). This diagram is used to delineate the hydraulic conditions under which three-dimensional (3D) dunes can form instead of two-dimensional (2D) dunes. The diagram

Table 3.7: Dune celerity: $c_m$ is an average values of the videos recorded during the experiments; $c_{p,TK}$ is the obtained value from Tang and Knight (2006)' celerity formulation, $c_{p,H}$ from Heydari et al. (2014) and $c_{p,CM}$ from Coleman and Melville (1994); $e$ is the relative error between the predicted and observed quantities.

| Setup | $Q_{s,dune}$ $(g/s)$ | $c_m$ $(m/s)$ | $e(Q_s)$ (%) | $e(c_{p,TK})$ (%) | $e(c_{p,H})$ (%) | $e(c_{p,CM})$ (%) |
|---|---|---|---|---|---|---|
| 1234 | 13.9 | 8.4E-04 | 28 | 90 | 36 | 111 |
| 123• | 23.8 | 9.2E-04 | -3 | 89 | 38 | -14 |
| 12•4 | 16.3 | 8.3E-04 | 19 | 86 | 29 | -50 |
| 12•• | 39.1 | 1.2E-03 | -19 | 80 | 39 | 6 |
| 1••• | 56.0 | 1.8E-03 | -7 | 71 | 49 | 3 |
| b•••• | 70.2 | 3.1E-03 | -13 | 59 | 57 | -49 |
| •••• | 92.7 | 3.3E-03 | 19 | 20 | 63 | 3 |
| bare bed | 155.7 | 6.4E-03 | 41 | 15 | 75 | -8 |

refers to the temperature-standardized depth $d_{10}$, flow velocity $U_{10}$, and sediment size $D_{10}$. These 10°C-equivalent quantities were estimated assuming negligible variation in water density with temperature, using the following equations:

$$H_{10} = H\left(\frac{\mu_{10}}{\mu}\right)^{\frac{2}{3}}; \quad D_{10} = D\left(\frac{\mu_{10}}{\mu}\right)^{\frac{2}{3}}; \quad U_{10} = U\left(\frac{\mu_{10}}{\mu}\right)^{\frac{1}{3}} \tag{3.11}$$

Where $D_{10}$ =1.02 mm, $\mu_{10}$=1.3076×10 $^{-3}$ is the 10°C dynamic viscosity, $D$ is the reference sediment size $D = D_{50}$. The relationship used to estimate $\mu$ as a function of temperature is based on the work of Popiel and Wojtkowiak (1998) and has been previously applied in studies such as Zonta et al. (2012). The water temperature during the experimental runs was measured using an Acoustic Doppler Velocimeter (ADV).

The results of this analysis are summarized in Figure 3.15a. Notably, the diagram predicts a three-dimensional geometry for the setups with the lowest vegetation density, specifically b•••• and •••• setups. On the other hand, the setups characterized by the highest vegetation density are classified as lower plane conditions. However, it is important to note that the corresponding section of the graph is labeled as "gradual," implying that

Table 3.8: Bedforms characteristics analysis: 10°C-equivalent velocity $U_{10}$ and water depth $H_{10}$ and dynamic viscosity $\mu$, non dimensional span ($NDS$).

| Setup | $\mu$ ($Nsm^{-2}$) | $U_{10}$ (m/s) | $H_{10}$ (m) | NDS ± S.E.[a] (-) |
|---|---|---|---|---|
| 1234 | 9.87E-04 | 0.39 | 0.27 | 1.32 ± 0.06 |
| 123• | 1.02E-03 | 0.42 | 0.27 | 1.12 ± 0.04 |
| 12•4 | 1.06E-03 | 0.42 | 0.26 | 1.29 ± 0.07 |
| 12•• | 1.03E-03 | 0.50 | 0.26 | 1.10 ± 0.02 |
| 1••• | 1.03E-03 | 0.60 | 0.26 | 1.09 ± 0.03 |
| b•••• | 1.03E-03 | 0.75 | 0.27 | 1.33 ± 0.07 |
| •••• | 1.06E-03 | 0.86 | 0.25 | 1.26 ± 0.02 |
| bare bed | 1.08E-03 | 1.03 | 0.26 | 1.37 ± 0.10 |

a: standard error S.E.= $SD/\sqrt{n}$ with n numbers of dunes observed.

the possibility of two-dimensional dunes cannot be completely excluded for these leafiest setups.

The classification of bedform geometry obtained from the Southard and Boguchwal (1990) diagram was further compared to the classification proposed by Venditti et al. (2005) based on the observed non-dimensional span (NDS) or sinuosity of the dunes. The NDS represents the ratio of the linear distance between the ends of the crestline to the actual length of the crestline being analyzed. A value exceeding 1.2 indicates the presence of three-dimensional dunes with highly sinuous crestlines (Venditti et al., 2005). To calculate the NDS, the DEMs of the final bed topography resulting from each experimental run were utilized (Figure 3.15b). As previously mentioned, these DEMs were constructed by processing photographs taken at the end of each experimental run using the Structure-from-Motion technique (SfM). The SfM technique enabled the reconstruction of the three-dimensional surface, providing a detailed representation of the final topography shaped by the interaction between vegetation and hydraulic conditions during the experiments.

According to the NDS classification, only setup 123•, 12•• and 1••• were classified as two-dimensional (2D), as reported in Table 3.8. Significantly, the setups characterized by the presence of the lowest branch, which

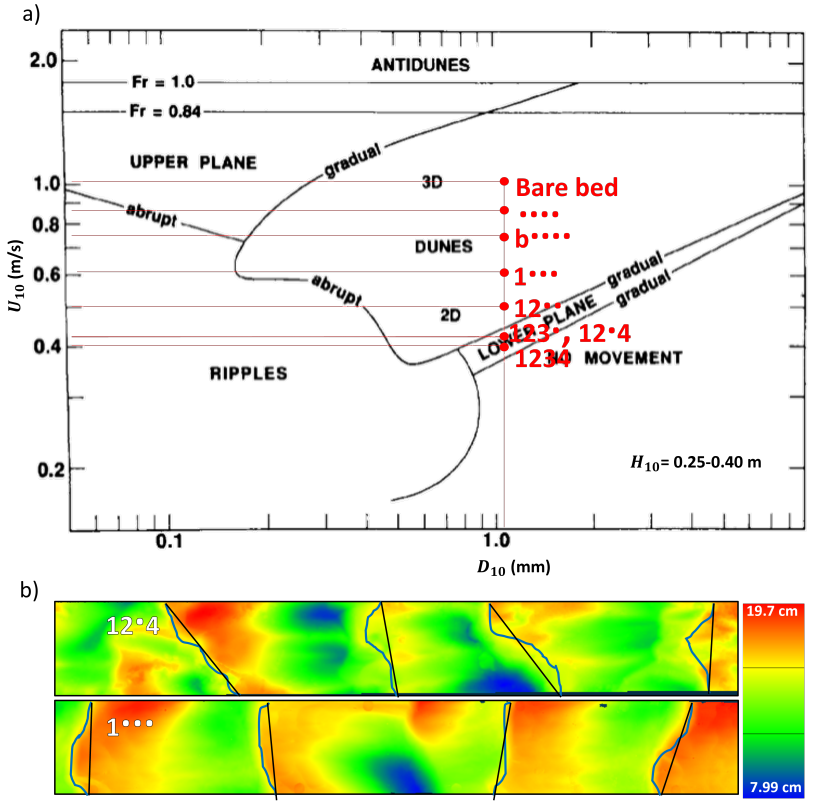


Figure 3.15: Dune classification: a) bedforms stability diagram proposed by Southard and Boguchwal (1990), for $H_{10}$ ranged between 0.25 and 0.40 m; b) example of NDS estimation for 12•4 and 1••• setups.

were initially predicted as 2D dunes based on the Southard and Boguchwal (1990) phase diagram, demonstrated an unexpected three-dimensional structure. This highlights the substantial impact of the lowest branch of the plant on the dune geometries, leading to a three-dimensional configuration. This is underlined by the observed interaction during the experiments, wherein the mobile dunes actively covered and enveloped the leaves of the lowest branch during their movement. Conversely, for setups without the fourth branch, both the classification based on Venditti et al. (2005) and the bedforms stability diagram proposed by Southard and Boguchwal (1990) were in agreement.

## 3.4 Conclusions

In conclusion, the results of this analysis shed light on the limitations of existing models in predicting sediment transport and bedform characteristics in open channels covered by leafy flexible vegetation. The examination of various formulations and methodologies to predict dune geometry and celerity provided insights into the influence of leafy flexible vegetation on dune characteristics. The findings of this study suggest that the presence of vegetation has an impact on dune characteristics. Specifically, it is observed that the average dune wavelength tends to decrease in the presence of vegetation. Additionally, the observed dune celerity deviates from the predicted estimates based on bare bed conditions, and this deviation becomes more pronounced with increasing vegetation frontal area ($\langle a \rangle_z$). The comparison between the measured and predicted bed-load transport rate using models based on bed shear stress shows that predictions within a 30% percentage error are obtained for setups with lower vegetation roughness ($\langle a \rangle_z H < 0.08$). However, significant deviations occur for setups with denser vegetation, indicating the limitations of the models in accurately predicting bed-load transport rate in such conditions. Furthermore, the results highlight that the bed load transport rate seems to be enhanced in the presence of leafy flexible plants, potentially due to the increased turbulence associated with the presence of leaves.

Further investigation into the turbulence characteristics during flow over dunes and in the presence of leafy vegetation would enhance the understanding of the link between leaf-scale turbulence and sediment transport. Conducting further studies under mobile bed conditions and incorporating various densities of leafy flexible vegetation will provide valuable insights into the complex interactions among flow, vegetation, and sediment processes. These insights will contribute to improving the accuracy of models to predict the morphological evolution of river systems.

# Chapter 4

# Effects of Flexible Just-submerged Vegetation and Dunes on Flow Field

## 4.1 Introduction

Despite the well known phenomenon that vegetation primarily reduces flow velocity and enhances deposition, recent studies have uncovered its potential to promote sediment resuspension, thereby impacting sediment transport. For instance, Tinoco and Coco (2016) demonstrated that in the presence of rigid cylinders, the vegetation-generated turbulence increases, leading to sediment being lifted into suspension. Similarly, Yang et al. (2016) found that vegetated channels have a lower critical shear velocity for incipient sediment motion compared to bare bed conditions, indicating easier sediment mobilization. Furthermore, Yang and Nepf (2018) highlighted the role of turbulence, rather than bed shear stress, in driving sediment transport, suggesting that turbulent kinetic energy can serve as a predictor for bed load in both bare and vegetated beds. The inadequacy of current bed-load transport models, which are based on time-averaged bed shear stress, in the presence of obstacles like bedforms and vegetation has been recognized (Yang and Nepf, 2019; Yager and Schmeeckle, 2013). Nelson et al. (1995) observed that turbulence structures signif-

icantly affect sediment transport without influencing time-averaged bed shear stress, emphasizing the importance of coupling turbulence and sediment transport.

The majority of prior investigations into turbulence fields in vegetated channels have predominantly centered on simplified vegetation models, such as rigid cylinders or regular flexible blades (Ghisalberti and Nepf, 2006; Huai et al., 2019; Tanino and Nepf, 2008b; Tinoco and Coco, 2016). However, these simplified models are inadequate to capture the complete hydraulic behavior of more realistic leafy vegetation. To date, only a few studies have considered more natural-like leafy vegetation models (Xu and Nepf, 2020).

Although previous studies have primarily examined turbulent flows within vegetation positioned on flat beds (Ghisalberti and Nepf, 2006), it is crucial to account for the complex and heterogeneous bed topography observed in natural river systems. These riverbeds frequently exhibit surface undulations or bedforms generated in response to sediment transport. In particular, flow over dunes, which are the predominant bedforms in alluvial channels, exhibits intricate characteristics with large-scale turbulence associated with flow separation at the crest (Best, 2005). Poggi et al. (2007) conducted experiments considering flows with vegetation over gently undulating beds and observed significant changes in pressure and velocity fields even with small variations in topography. This highlights the crucial role of bed topography in determining flow characteristics within vegetated channels. Hence, the consideration of the influence of complex and heterogeneous bed topography in flow hydrodynamics is crucial for advancing the understanding in this field.

Considering that many laboratory studies have primarily focused on investigating flow over two-dimensional fixed dunes, it is important to note that these studies do not fully capture the complex geometry dominated by three-dimensional (3D) structures observed in natural river bedforms (McLean et al., 2008; Maddux et al., 2003b). Maddux et al. (2003b) found that 3D dunes generate more friction and exhibit reduced turbulence compared to 2D dunes. They also observed higher dispersive stress values throughout the water depth for 3D dunes, whereas dispersive stress in the presence of 2D dunes can be considered negligible above the crest.

Many studies have focused on fixed bed conditions when designing experiments involving bedforms (Maddux et al., 2003b; Unsworth et al., 2018). However, conducting and analyzing experiments under fixed bed conditions neglects the different flow structures associated with sediment motion (Nikora and Goring, 2000). Understanding the complex interaction between flow, vegetation, and sediment processes is crucial for the proper and effective employment of vegetation in river restoration practices (Termini, 2015).

Moreover, in scenarios where vegetation and large-scale bedforms like dunes may coexist, such as in natural alluvial floodplains, the prediction of turbulence characteristics becomes extremely challenging due to the combined effects of both sources. Kabiri et al. (2017) demonstrated that, for the same fixed gravel bedforms, the presence of grass cover significantly affects the flow field and turbulence characteristics, leading to an increase in the length of the separation zone.

This chapter aims to investigate the influence of leafy flexible vegetation on flow velocity and turbulence characteristics across different leaf area index (LAI) configurations over a dune bed. The study involved laboratory experiments to measure velocities, under both fixed and mobile bed conditions. The fixed bed physical model was constructed using the digital elevation model (DEM) of the final topography resulted from the mobile bed experiments (Chapter 3). The double-averaging method was employed to analyze the flow and turbulence fields, facilitating a comprehensive assessment of the effects of vegetation and dunes on flow dynamics. Valuable insights can be gained into the impact of the mobile bed on flow structure by comparing the flow field and turbulence characteristics resulted from both the mobile and fixed bed conditions. Additionally, the study aims to develop an initial predictive bed-load model that integrates the turbulence generated by both leafy flexible vegetation and large-scale bedforms.

## 4.2 Double Averaging Method

A flow over bedforms is characterized by significant spatial variability in all directions. The double averaging method is a widely employed tech-

nique in the study of flow over bedforms, aiming to mitigate spatial and temporal non-uniformities and to analyze the flow field characteristics in such complex environments (Nikora et al., 2007b). In the present case, the double averaging method is applied to overcome and remove the spatial and temporal non-uniformity generated by the presence of the dunes and the vegetation (McLean et al., 2008; Xu and Nepf, 2020). The procedure involves applying spatial averaging to flow parameters that have already been averaged in the time domain. The spatial-averaging procedure can be defined as follows:

$$\langle \Theta \rangle (x, y, z, t) = \frac{1}{V_f} \int_{V_f} \Theta dV \tag{4.1}$$

where $\Theta$ is a flow variable, $V_f$ is the volume occupied by the fluid within the considered $x - y$ area at level $z$ (Nikora et al., 2001). In presence of bedforms, the averaging domain may be partially filled with sediment and thus, in Equation 4.1, $\Theta$ is defined in the fluid volume $V_f$ and not in the volume occupied by the sediment.

In the double averaging procedure, the variables are expressed referring to Reynolds' decomposition $\Theta = \overline{\Theta} + \Theta'$ and the extension for the time-averaged variables $\bar{\Theta} = \langle \overline{\Theta} \rangle + \tilde{\Theta}$, where the overbar represents the time-averaged variable and the brackets $\langle \rangle$ represents the spatial averaged variable (Nikora et al., 2007b). Thus, $\tilde{\Theta}$ is the spatial fluctuation in the time-averaged flow variable and $\langle \overline{\Theta} \rangle$ is the double averaged variable.

McLean and Nikora (2006) and McLean et al. (2008) have observed that the shape of double-averaged velocity profiles varies depending on the reference level of the averaging domain. In rough flows, the hydraulic parameters are usually double averaged considering thin horizontal slabs parallel to the mean smoothed bed surface (Nikora et al., 2007a; McLean et al., 2008; Aberle et al., 2008; McLean and Nikora, 2006). Smith and McLean (1977) demonstrated that by double-averaging the Reynolds stress only over the stoss side of a dune (from the reattachment point to the crest), it is possible to infer the skin friction based on the slope of the near-bed double-averaged velocity profile, while the combination of skin friction and form drag can be inferred from the slope of the outer part of the profile (1.5 bedform heights from the dune crest). The first application of the double averaging method on a wavy bed was conducted by Smith and

McLean (1977), who performed the double averaging procedure solely on the stoss side at the x-y plane, at the same distance from the local bed. Highlighting the significance of the reference level in the double averaging method, McLean et al. (2008) argued that this approach is prone to errors as it excludes the flow separation zone from the analysis. The authors emphasized that the double averaging over a horizontal thin slab volume enables the integration of the conservation of mass and momentum equations, resulting in a more comprehensive analysis.

## 4.3 Turbulence-based bed-load model

Turbulence kinetic energy ($k_t$) is widely used to characterize the temporal and spatial changes of a turbulent flow and is defined as:

$$k_t = \frac{1}{2}\left(\overline{u'^2} + \overline{v'^2} + \overline{w'^2}\right) \tag{4.2}$$

where $u', v'$ and $w'$ are the instantaneous velocities in the x,y,z directions, respectively.

In bare bed conditions, the turbulence $k_t$ is correlated with bed shear stress $\tau_b$ as $k_t = \tau_b/0.19\rho$ where $\rho$ is the water density (Hofland and Battjes, 2006; Stapleton and Huntley, 1995). However, in vegetated channels, $k_t$ is not solely produced by the bed, but also by the presence of vegetation. As a result, $k_t$ does not scale with the bed shear stress $\tau_b$.

A study conducted by Yang and Nepf (2018) demonstrated that the bed load transport rate, $Q_s$, is related to the near-bed turbulent kinetic energy $k_t$ in both bare and vegetated beds. In their study, Yang and Nepf (2018) modified the Einstein-Brown bed-load model replacing the dependence on bed shear stress with the near-bed turbulent kinetic energy $k_t$, through the substitution $\tau_b = \rho 0.19 k_t$. This modification resulted in the following expression:

$$q_s^* = \begin{cases} 2.15e^{-2.06/k_t^*}, & \text{if } k_t^* < 0.95. \\ 0.27{k_t^*}^3, & \text{if } 0.95 < k_t^* < 2.74. \end{cases} \tag{4.3}$$

where $q_s^*$ and $k_t^*$ are the dimensionless transport rate and turbulent kinetic

energy, respectively:

$$q_s* = \frac{q_s}{\rho_s \omega_0 D_{50}}, \quad k_t^* = \frac{k_t}{(\rho_s/\rho - 1) g D_{50}} \tag{4.4}$$

where $q_s$ is the sediment transport per unit width, $\rho$ the water density, $\rho_s$ the sediment density ($2650 kg/m^3$), $\omega_0$ particle fall velocity (Dietrich, 1982) and $D_{50}$ sand characteristic diameter.

In Equation 4.3, Yang and Nepf (2018) considered near-bed $k_t$ measured at 2 cm from the mean bed level. This distance coincided with the average height of ripples, as the authors observed a drop in velocity data quality closer to the bottom. Previous studies with same model vegetation (Yang et al., 2015), have shown a uniform vertical trend of $k_t$ above the boundary layer, with a height estimated to be less than 3 mm. Therefore, the measurements at 2 cm were assumed to be representative of the maximum near-bed $k_t$. Furthermore, the model (Equation 4.3) has been validated in presence of rigid cylinders and mobile ripples by Yang and Nepf (2019).

Most studies focusing on vegetation-generated turbulence have proposed predictive models that are valid only under limited conditions, such as rigid cylinders and fixed-bed conditions (Yang and Nepf, 2019). Based on the equation developed by Tanino and Nepf (2008b) for predicting vegetation-generated turbulence as a function of the vegetation solid volume fraction $\phi$ and drag coefficient $C_D$, Yang et al. (2016) derived an expression to calculate the near-bed turbulent kinetic energy as the sum of bed-related and vegetation-related turbulence:

$$k_t = k_{t,b} + k_{t,v} = \frac{\tau}{0.19\rho} + \delta \left( C_D \frac{\phi}{(1-\phi)\pi/2} \right)^{2/3} U^2 \tag{4.5}$$

where $U$ the flow velocity and $\delta = 1.2$ is a scaling constant.

The vegetative term in Equation 4.5 was determined for rigid cylinders and is valid for $d/s_n < 0.56$, where $s_n$ represents the surface-to-surface distance between vegetation elements. This equation applies in the presence of stem-generated turbulence, which has been observed at stem Reynolds numbers $Re_d = Ud/\nu > 200$, with $d$ being the stem diameter and $\nu$ representing the kinematic viscosity (Liu and Nepf, 2016). In the study by

Tanino and Nepf (2008b), the vegetation-generated turbulence in a stem array was derived by assuming that the integral length scale $l_t$, which is the characteristic length of turbulent eddies, scales with the stem diameter (Nepf, 1999). However, this assumption may not hold true in the presence of leafy flexible plants. Xu and Nepf (2020) extended the right-most term of Equation 4.5 to account for vegetation with more complex morphology. Considering channel-averaged parameters, the modified equation for vegetation-generated turbulence is given by:

$$\langle k_t \rangle_z = \gamma^2 \left( C_D \frac{\langle a \rangle_z \langle l_t \rangle_z}{2(1 - \langle \phi \rangle_z)} \right)^{2/3} U^2 \tag{4.6}$$

where $\langle \rangle_z$ refers to depth-averaged values of double-averaged parameters.

As a result, an adjustment to Equation 4.5 is necessary, taking into account the integration of Equation 4.6. In the presence of mobile ripples, Yang and Nepf (2019) observed that $k_{t,v}$ dominates over $k_{t,b}$ when $\phi > 0.01$. They emphasized that larger bedforms, such as dunes, can generate additional turbulence that should not be neglected. In this chapter, Equations 4.5 and 4.3 are applied in the presence of leafy flexible vegetation and dunes, in both mobile and fixed-bed conditions. This analysis would enhance the understanding of the intricate interactions among vegetation, dunes and flow dynamics, shedding light on the predictive potential of the proposed models.

## 4.4 Materials and Methods

Experiments were conducted under both mobile-bed (MB) and fixed-bed (FB) conditions. Concerning the mobile-bed conditions, data collected during the experiments described in Chapter 3 were considered, while the FB experiments are described in Section 4.4.1.

In this study, the FB and MB experiments are interconnected in terms of experimental conditions and plant setups. The same artificial flexible plants were used throughout both types of experiments. Moreover, sands with similar characteristics, as described in Table 4.1, were employed in all the experiments. In the FB experiments, the sand was glued onto the surface of the physical 3D-printed model, which served as dune bed.

Table 4.1: Characteristics of the sands used in both MB and FB experiments. $\Upsilon$ is the uniformity coefficient, $D_g$ is the geometric mean size and $\sigma_s$ is the geometric standard deviation.

| **Characteristic diameter** | MB ($mm$) | FB ($mm$) |
|---|---|---|
| $D_{10}$ | 0.639 | 0.631 |
| $D_{16}$ | 0.670 | 0.708 |
| $D_{30}$ | 0.741 | 0.749 |
| $D_{50}$ | 0.843 | 0.806 |
| $D_{60}$ | 0.894 | 0.835 |
| $D_{65}$ | 0.920 | 0.851 |
| $D_{84}$ | 1.172 | 0.965 |
| $D_{90}$ | 1.487 | 1.148 |
| $D_{max}$ | 3.15 | 1.40 |
| $D_{mean}$ | 0.92 | 0.83 |
| $\Upsilon = \frac{D_{60}}{D_{10}}$ | 1.40 | 1.32 |
| $D_g = \frac{1}{2}(\frac{D_{84}}{D_{50}} + \frac{D_{50}}{D_{16}})$ | 1.32 | 1.17 |
| $\sigma_s = (\frac{D_{84}}{D_16})^{0.5}$ | 1.32 | 1.17 |

A fixed plant density of $m = 25$ plants/$m^2$ was maintained in all the experiments. All the experiments were conducted under spatially average uniform flow conditions, in which the plants were just submerged. Experiments in absence of plants were characterized by the same water depth of the vegetated setup.

As previously mentioned, the fixed topography used in the FB experiments was constructed through SfM technique based on photos taken at the end of MB experiments. At the conclusion of each experimental run, a series of photographs at different angulation were taken along a designated section of the flume (Morgan et al., 2017). The length of the section was at least 3 meters for each setup. The photos were processed in Photoscan to generate a point cloud, and then in CloudCompare to accurately remove the plants and flume walls. In areas where leaves obstructed the view, missing parts of the DEM were filled by linear interpolation using surrounding data. An example of a post processed DEM is shown in Figure 4.1. From the generated DEMs, one topography was selected for 3D printing, specifically the one obtained from the 12•4 experiment. The choice was based on the quality of the resulting DEM, as in this particular

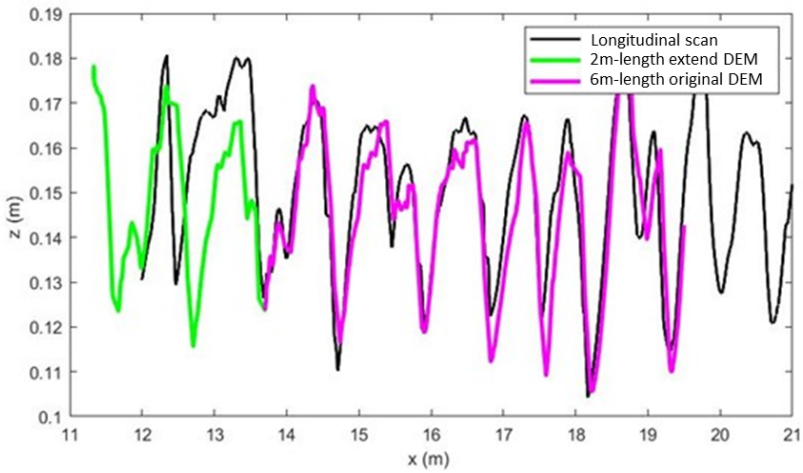


Figure 4.1: Comparison between scan and Photoscan model bed elevation profiles at y=30 cm. The green line corresponds to the extended section of the model.

configuration it was feasible to remove the plants before taking photos at the end of the experiments, thereby preventing any interference from leaves on the topography.

The validation of the resulting DEM involved a comprehensive comparison of bed profiles and dune characteristics. Bed profile scans were conducted along three longitudinal lines located at distances of 15 cm, 30 cm, and 45 cm from the y-axis origin (hydraulic left-hand side of the flume), and at the time of capturing the photos. The comparison between the model-generated topography and the scanned bed profiles is depicted in Figure 4.1, illustrating the close correspondence between the DEM and the original topography. Additionally, the maximum percentage error between the dune characteristics obtained from the scans and presented in Chapter 3 and from the DEM was found to be less than 12%, indicating a general agreement between the model-generated topography and the actual bed morphology (Table 4.2).

Table 4.2: Validation of the DEM by comparing the average dune characteristics. $e$ is the percentage error between the dune characteristics obtained from the scans and from the DEM.

| | height | | | wavelength | | |
|---|---|---|---|---|---|---|
| | DEM (m) | $\Delta_\sigma$ (m) | $e$ (%) | DEM (m) | $\lambda_{crest}$ (m) | $e$ (%) |
| 15 cm | 0.0463 | 0.0435 | 6 | 0.6876 | 0.711 | -3 |
| 30 cm | 0.0383 | 0.038 | 1 | 0.656 | 0.6319 | 4 |
| 45 cm | 0.0482 | 0.0424 | 12 | 0.7977 | 0.7121 | 11 |

### 4.4.1 Fixed-bed Experimental Setups

The FB experiments were conducted in a 10-m long, 0.43-m wide and 0.45-m deep tilting flume of the Fluvial, lagoon and biofluid hydraulics laboratory of the University of Florence. The fixed dunes model was 3D printed in expanded polystyrene and solidly installed at the bottom of the flume (Figure 4.2). The original DEM had a length of 6.05 m and an additional 2-meters section upstream was included to ensure complete development of flow conditions at the measurement section. The extension corresponds to the initial 2 meters of the original DEM, which were replicated at the upstream section of the model. The surface of the 3D printed dunes was then covered with sand to provide bed roughness comparable to that of the MB experiments. To maintain consistency in bed roughness, the remaining 2 meters of the flume were covered with filling material, specifically stones, which provided similar roughness characteristics (Figure 4.3).

Three specific plant stages were chosen from the MB experiments based on their suitability for replicating similar hydraulic conditions, particularly in relation to the Froude number, in the different flume setup. In addition to these plant stages, five experiments were conducted without any vegetation installed. These experiments served as reference conditions for the subsequent analyses.

During the experiments, the water surface was measured at 5 different sections along the flume using eight UNAM 12U9912/S14 ultrasonic sensors with an accuracy 0.5 mm (Figure 4.3). These measurements enabled the determination of the average water depth. The flow conditions

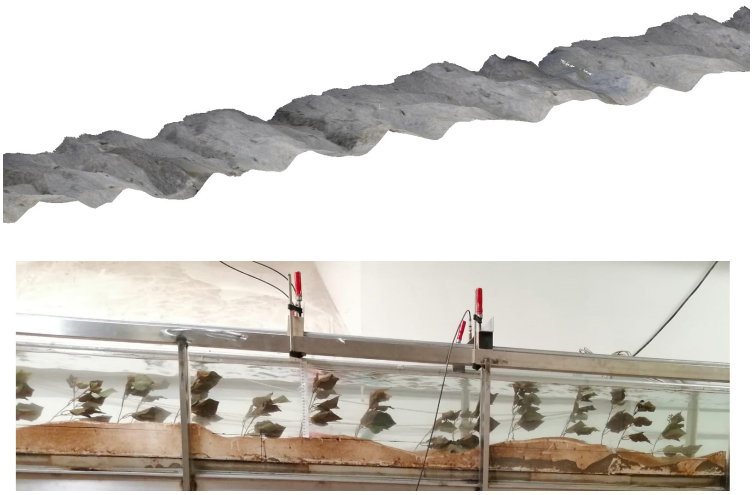

Figure 4.2: On the top, the DEM relative to the 12•4 setup. On the bottom, the corresponding fixed dunes model installed in the flume of the University of Florence.

were adjusted using a weir located at the end of the flume to achieve quasi-uniform conditions.

### 4.4.2 Velocity Measurements

During both experimental activities, flow velocity measurements were conducted using an Acoustic Doppler Velocimeter (ADV) at multiple locations along the flume.

To properly characterize the flow and turbulent fields, especially over a mobile bed, it is essential to have an adequate measurement duration and sampling rate (Yager and Schmeeckle, 2013; Park and Hwang, 2021). High sampling rates are necessary to capture turbulence fluctuations at high frequencies without losing information (Yang and Nepf, 2019). Park and Hwang (2021) suggested that a sampling period of 200 times the characteristic time scale is sufficient for achieving steady conditions in hydraulic parameters.

In the MB experiments, flow velocity measurements were conducted at the morphological equilibrium (defined in Section 3.2.5). The velocity

components were measured using a Nortek Vectrino Profiler ADV with a sampling rate of 100 Hz for a duration of 3 minutes. Point measurements were taken along the velocity profiles with a vertical spacing of 1 cm.

The decision to measure velocity for a duration of three minutes was based on a compromise between the spatial and temporal variability of the measurements. It was necessary to spatially cover a certain number of wavelengths in order to apply the double averaging method, while also ensuring that the measurement time was long enough to capture the flow structure. In these experiments, the turbulent kinetic energy ($k_t$) and mean flow velocity ($u$) did not always stabilize at a constant value within the measurement time. This variability can be attributed to the presence of the mobile bed and its influence on the flow dynamics, even if the conditions outlined in Park and Hwang (2021) were respected. To assess the stabilization period of downstream velocity and turbulent kinetic energy during the MB experiments, long-term measurements were conducted at multiple locations. Running averages of these parameters were analyzed to determine their convergence period and to evaluate the impact of mobile dunes on these measurements. This analysis is discussed in detail in Section 4.4.4.

In the FB experiments, flow velocity measurements were taken after setting up the flume and waiting for 15 minutes to ensure that the flow had reached a fully developed state. The velocity components were recorded using a Nortek Vectrino Plus ADV at a sampling rate of 100 Hz. The duration of the measurement period ranged from 3 to 6 minutes, depending on the data quality, in order to obtain a sufficient number of good quality data samples. Similarly to the MB experiments, the velocity profiles were measured point-to-point with a vertical spacing of 1 cm.

In fixed-bed conditions, the influence of migrating dunes on the measurements was absent, and the cumulative mean of the measurements reached a stable value within the measurement period.

Due to the changing configuration of bedforms along the flume, the number of points in the profiles varied according to the local bed topography. The results were referenced to the mean bed level of the run estimated through the bed elevation scans. It is important to note that the mea-

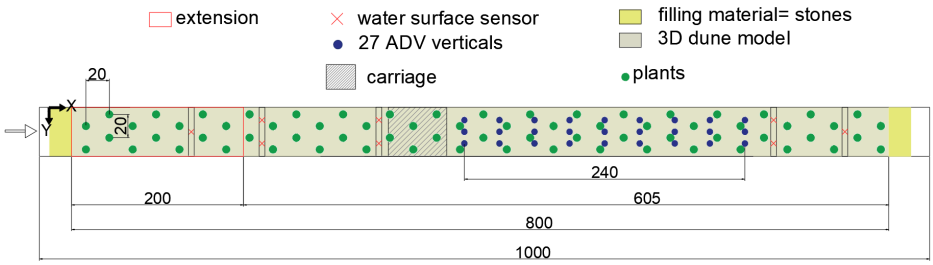


Figure 4.3: Flume setup for FB experiments and locations of velocity measurements verticals. Flow direction is from left to right.

surement volume was located 5 cm below the ADV probe, which made it not possible to measure the first 5 cm below the water surface elevation. To estimate the depth-average velocity, it was assumed that all velocity profiles within the first 5 cm were constant (Maza et al., 2017; Xu and Nepf, 2020).

The ADVs were mounted on moving carriages, ensuring that the probe was oriented perpendicular to the stream direction. A total of 27 vertical profiles were measured along the flume within the vegetation, when present, in both MB and FB experiments.

In the MB experiments, the locations of the vertical profiles were randomly chosen (blue rectangle in Figure 4.5). This random selection pattern was consistently applied in each run of the experimental activity. In contrast, for the FB experiments, a regular grid was used to determine the locations of the vertical profiles, with a longitudinal spacing of 30 cm, (Figure 4.3). This approach provided a fixed reference for the dunes model and the vegetation.

The lengths of the measurement sections were carefully determined to correctly apply the double averaging method. According to Nikora et al. (2007b), in 2D experimental activities with identical fixed dunes, double averaging over a single wavelength is sufficient to characterize the flow. However, for flows over a 3D natural dune field, double averaging requires including multiple bedforms to account for the variability of the flow field. In the present study, the measurement section for the FB experiments was 2.4 m long, corresponding to approximately 4 wavelengths. For the

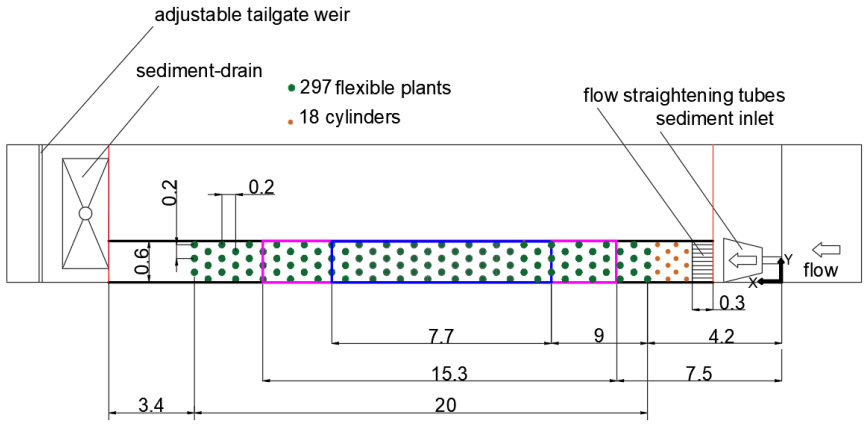


Figure 4.4: Schematic plan view of the flume. Flow direction right to left. The figure is not drawn to scale. Pink rectangle represent the scans section, while the blue one represents the velocity measurement section.

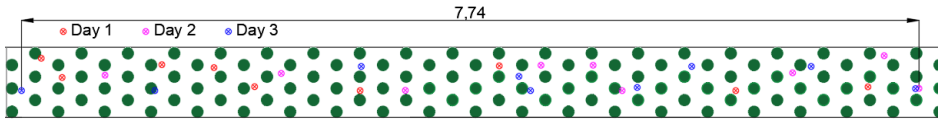


Figure 4.5: Location of velocity measurements verticals taken during each run of MB experiments. The measurement activity was divided into three days for each run. The flow is from right to left.

MB experiments, the measurement section was 7.7 m long, encompassing a varying number of dunes ranging between 6 and 13, depending on the average wavelength associated to the specific run. During the MB experiments, that were the first experiments conducted in chronological order, the cumulative mean of the depth-averaged velocity was used to evaluate the minimum number of profiles needed to converge to the double-averaged velocity. As result, the deviation between the cumulative mean and the depth-averaged velocity drastically reduces to 2% with 15 profiles, while the number of profiles to obtain a minimum deviation (around 1%) is equal to 25 (Figure 4.6). The choice of 27 verticals was decided according to the temporal program of the experiments and kept also for the FB

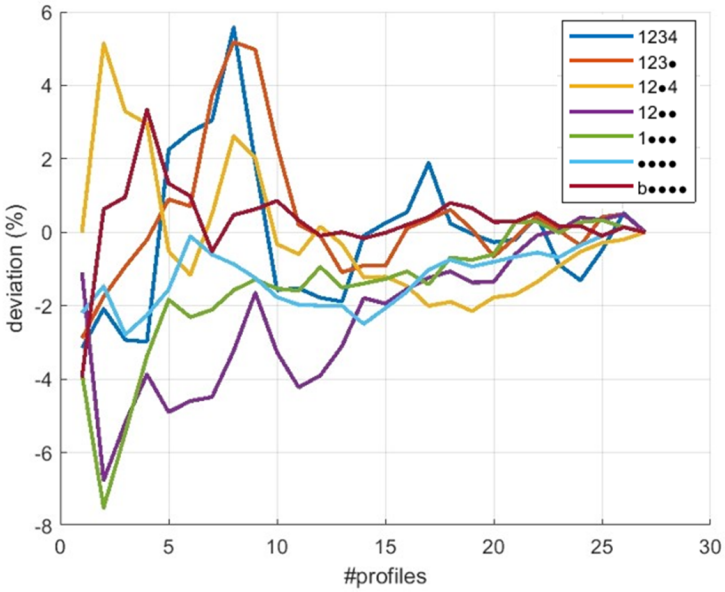


Figure 4.6: Cumulative mean of the depth averaged velocity obtained from MB measurements.

experiments.

### Post-processing of Velocity Measurements

The velocity measurements collected with an ADV require careful data processing to ensure data quality. Unprocessed data can lead to erroneous time-average velocity and turbulent estimates (Wahl, 2000). Many researchers have reported encountering high levels of noise and spikes in their measurements, prompting the development of methods to improve data quality (Hejazi et al., 2016; McLelland and Nicholas, 2000; Nikora and Goring, 1998; Voulgaris and Trowbridge, 1998; Chanson et al., 2008). These methods are designed to minimize noise and remove spikes from the data, ensuring accurate and reliable data analysis.

In this study, a four-phase procedure was employed, which included (1) an initial cleaning of the signal, (2) filtering based on correlation and signal-to-noise ratio values, (3) despiking, and (4) denoising. The first step

aims to remove outliers due to the overranging of the ADV probes (Wahl, 2000). The ADV measures flow velocity based on the phase change in the signal reflected by scattering particles in the water. When the flow velocity exceeds the measurement range set by the user, the ADV may exhibit velocity ambiguities, resulting in spikes. This phenomenon is known as aliasing (Wahl, 2000). Additionally, spikes can occur when measurements are contaminated by the reflection of previous pulses on complex boundaries (Goring and Nikora, 2002; Nortek, 2018). The procedure proposed by Hanmaiahgari and Balachandar (2016) was employed to identify and remove outliers in the velocity measurements. Outliers were defined as data points that exceeded 3.5 times the standard deviation of the velocity time series.

In the second phase of the data processing procedure, the focus was on filtering out data with low signal-to-noise ratio ($SNR$) and correlation $Corr$ values to ensure high-quality data. $Corr$ reflects the consistency between the two pulse echoes measured within the sampling period. Using a Matlab routine, the signals recorded by the four beams were filtered to exclude data points with $SNR < 15$ dB and $Corr < 70\%$, which thresholds are commonly used in post-processing ADV velocity measurements in turbulent flow (Wahl, 2000; McLelland and Nicholas, 2000; Nortek, 2018).

Furthermore, it is important to note that spikes in the data cannot be easily categorized as either too high or too low outliers. These spikes can sometimes resemble natural fluctuations, leading to potential confusion in their interpretation (Goring and Nikora, 2002). For this reason, an additional despiking tool (third step) was applied. The iterative method developed by Goring and Nikora (2002) was considered, which is suitable also for spikes due to the background reflection.

After the initial three steps of the post-processing procedure, the data that has been removed appears as gaps within the measurements. Many methods have been developed to address gaps in velocity time series data, offering various approaches such as spline fitting (Goring and Nikora, 2002) and simple replacement using median values (Doroudian et al., 2010). Lai and Socolofsky (2018) proposed the utilization of a linear AR model when the mean duration of data gaps exceeds the time integral scale $t_t$ (reported in Section 4.4.3). Linear autoregressive (AR) models belong to the family

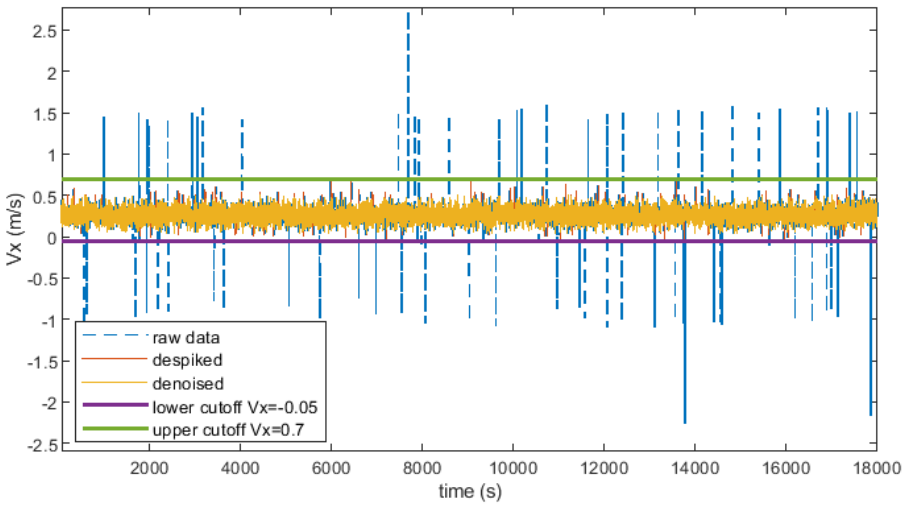


Figure 4.7: Velocity data analysis: post-processed time series by means of cutoff filter, despiking and denoising tools. The horizontal lines corresponds to the cutoff thresholds.

of linear autoregressive-moving-average (ARMA) models (Shumway et al., 2000). However, unlike the full ARMA models, linear AR models do not include the moving-average component. In an AR model, the output variable is linearly dependent on its own previous values and a stochastic term related to the autocorrelation function (Lai and Socolofsky, 2018; Faranda et al., 2014). Considering both the FB and MB experimental data, it was observed that the average maximum duration of data gaps was found to be between 4 and 10 times larger than $t_t$. Consequently, following the recommendation of Lai and Socolofsky (2018), the data removed during the initial three phases were filled using an first-order AR model (AR(1)). It is worth noting that the proposed method has been validated by the authors up to a 20% data gap, while acknowledging that a 50% data gap can lead to increased energy levels at low frequencies. The occurrence of data gaps in the measurements was found to be random over time, as no discernible pattern was identified when examining the autocorrelation of the time gap sequence. The assessment of discarded percentages was conducted after the completion of phases 2 and 3, as documented in Table

4.5. Generally, the majority of discarded data points were associated with phase 2, wherein filtering was applied based on the two thresholds, i.e., $SNR < 15dB$ and $Corr < 70\%$. As a result, FB experiments with the 123• and 12•4 setups exhibited significantly higher discarded percentages, over 50%. For these setups, nominal velocity ranges were set at 0.3 m/s or 1 m/s, resulting in corresponding vertical velocity ranges of 0.27 m/s or 0.54 m/s, and horizontal velocity ranges of 0.94 m/s or 1.88 m/s. Nortek (2018) suggests that velocity fluctuations can be expressed as a percentage of the mean flow velocity, and thus, it was assumed that the actual velocity fluctuations fell within these prescribed limits. Furthermore, the differing number of spikes observed in the four beams led to the assessment that the outliers in the velocity series are predominantly associated with interference from the boundary rather than being a result of aliasing (Doroudian et al., 2010). Thus, a cutoff filter was implemented to remove outliers from measurements (Wahl, 2000). Consequently, a higher percentage of data was discarded, as indicated in Table 4.5. The maximum discarded percentage was 60% resulted for 12•4. In order to mitigate the substantial data loss, the sampling period was extended to ensure the acquisition of at least 9000 "good" samples. While it is commonly acknowledged that low correlation is prevalent in highly turbulent flow, some studies argue against discarding data solely based on low signal correlations, particularly in the case of four-armed ADV (Martin et al., 2002; Wahl, 2000). Martin et al. (2002) recommended repeating the filtering step if the retained data falls below 70% reducing correlation threshold from 70% to 40%. In the present case, the velocity post-processing procedure was repeated for FB experiments 123• and 12•4 setups with a correlation threshold of 40% accordingly with Martin et al. (2002), resulting in lower discarded percentages of 26.7 and 29.3 %, respectively. The need for this modification may be attributed to a structural change in the water recirculation system of the laboratory during the experiment program.

The final step involves removing Doppler noise, which is a significant source of error in ADV measurements that results in signal decorrelation (Voulgaris and Trowbridge, 1998). Doppler noise is a Gaussian white noise that affects turbulence parameters but does not impact the mean velocity value (Nikora and Goring, 1998). A publicly accessible tool developed by

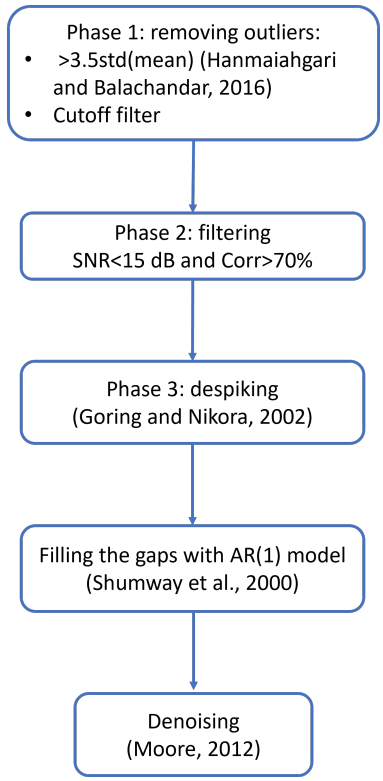


Figure 4.8: Post-processing procedure of the velocity measurements.

Moore (2012) was utilized for denoising. The tool is based on the denoising filter proposed by Kalman et al. (1960) and the filter parameters were set according to the recommendations provided by Huang et al. (2020).

### 4.4.3 Data Analysis

After post-processing the velocity data, the turbulent velocity spectra were computed to estimate the integral length scale $l_t$. The estimation of the $l_t$ was performed by analyzing the time series of turbulent fluctuations in the streamwise direction $u'$. This estimation procedure involved the identification of the frequency peak, $f_{peak,u'}$, within the frequency-weighted power spectrum density of $u'(t)$ (Figure 4.9). In order to obtain the spatial representation, Taylor's frozen turbulence hypothesis was ap-

plied to transform the temporal spectra into the spatial domain (Tanino and Nepf, 2008b; Xu and Nepf, 2020; Huang et al., 2020):

$$l_t = \frac{\overline{u}}{2\pi f_{peak,u'}} \tag{4.7}$$

where $\overline{u}$ is the time-averaged velocity at a specific height above the reference bed. The power spectral densities were determined using the Welch method with 50% overlap, using *pwelch* Matlab function (Tanino and Nepf, 2008b). Spectra that did not exhibit a clear peak were excluded from the estimation of the integral length scale (Figure 4.9). During the double-averaging procedure, $l_t$ values that deviated more than three standard deviation from the spatially averaged value $\langle l_t \rangle$ were discarded.

Finally, all the estimated quantities, including $\overline{u}$, $l_t$, and $k_t$, were double-averaged in both the time and space domains. During the spatial-averaging procedure, it is important to note that the near-bed results may be influenced by a limited number of measured points. In this particular study, a careful selection of data points was performed, considering only those points for which a minimum of 10 measurements were available along the averaging volume at the same z coordinate. The presented results pertain to the double-averaged quantities (Section 4.5).

To utilize the predictive formulation for turbulent kinetic energy ($k_t$) proposed by Xu and Nepf (2020) (Eq. 4.6), it is necessary to determine the drag coefficient ($C_D$) for each foliage configuration (reported in Table 4.6). For the MB experiments, the drag coefficient is obtained by referring to Figure 4b in Aberle et al. (2011), which provides $C_D$ values for the corresponding plant foliage configurations as a function of flow velocity. b●●●● and ●●●● setups were not considered in the work of Aberle et al. (2011). Therefore, for the b●●●● setup, considering the complex morphology structure of the plant, a value of $C_D = 1$ is chosen, as it is commonly used in vegetation studies (Vargas-Luna et al., 2015; Aberle and Järvelä, 2013). While, for the ●●●● setup, the drag coefficient is determined using the equation proposed by Chapman et al. (2015), which is validated for flexible and rigid cylinders:

$$C_D = -0.648 Ln(Re) + 6.212 \tag{4.8}$$

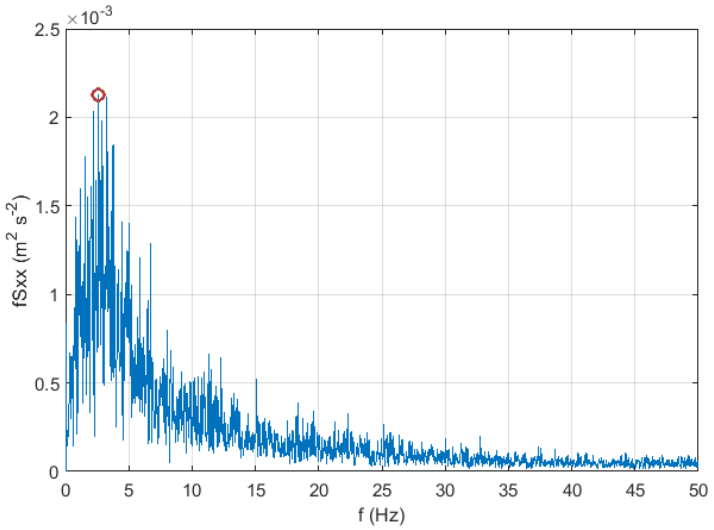


Figure 4.9: Peak of the frequency-weighted turbulence spectrum fSxx (labeled with a red circle), considered to estimate the integral length scale $l_t$ (using Equation 4.7).

where $Re = Ud_e/\nu$ is the Reynolds number calculated using the vegetation obstruction width that coincides with the equivalent diameter $d_e$, resulting in a value of $C_D = 1.20$. The same drag coefficients ($C_D$) derived from the MB experiments are used for the FB experiments, given the nearly identical channel-averaged velocity among the vegetated cases.

### 4.4.4 Impact of Mobile Bedforms on Measurements

To assess the impact of dune evolution on the flow field, it is common to conduct measurements that cover a time duration longer than the period of one dune wavelength (Delecluyse et al., 2010). In this study, simultaneous measurements of flow velocity and bed elevation were conducted within the vegetation at a specific elevation above the mean bed level. The measurements were carried out during 1234 vegetation runs, with record duration ranging from 15 minutes to 1 hour. These durations exceed the average dune migration period, which was 12 minutes.

To analyze the temporal behavior of flow velocity, running averages of

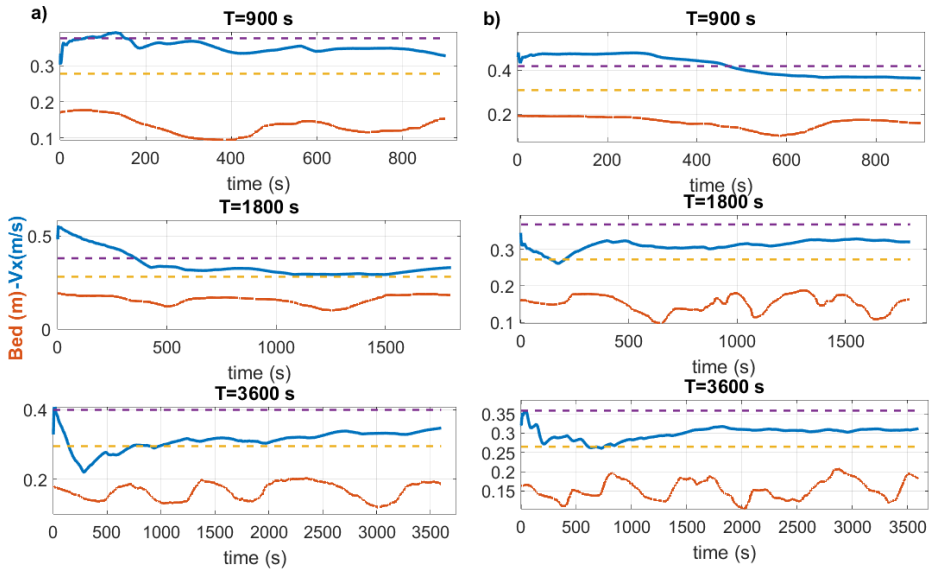


Figure 4.10: Running averages (blue line) of different duration $T$ of streamwise flow velocity at a distance of: a) 21 cm and b) 26 cm from the flume bottom. The measurement duration $T$ is indicated above each graph. The red line is the bed evolution. The horizontal dashed lines represent $\pm 15\%$ deviation.

the streamwise flow velocity were calculated (Figure 4.10). Among the six velocity samples analyzed, three samples exhibited a convergence within $\pm 15\%$ deviation after three minutes. The remaining velocity measurements achieved convergence within 16 minutes, a duration that appears to scale with the average dune period of 12 minutes.

To estimate the impact of migrating dunes on the flow field, 3-minutes velocity samples were extracted from the longest-time measurements and mean streamwise flow velocity values were estimated for each sample (Yang and Nepf, 2019). Figure 4.11 illustrates the comparison between these estimates and the overall mean value (indicated by the solid horizontal line). The standard deviation of the 3-minute flow velocity, denoted by dashed lines, was found to be 20% and 28% of the mean value for measurements taken at 26 cm and 21 cm from the flume bottom, respectively. This observation suggests that a value of 30% of the mean value, which approximately corresponds to the maximum observed standard deviation,

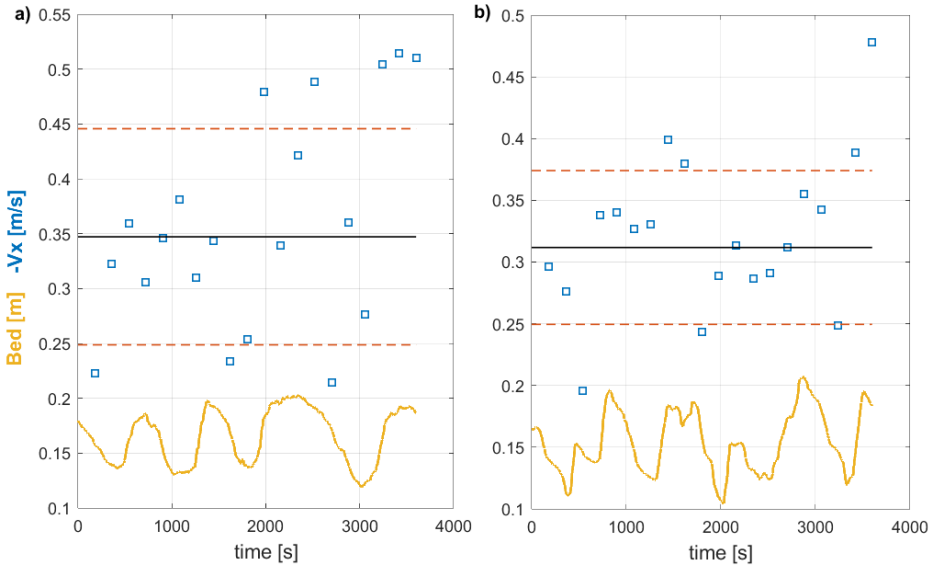


Figure 4.11: Three-minute averaged flow velocity (blue squares) measured over migrating dunes. Measurements taken at a distance of: a) 21 cm and b) 26 cm from the flume bottom. The yellow line represents the bed evolution, while the horizontal black line the overall mean. The standard deviation is shown as dashed lines.

can be considered representative for the experimental results presented in this study.

Similarly, 3-minutes samples of turbulent kinetic energy ($k_t$) were time-averaged and compared with the overall mean value (Figure 4.12). The standard deviation of the three-minute $k_t$ averages was significantly lower compared to those resulted for the streamwise velocity. Specifically, at a distance of 26 cm from the flume bottom, the standard deviation accounted for 7% of the mean value. Moreover, at a closer distance of 21 cm from the flume bottom, the standard deviation was even lower, representing only 3% of the mean value. The values obtained in this study indicate significantly lower standard deviations compared to those reported by Yang and Nepf (2019), who found a maximum standard deviation of 21% for $k_t$ over migrating ripples. Furthermore, the analysis revealed an in-phase trend between the 3-minute averaged $k_t$ and the bed evolution, with $k_t$

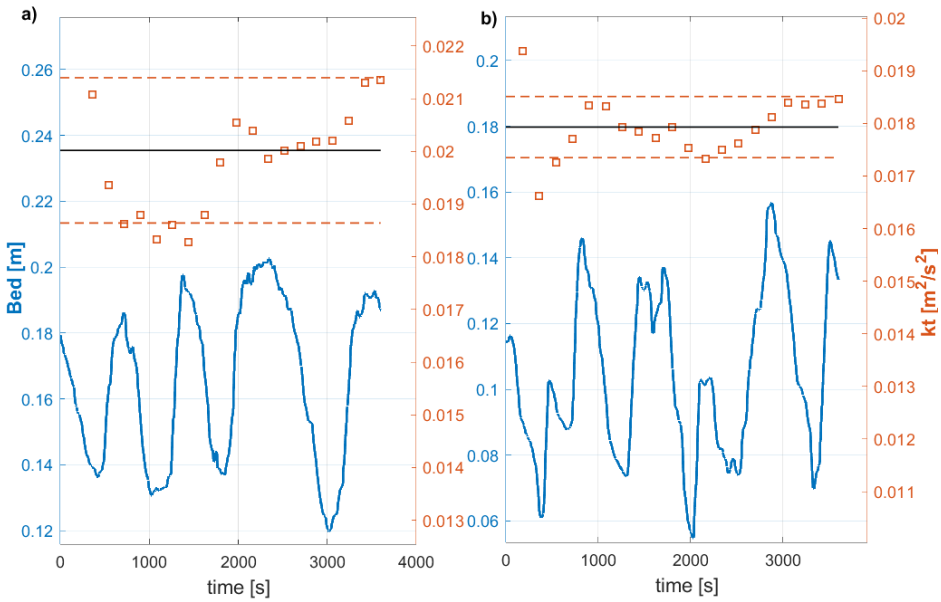


Figure 4.12: Three-minute averaged $k_t$ (orange squares) measured over migrating dunes. Measurements taken at a distance of: a) 21 cm and b) 26 cm from the flume bottom. The blue line represents the bed evolution, while the horizontal black line the overall mean. The standard deviation is shown as dashed lines.

appearing to increase over the stoss side of the bedforms. Additionally, when examining the cumulative means of $k_t$ over time, it was observed that five out of the six recorded time series converged within ±15% of the time-averaged $k_t$ (Figure 4.13).

Direct investigation of the influence of larger dunes on the flow field was not possible due to the unavailability of long-time measurements for setups characterized by lower LAI. However, it can be assumed that the influence of larger dunes was better captured in the recorded data, given their higher migration rate.

In previous studies, turbulent flow over migrating dunes and ripples was characterized using different sampling periods. For instance, Krick and Sukhodolov (2014) conducted measurements over river dunes for sampling periods that ranged from 17% to 30% of the migration period. Sim-

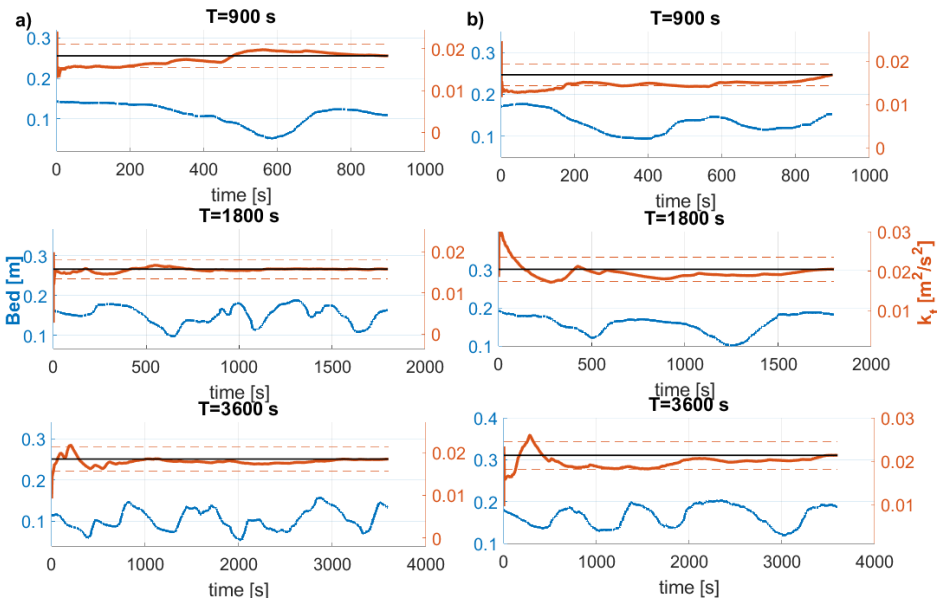


Figure 4.13: Running averages (orange line) of different duration of $k_t$ at a distance of: a) 21 cm and b) 26 cm from the flume bottom. The horizontal dashed lines represent ±15% deviation. The blue line represents the bed evolution.

ilarly, Yang and Nepf (2018) performed turbulence measurements over migrating ripples with sampling periods varying from 4% to 90% of the migration period. In the measurements, the sampling period corresponded to $24 \div 63\%$ of the dune migration period (Table 4.3).

Among the different setups considered, the 1234 configuration exhibited one of the longest average dune periods $T_{dune}$, which were associated with denser vegetation. As the frontal area of the vegetation decreased, the dune celerity increased, resulting in shorter dune periods. For the bare stem scenario, the dune period was as short as 5 minutes. It is important to recall that the setups were characterized by a gradual increase in flow discharge values from run to run, starting with the fully foliated setup 1234 and concluding with the bare bed scenario.

Table 4.3: Average dune migrating period $T_{dune}$ and the ratio between $T_{dune}$ and sampling period (that is equal to 3 min). $T_{dune}$ is estimated as the ratio of the average dune wavelength and the observed celerity.

| Setup | $T_{dune}$ (min) | $T_{dune}$/sampling period |
|---|---|---|
| 1234 | 12 | 24% |
| 123• | 14 | 21% |
| 12• 4 | 14 | 22% |
| 12•• | 13 | 23% |
| 1••• | 10 | 30% |
| b•••• | 7 | 44% |
| •••• | 5 | 63% |

## 4.5 Results

The applied hydraulic conditions for the FB experiments are provided in Table 4.4. The five experiments conducted under bare bed conditions, referred to as "BB," involved flume sloped values from 0.09 to 0.22%, aiming to explore a broader range of hydraulic conditions. The first three of them were characterized by similar conditions of the vegetated setup, with similar Froude number and water depth. In BB 4 and 5 setups, the Froude numbers were slightly higher to achieve a better match between the bed slope and the water surface slope.

However, it should be noted that in some setups of the FB experiments, there was a discrepancy between the water surface slope and the flume slope. This mismatch is attributed to the limited length of the channel and constraints in adjusting the water height, as all experiments were conducted under similar water depths, which corresponds to submerged conditions for the plants.

The resulting averaged signal-to-noise ratio ($SNR$) and correlation coefficient ($Corr$) exceeded the specified thresholds. For FB experiments, the $SNR$ of the post-processed data resulted higher than 22 dB and $Corr > 88\%$, while for MB experiments, they were $SNR > 33$ dB and $Corr > 92\%$. These values ensure the reliability of the measurements (Table 4.5).

The effectiveness of the denoising procedure was demonstrated by the

Table 4.4: Hydraulic conditions applied for the FB experiments. $U$ is the channel averaged velocity as $U = Q/(WH)$. The averaged uncertainty of the energy slope $S_E$ is equal to $\pm 0.07\%$, estimated as 95% confidence intervals.

| Setup | Q (l/s) | H (m) | U (m/s) | $Fr$ (-) | $S_b$ (%) | $S_E$ (%) |
|---|---|---|---|---|---|---|
| 1234 | 36.4 | 0.234 | 0.36 | 0.24 | 0.80 | 0.74 |
| 123• | 36.4 | 0.231 | 0.37 | 0.24 | 0.80 | 0.56 |
| 12•4 | 36.5 | 0.232 | 0.37 | 0.24 | 0.80 | 0.60 |
| BB 1 | 30.0 | 0.206 | 0.34 | 0.24 | 0.09 | 0.20 |
| BB 2 | 30.0 | 0.194 | 0.36 | 0.26 | 0.12 | 0.23 |
| BB 3 | 29.9 | 0.200 | 0.35 | 0.25 | 0.13 | 0.22 |
| BB 4 | 30.0 | 0.179 | 0.39 | 0.30 | 0.17 | 0.27 |
| BB 5 | 30.0 | 0.164 | 0.42 | 0.33 | 0.22 | 0.29 |

agreement of the denoised spectra with the expected Kolmogorov's $-5/3$ power law at intermediate frequencies (Pope and Pope, 2000; Lai and Socolofsky, 2018), as shown in Figure 4.14. This figure presents an example where the spectrum of the noisy data displays a flat (horizontal) trend at high frequencies, also documented by Huang et al. (2020).

### 4.5.1 Velocity Profiles

The double-averaged streamwise velocity $\langle \overline{u} \rangle$ and turbulent kinetic energy profiles $\langle \overline{k_t} \rangle$ obtained from MB experiments are reported in Figure 4.15a. In the case of the densest vegetation configurations, specifically 1234, 12•4 and 123•, the vertical velocity distribution exhibits a uniform pattern, mirroring the relatively homogeneous morphology of the plants along the z-direction. This observation suggests a strong correlation between the vegetation density and the flow behavior, even if the flow is over mobile dunes. Conversely, as the LAI decreases, the velocity profiles display an increasingly logarithmic shape, following a turbulent boundary layer profile. These findings are consistent with prior investigations focusing on the dynamics of vegetated flow over a planar fixed bed, as reported by Aberle and Järvelä (2013) and Nepf and Vivoni (2000). Remarkably, the absence of negative velocities in the present measurements

Table 4.5: Average Correlation and SNR for all conducted experiments. Discarded Percentage (DP) of data after phase 2-filtering and 3-despiking. DP is calculated based on the total measured samples. The brackets () indicate the resulted DP obtained prior to repeating the post-processing procedure for the velocity measurements.

| Setup MB | *Corr* | *SNR* | DP 2 | DP 3 | Setup FB | *Corr* | *SNR* | DP 2 | DP 3 |
|---|---|---|---|---|---|---|---|---|---|
| 1234 | 94 | 33 | 2.4 | 3.4 | 1234 | 89 | 24 | 23.6 | 24.5 |
| 123• | 94 | 34 | 3.0 | 4.1 | 123• | 88 | 22 | 25.4 (51.1) | 26.7(51.8) |
| 12•4 | 93 | 33 | 3.4 | 4.3 | 12•4 | 88 | 22 | 27.8 (59.8) | 29.3(60.4) |
| 12•• | 93 | 35 | 5.6 | 6.6 | BB 1 | 93 | 25 | 3.6 | 4.3 |
| 1••• | 93 | 37 | 8.8 | 9.9 | BB 2 | 91 | 25 | 8.2 | 9.2 |
| b•••• | 92 | 36 | 16.4 | 17.3 | BB 3 | 91 | 24 | 10.2 | 11.8 |
| •••• | 92 | 38 | 20.2 | 21.0 | BB 4 | 92 | 25 | 3.7 | 4.3 |
| | | | | | BB 5 | 92 | 25 | 6.2 | 6.9 |

indicates a notable suppression of reverse flow within the recirculation zone, which can be attributed to the presence of vegetation, which contrasts with the reversed velocities typically observed in the recirculation zone of bare fixed 2D dunes (Dey et al., 2020). Consequently, it can be concluded that the configuration of the double-averaged streamwise velocity $\langle\overline{u}\rangle$ is jointly influenced by the vegetation and the presence of dunes, reflecting the intricate interplay between these two factors. According to Nepf (2012), the classification of canopy density as either dense or sparse is based on a vegetation roughness density threshold, i.e., $C_D\langle a\rangle_z h_p \approx 0.1$, where $\langle a\rangle_z = md_e = mA_f/h_p$ is the vegetation frontal area per unit volume, with $d_e$ is the equivalent diameter and $A_f$ the frontal area (see Chapter 3). In this study, 1234, 12•4 and 123• setups can be classified as dense vegetation, as their $C_D\langle a\rangle_z h_p > 0.17$ (Table 4.6). Conversely, setups with lower leaf mass were categorized as sparse vegetation, with $C_D\langle a\rangle_z h_p < 0.1$. Remarkably, the observed $\langle\overline{u}\rangle$ profiles conform to the expected patterns within dense and sparse canopies, as outlined by Nepf (2012). This agreement highlights the applicability of the $C_D\langle a\rangle_z h_p$ classification, even in the presence of leafy and flexible vegetation, as well as mobile dunes. The obtained double-averaged velocity profiles $\langle\overline{u}\rangle(z)$ were integrated throughout the water depth, assuming a constant value within the first five cm below the water surface (Maza et al., 2017; Xu and Nepf, 2020). These depth-averaged velocities, denoted as $\langle\overline{u}\rangle_z$, were then com-

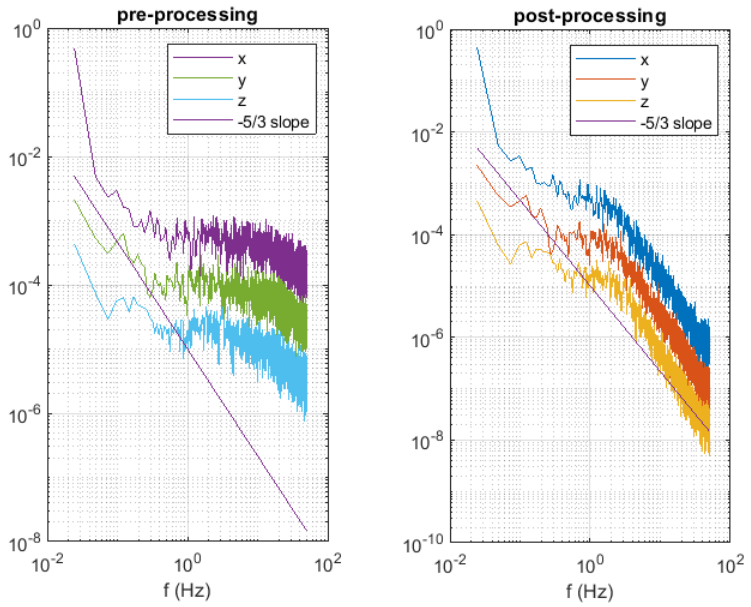


Figure 4.14: Comparison between noisy and denoised spectra. A noticeable distinction is observed in the slope of the spectra, which becomes steeper as the noise is eliminated, converging towards the expected -5/3 slope.

pared to the channel-averaged velocity $U = Q/(WH)$. It was observed that the $\langle\overline{u}\rangle_z$ values were consistently lower than the $U$ values, with the leafiest setup (1234) exhibiting a maximum percentage error of -19%. The magnitude of this deviation increased with the plant roughness density (Table 4.6), indicating a potential sheltering effect (Caroppi et al., 2022). The presence of vegetation in the wake region reduces the flow velocity magnitude, and this effect becomes more pronounced as the plant blockage factor increases. Consequently, the observed deviation in $\langle\overline{u}\rangle_z$ from $U$ is likely associated with measurements obtained within the wake region.

Figure 4.16 presents the double-averaged velocity profiles obtained from FB experiments. Panel (a) displays the velocity profiles from the bare bed conditions, while panel (b) shows the profiles from the vegetated setups. By comparing these two panels, the impact of vegetation on the flow field over the fixed dune bed can be assessed. The velocity pro-

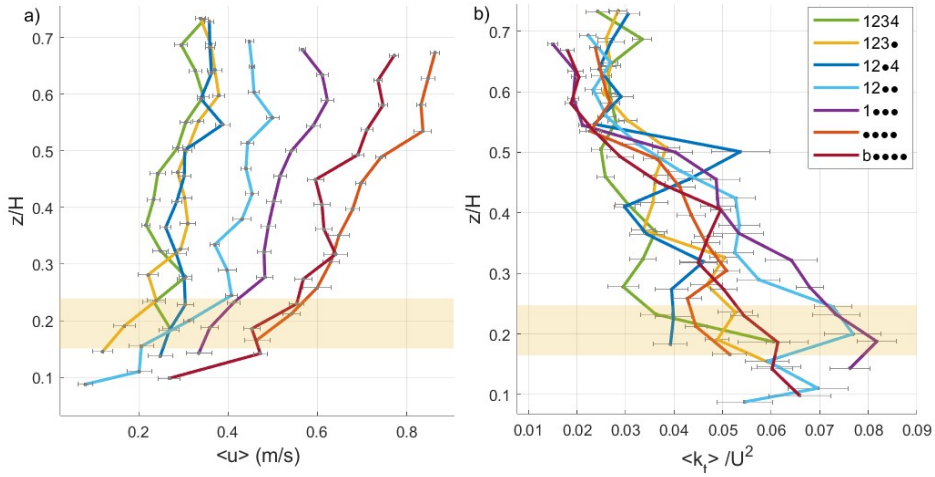


Figure 4.15: Double-averaged a) streamwise velocity $\langle \overline{u} \rangle$ and b) dimensionless turbulent kinetic energy $\langle \overline{k_t} \rangle / U^2$ resulting from MB experiments. Horizontal bars represent the standard deviation related to spatial variability. The highlighted rectangle represents the range of the maximum bed level recorded in the different setups. The mean bed level corresponds to the elevation $z = 0$.

file over bare fixed dunes exhibits a quasi-logarithmic shape, consistent with previous studies investigating hydrodynamics over dunes (McLean and Nikora, 2006; McLean et al., 2008; Nikora et al., 2001). However, in contrast to the mobile bed (MB) experiments, the profiles obtained in the vegetated setups clearly demonstrate the influence of the missing branch. In the densest vegetation setup (1234), the velocity profile remains predominantly vertical along the water depth. In setups 12•4 and 123•, on the other hand, deviations from the vertical can be observed at elevations corresponding to the missing branch. These deviations indicate an acceleration of flow within the gaps between the leaves.

### 4.5.2 Turbulence Field

Figure 4.15b presents the dimensionless turbulent kinetic energy profiles $\langle \overline{k_t} \rangle_z / U^2$ obtained from the MB experiments. The profiles exhibit some similarities, but noteworthy differences can be observed. The 1234 setup is characterized by a nearly vertical profile and the lowest turbulence

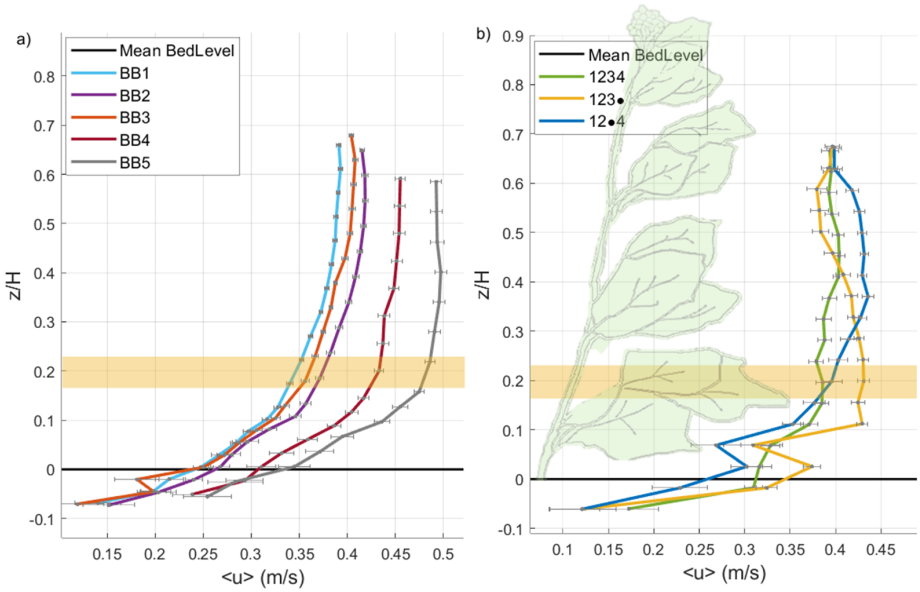


Figure 4.16: Double-averaged streamwise velocity $\langle \overline{u} \rangle$ from FB experiments: a) bare bed setups; b) vegetated setups. Line at z=0 represents the mean bed level. The highlighted rectangle represents the range of the maximum bed level recorded in the different setups. The plant is to scale.

intensity values, while the 1••• and 12•• setups show higher turbulence levels. These setups are characterized by a greater vertical variation in plant LAI and larger average dune height (Table 3.6). Notably, a peak can be observed in the 12•4 profile, which is likely associated with the presence of a leaf gap.

On the other hand, Figure 4.17 presents the dimensionless turbulent kinetic energy profiles $\langle \overline{k_t} \rangle / U^2$ for the FB experiments. The profiles exhibit different shapes. In the bare bed (BB) conditions, the $\langle \overline{k_t} \rangle$ increases as it approaches the bed, displaying a peak below the mean bed level elevation ($z = 0$). This behavior can be attributed to the higher turbulence levels in the separation zone located downstream of the dune crest. Moreover, in the vegetated setups, the $\langle \overline{k_t} \rangle / U^2$ profiles reflect the vertical variation of plant morphology. The 1234 setup exhibits a uniform trend along the vertical direction, while the 123• and 12•4 profiles deviate from unifor-

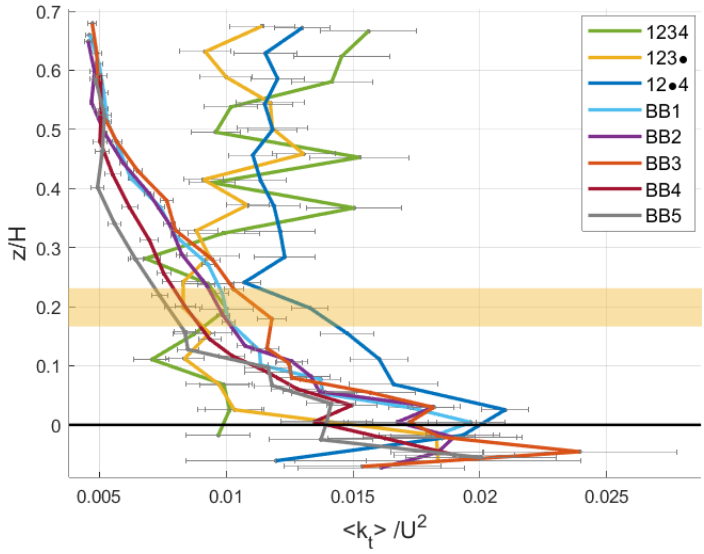


Figure 4.17: Dimensionless double-averaged $\langle \overline{k_t} \rangle / U^2$ resulted from FB experiments, where $U$ is the channel-averaged velocity. Horizontal bars represent the standard deviation related to spatial variability.

mity at elevations corresponding to leaf gaps. This deviation is caused by velocity gradients occurring within the leaves and gaps, promoting the generation of Kelvin-Helmholtz instabilities and consequently enhancing the turbulence budget (Aberle and Järvelä, 2015; Nepf, 2012).

The turbulent kinetic energy fractions associated with the streamwise, spanwise, and vertical fluctuations, $u', v', w'$, are analyzed in both fixed-bed and mobile-bed conditions and reported in Figure 4.18and 4.19, respectively. In the fixed bed conditions (Figure 4.18), the streamwise $0.5\langle \overline{u'} \rangle^2 / k_t$ and the spanwise component (v) of $k_t$ demonstrate similar average magnitudes, indicating an isotropic nature of the turbulence field. This suggests that the turbulent motions are equally prominent in all directions within the horizontal plane. Conversely, the $0.5\langle \overline{w'} \rangle^2 / k_t$ increases with increasing z. This behavior can be attributed to the influence of the bedform geometry and the shear layer associated with flow over dunes. Above the dune crest, $0.5\langle \overline{u'} \rangle^2 / k_t$ exhibits a slight increase, followed by a decrease along z. In contrast, $0.5\langle \overline{v'} \rangle^2 / k_t$ remains relatively constant along

the vertical profile. It is worth noting a subtle distinction between the vegetated and non-vegetated setups in terms of $0.5\langle\overline{u'}\rangle^2/k_t$ and $0.5\langle\overline{v'}\rangle^2/k_t$ components. The vegetated setups display lower magnitudes of $0.5\langle\overline{u'}\rangle^2/k_t$ and higher magnitudes of $0.5\langle\overline{v'}\rangle^2/k_t$ compared to the non-vegetated setups. This can be attributed to the increased complexity of the turbulence field caused by the presence of vegetation.

In the mobile bed conditions (Figure 4.19), the distribution of $k_t$ components demonstrates a markedly different pattern. The $0.5\langle\overline{u'}\rangle^2/k_t$ components dominates over the other components, constituting approximately 80% of the total $k_t$, while the spanwise component and the vertical component contribute to around 10% each, on average. $0.5\langle\overline{u'}\rangle^2/k_t$ initially increases and then decreases along the vertical profile, signifying a transition in the turbulence dynamics. Conversely, both $0.5\langle\overline{v'}\rangle^2/k_t$ and $0.5\langle\overline{w'}\rangle^2/k_t$ components exhibit a decrease followed by an increase along z. These observations suggest a complex interplay between the flow dynamics and the mobile bed conditions. Interestingly, no discernible distinction is observed in the distribution of $k_t$ components among the various experimental setups within the mobile bed framework, implying that the influence of mobile bed dynamics outweighs the specific configuration of the experimental setup.

The observed differences in averaged values and trends in the turbulence profiles between the FB and MB experiments can be attributed to the effects of mobile dunes, taking into account that the FB experiments involved 3D printed dunes representing the final morphology of the MB experiments.

The double-averaged turbulence intensity was estimated as $\sqrt{\langle\overline{k_t}\rangle}_z/U$ (Xu and Nepf, 2020) and is reported in Table 4.6 for the MB experiments and in Table 4.7 for the FB experiments.

In the FB experiments, both vegetated and unvegetated cases showed similar $\sqrt{\langle\overline{k_t}\rangle}_z/U$ values, with a slight increase observed for 12•4 setup. On the other hand, in the MB experiments, there was a noticeable increasing trend in turbulence intensity as the vegetation roughness density decreased. It is important to note that lower LAI values in the experiments led to larger dunes due to higher flow velocities required to achieve the just-submerged conditions.

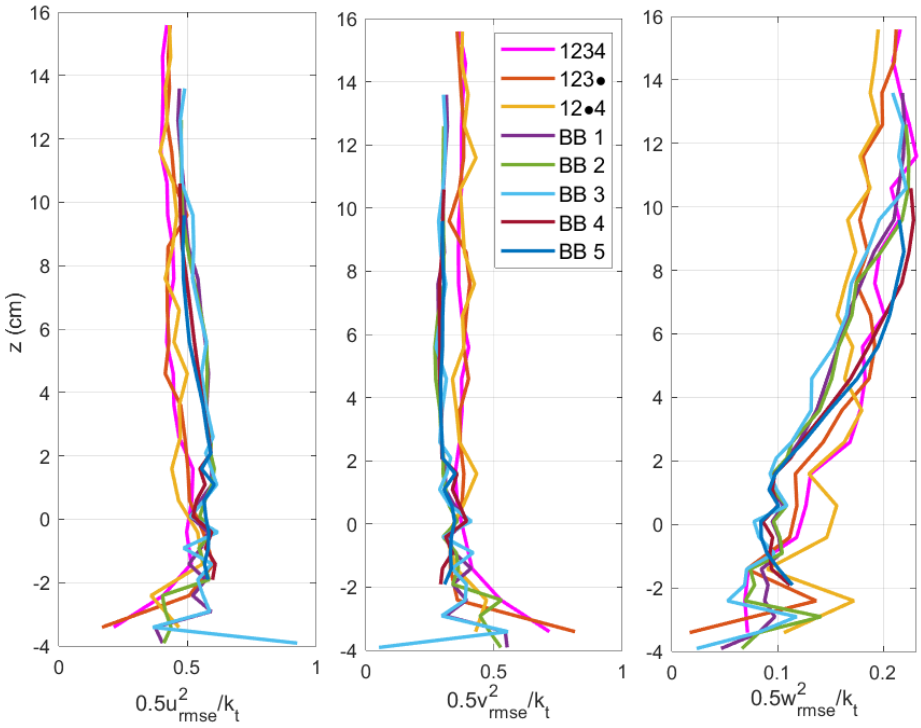


Figure 4.18: Streamwise, spanwise, and vertical fractions of the turbulent kinetic energy for FB experiments.

Comparing the channel-average turbulence intensities $\sqrt{\langle \overline{k_t} \rangle}_z / U$, the MB experiments exhibited turbulence levels that are approximately two to three times higher than those observed in the FB experiments.

To investigate whether the impact of dunes or vegetation dominates the overall turbulence budget, the turbulence intensity was plotted against dimensionless parameters related to the dune geometry (Figure 4.20). An initial analysis revealed a clear increase in turbulence as the dunes grew larger. The turbulence intensity was further modeled using a new variable defined in Equation 4.9, and the fit of the equation to the data yielded the proportional parameters $\alpha = 2.97 \pm 1.179$ and $\beta = 0.1493 \pm 0.018$, with uncertainties estimated as 95% confidence intervals.

$$\frac{\sqrt{\langle k_t \rangle}}{U} = \alpha \left( \frac{\Delta^2}{\lambda H} \right) + \beta \tag{4.9}$$

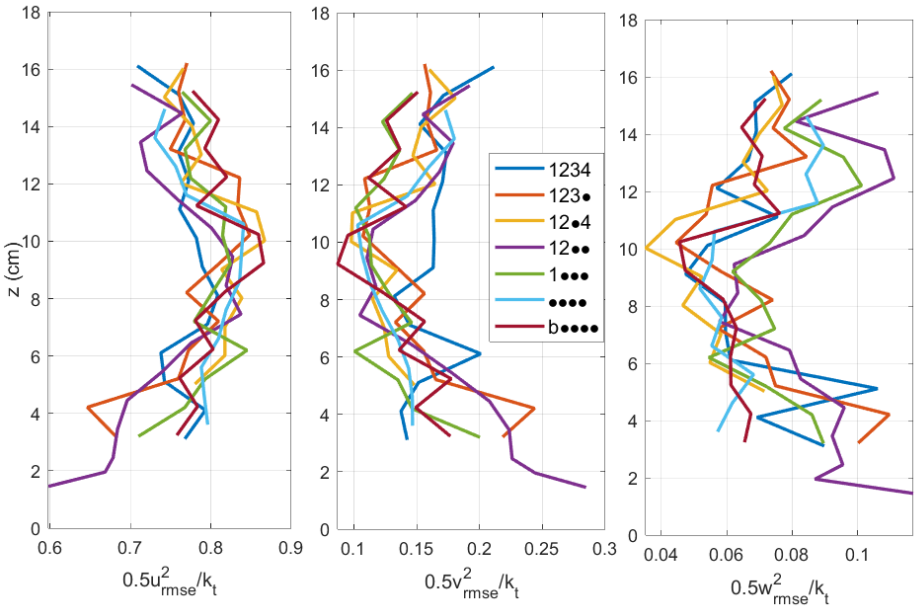


Figure 4.19: Streamwise, spanwise, and vertical fractions of the turbulent kinetic energy for MB experiments

These findings suggest that in vegetated flows over mobile dunes, the geometry of the bedforms plays a dominant role in controlling turbulence, rather than vegetation drag.

Finally, Figure 4.9 depicts the profiles of the integral length scale $l_t$ for both the MB and FB experiments. The estimated integral length-scale $l_t$ was compared with the findings from previous studies (Aberle and Järvelä, 2015; Nepf, 2012; Nepf and Vivoni, 2000). Consistent with the expectations, $l_t$ exhibited a scaling relationship with the equivalent diameter $d_e$ in the setup classified as dense vegetation. Notably, no clear effect was observed between the different mobile and fixed conditions, suggesting that the presence of mobility did not significantly impact the integral length scale in densely vegetated setups.

Moreover, in the absence of vegetation within the FB experiments and in the •••• setup within the MB experiments, the profiles of $l_t$ exhibited similarities to the results reported by Venditti and Bennett (2000). The

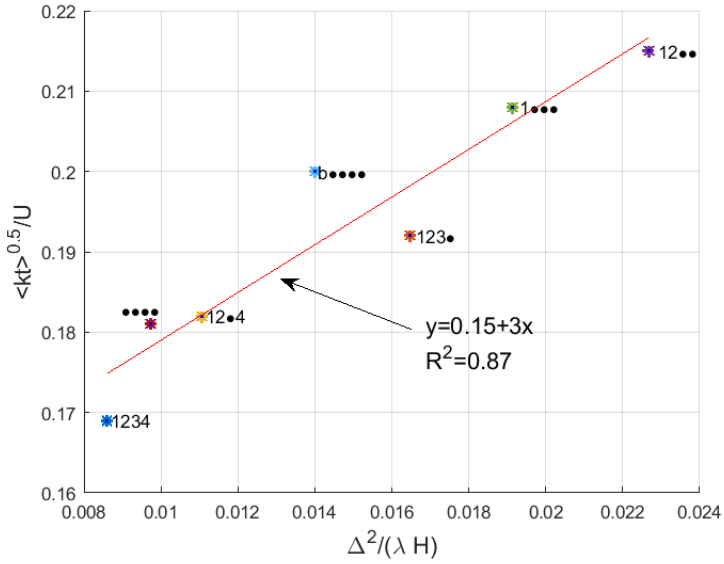


Figure 4.20: Turbulence intensity $\sqrt{\langle \overline{k_t} \rangle}_z / U$ plotted against dimensionless bedform geometry for MB experiments.

authors reported an integral length scale $l_t$ ranging from 0.06m to 0.13m at a height of 0.12m above the bed, obtained from experiments involving fixed 2D dunes in non-vegetated setups with similar dune geometries and hydraulic conditions of the present experiments, validating the results of this study.

Table 4.6: Flow characteristics and parameters for MB experiments.

| Setup | $C_D$ (-) | $C_D \langle a \rangle_z H$ (-) | U (m/s) | $\langle \overline{u} \rangle_z$ (m/s) | $\frac{(\langle \overline{u} \rangle_z - U)}{U}$ (%) | $d_e$ $(cm)$ | $\langle l_t \rangle_z$ $(cm)$ | $\langle k_t \rangle_z$ $(cm)$ | $\sqrt{\langle k_t \rangle_z}/U$ $(cm)$ |
|---|---|---|---|---|---|---|---|---|---|
| 1234 | 1.25 | 0.225 | 0.36 | 0.29 | -19% | 3.73 | 2.33 | 0.0037 | 0.169 |
| 123• | 0.97 | 0.162 | 0.39 | 0.33 | -15% | 3.45 | 2.70 | 0.0056 | 0.192 |
| 12•4 | 1.19 | 0.170 | 0.38 | 0.32 | -16% | 2.92 | 2.59 | 0.0048 | 0.182 |
| 12•• | 0.80 | 0.084 | 0.46 | 0.41 | -11% | 2.19 | 4.11 | 0.0098 | 0.215 |
| 1••• | 0.70 | 0.047 | 0.55 | 0.54 | -2% | 1.36 | 5.87 | 0.0131 | 0.208 |
| b•••• | 1.00 | 0.025 | 0.69 | 0.67 | -3% | 0.63 | 6.53 | 0.0190 | 0.200 |
| •••• | 1.20 | 0.016 | 0.81 | 0.77 | -5% | 0.30 | 8.15 | 0.0215 | 0.181 |

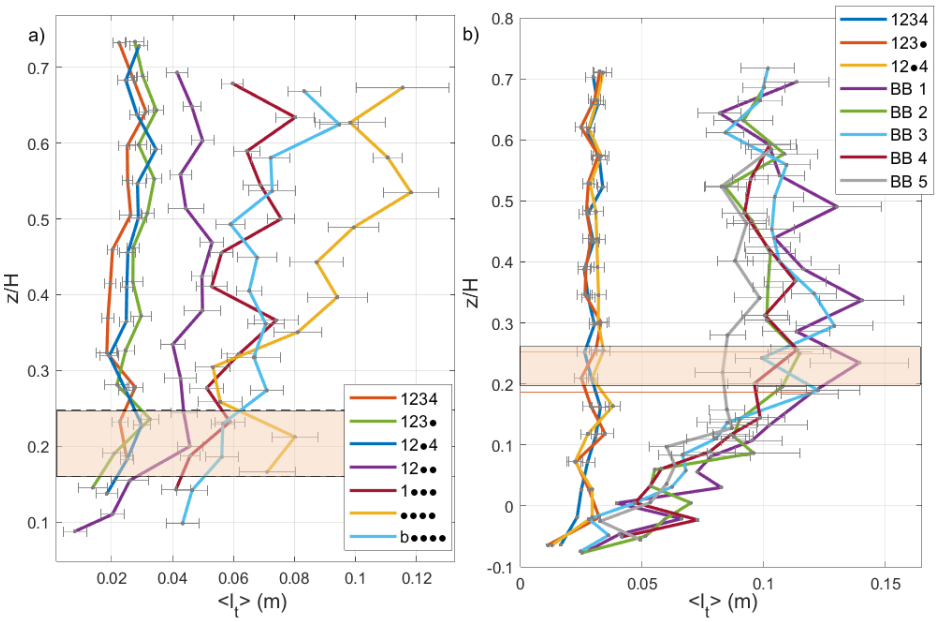


Figure 4.21: Double-averaged $\langle l_t \rangle$ resulted from a) MB experiments and b) FB experiments. The dashed lines represent the maximum bed level observed among the experimental runs. z=0 is the mean bed level.

### 4.5.3 Validation of Predicting Models for Turbulent Kinetic Energy and Bed-load Transport Rate

In this study, the model developed by Xu and Nepf (2020) was employed to predict the double-averaged turbulent kinetic energy ($k_t$) by considering vegetation characteristics, such as vegetation frontal area ($\langle a \rangle_z$), solid volume fraction ($\phi$), drag coefficient ($C_D$), and the estimated integral length scale ($l_t$).

The comparison between the predicted $k_t$ values, obtained from Equation 4.6, and the measured double-averaged $k_t$ values is depicted in Figure 4.22. The agreement between the predicted and measured values was not entirely satisfactory. Particularly, for setups classified as dense vegetation patterns, characterized by a higher leaf mass, the model exhibited a tendency to overestimate the measured $k_t$ values of about 30%. Notable deviations of 103%, 36%, and 69% were observed for setups 1234,

Table 4.7: Flow characteristics and parameters for FB experiments.

| Setup | $A_f$ ($cm^2$) | $H$ (m) | U (m/s) | $\langle\overline{u}\rangle_z$ (m/s) | $\frac{(\langle\overline{u}\rangle_z - U)}{U}$ | $d_e$ ($cm$) | $\langle l_t\rangle_z$ ($cm$) | $\langle\overline{k_t}\rangle_z$ ($m^2/s^2$) | $\sqrt{\langle\overline{k_t}\rangle_z}/U$ (-) |
|---|---|---|---|---|---|---|---|---|---|
| 1234 | 75 | 0.234 | 0.36 | 0.37 | 3% | 3.21 | 2.56 | 0.0012 | 0.096 |
| 123• | 70 | 0.231 | 0.37 | 0.39 | 7% | 3.03 | 2.54 | 0.0013 | 0.098 |
| 12•4 | 60 | 0.232 | 0.37 | 0.38 | 5% | 2.59 | 2.70 | 0.0016 | 0.109 |
| BB 1 | - | 0.206 | 0.34 | 0.36 | 7% | - | 8.75 | 0.0009 | 0.089 |
| BB 2 | - | 0.194 | 0.36 | 0.39 | 8% | - | 7.68 | 0.0010 | 0.088 |
| BB 3 | - | 0.200 | 0.35 | 0.37 | 8% | - | 7.95 | 0.0010 | 0.091 |
| BB 4 | - | 0.179 | 0.39 | 0.43 | 11% | - | 6.96 | 0.0010 | 0.081 |
| BB 5 | - | 0.164 | 0.42 | 0.47 | 11% | - | 6.43 | 0.0012 | 0.082 |

123•, and 12•4, respectively. These discrepancies can be attributed to the intricate influence of leaf presence and their interconnections on the flow field, sediment dynamics, and subsequently, bedform morphology. It should be noted that the development of the model was based on the assumption of fixed plane bed conditions, which may not fully capture the complex interactions occurring in the presence of mobile bed. Interestingly, setups characterized by lower vegetation roughness density, specifically 12••, 1••• and b••••, exhibited closer agreement between the predicted and measured $k_t$ values. However, it is noteworthy that the data point •••• stood out as an outlier, displaying a deviation of 45%.

Moreover, based on the measured turbulent kinetic energy ($k_t$), an evaluation was conducted to assess the applicability of the Yang and Nepf (2018) model to the experimental data. Figure 4.23 illustrates a comparison between the model-predicted sediment transport rates (Equation 4.3) and the actual measurements in a dimensionless $q_s^* - k_t^*$ plane, where * denotes dimensionless quantities (Equations 4.4). Notably, the setups characterized by dense vegetation exhibited significant deviations from the model predictions, with the measured sediment transport rates being approximately 90% higher than the predicted values. This observation aligns with the previous findings (Chapter 3), indicating that the presence of leafy vegetation can considerably enhance the actual sediment transport. Conversely, for the leafless setup, the model overestimated the bed-load transport rate, which is reasonable considering the presence of suspended transport that might be not entirely captured of the sediment trap of the flume recirculating system resulting in underestimated mea-

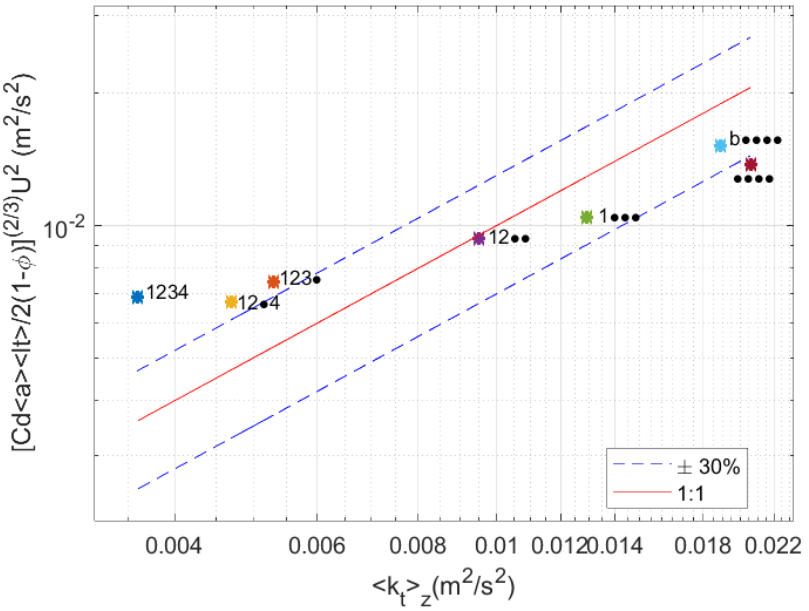


Figure 4.22: Comparison with measured $\langle \overline{k_t} \rangle_z$ and predicted using Xu and Nepf (2020) model.

sures of the bed-load rate. Moreover, it is worth noting that this deviation could also arise from the model applicability at the transition to the upper flow regime, where its validity might be compromised.

Nevertheless, the observed results suggest that the Yang and Nepf (2018) model is capable of predicting sediment transport rates based on turbulent kinetic energy ($k_t$), even in the presence of complex bedform geometry. It is worth noting that the original model was validated using rigid cylinders and small ripples.

However, to incorporate the impact of leafy vegetation, the model required further development. As a result, a correction was introduced, as shown in Figure 4.23, and expressed by Equation 4.10. A linear regression analysis was conducted on the data to determine the equation:

$$q_s^* = \gamma \langle k_t^* \rangle \tag{4.10}$$

where $\gamma = 0.229 \pm 0.0.15$. The uncertainty on the derived coefficient is estimated through 95% confidence intervals. In contrast to the original

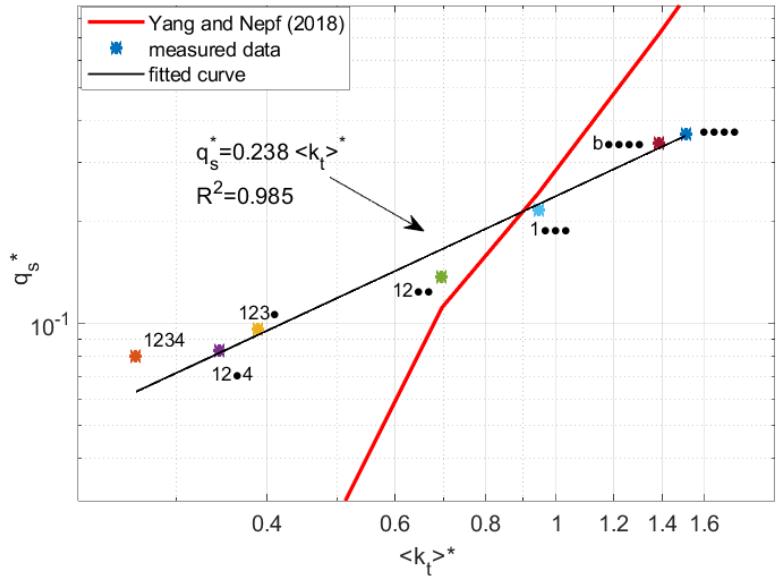


Figure 4.23: Modified Yang and Nepf (2018) $k_t$-based model for predicting bed-load transport rate.

model that accounts for near-bed values of $k_t$, the modified approach considers the depth-averaged $\langle k_t \rangle$. This modified approach takes into account the complex interactions between vegetation and dunes, providing a more accurate representation of the turbulent kinetic energy values in such complex scenarios.

## 4.6 Conclusions

In conclusion, the analysis of the experimental data presented in this study sheds light on the complex interactions between vegetation, bedform geometry, and turbulent flow characteristics in fluvial environments.

Experimental data suggested that dune geometry can be employed to express double- and depth-averaged turbulence kinetic energy. Thus, in vegetated flows over mobile dunes, the geometry of the bedforms seems to play a dominant role in controlling turbulence, rather than vegetation drag.

The presence of vegetation was found to dampen the flow separation zone of dunes. By reducing the intensity of flow separation, the presence of vegetation alters the scour and erosion downstream of the dunes, with implications for sediment transport.

The comparison between MB and FB experiments revealed distinct differences in turbulence intensity, emphasizing the need to consider these variations when investigating flow dynamics. The measured velocity profiles exhibited significant differences between the fixed bed and mobile bed conditions, despite considering the same plant configuration. Particularly noteworthy was the noticeable acceleration observed at the level corresponding to the missing branches elevation in the fixed bed, which was not evident in the mobile bed. Moreover, the MB experiments exhibited turbulence levels approximately two to three times higher than those observed in the FB experiments.

The integral length scale profiles demonstrated similarities to previous studies despite the complexities of the experimental conditions.

Furthermore, the application of the turbulence-based bed-load model by Yang and Nepf (2018) demonstrates reasonable accuracy for setups with low vegetation roughness density, whereas it underestimates the bed-load transport rates for setups characterized by dense vegetation patterns. This deviation can be attributed to the complex influences of leaf presence on sediment movement, dune geometry, and flow fields, which were not accounted for in the model, which was derived in presence of rigid cylinders and small ripples.

Finally, a modified model has been developed to account for the combined influence of leafy vegetation and dune presence, resulting in improved predictions of sediment transport rates in vegetated flows. To ensure enhanced accuracy and applicability, further validation and refinement of the model using extensive data on leafy vegetation are recommended.

Overall, this analysis highlights the importance of considering both bedform and vegetation effects when studying and modeling sediment transport processes.

# Chapter 5

# Flow Resistance Decomposition in Vegetated Channels with Dunes

Open channel flows exhibit a complex interplay between water depth, flow structure, and sediment transport, all intricately connected to hydraulic roughness. Numerous factors, including bed roughness, channel geometry, meandering, obstructions, vegetation (Chow, 1959; Yen, 2002; Nepf, 2012), and bed irregularities such as bedforms (van Rijn, 1984b), contribute to the resistance experienced by channel flow.

Among the factors influencing flow resistance, bedforms play a significant role. The resistance associated with bedforms depends on their geometry and hydraulic parameters, such as water depth and Froude number. As the height of bedforms increases, they impose more pronounced disruptions on the flow, resulting in greater energy loss and higher form drag. The rate of form drag induced by bedforms is further amplified by a higher ratio of bedform height to water depth or Froude number (Van der Mark, 2009). Additionally, the spacing and pattern of bedforms, whether out-of-phase or aligned, have a consequential impact on the exertion of form drag (Venditti, 2007). However, despite extensive research on bed shear stress over bedforms, the effects of three-dimensional bedforms on the flow field remain a subject of debate, with conflicting conclusions

drawn by different researchers (Van der Mark, 2009; Venditti, 2007; Maddux et al., 2003b).

Vegetation also contributes substantially to flow resistance and its effect is influenced by various factors. These factors include plant density, morphology, submerged or emergent conditions, spatial arrangement, and flow velocity (Aberle and Järvelä, 2013; Baptist et al., 2007; Armanini et al., 2005). Rigid vegetation, such as trees or reeds, offers resistance primarily based on its projected area and drag coefficient, following the concept of drag force. Specifically, the resistance scales with the squared velocity. On the other hand, flexible vegetation exhibits different hydraulic behaviors. As the flow velocity increases, flexible vegetation bend or sways in response to the fluid. This bending allows flexible plants to reduce their projected area, thereby decreasing their flow resistance. The bending of flexible vegetation also influences the drag coefficient ($C_D$) value (Schoneboom and Aberle, 2009). Previous research has acknowledged that leaves play a crucial role in governing the drag imposed by vegetation (Vogel, 1994). Thus, the behavior of flexible vegetation is more complex and cannot be accurately predicted using the drag force approach alone.

Accurate prediction of flow resistance is of fundamental importance for the successful implementation of river management strategies, as it serves as a fundamental parameter for flood control strategies and in the design of river restoration projects (Hou et al., 2019; Wang et al., 2023). Estimating the resistance exerted on the riverbed represents a significant challenge in fluvial engineering, as it requires a comprehensive understanding of the complex interactions and linkages among the various sources (Aberle and Järvelä, 2015; Box et al., 2021).

From a mechanical perspective, the hydraulic resistance in 1D steady uniform, fully developed open channel flow can be defined as the opposing forces acting per unit bed area that counteract the motion of the fluid. In uniform flows, the resisting forces must balance the component of the weight parallel to the flow direction (Einstein, 1950). This relationship can be expressed in dimensionless terms as follows:

$$\frac{\rho g R_h S}{\rho U^2} = c_{f,T} \tag{5.1}$$

where, $\rho$ represents the water density, $g$ is the gravitational acceleration,

$R_h$ denotes the hydraulic radius, $U$ is the cross-sectional averaged velocity, $S$ represents the friction slope, and $c_{f,T}$ signifies the dimensionless total resistance coefficient (Rebai et al., 2022).

Thus, in 1D steady uniform open channel flow, the expression of the total boundary shear stress, denoted as $\tau_0$, is commonly derived from the 1D Saint-Venant shallow water equations (Le Bouteiller and Venditti, 2015; Van der Mark, 2009):

$$\tau_0 = \rho g S R_h \tag{5.2}$$

By substituting the bed-related hydraulic radius $R_b$ for $R_h$ in Equation 5.2, the bed shear stress, $\tau_b$, can be obtained (Van der Mark, 2009):

$$\tau_b = \rho g S R_b = \rho c_{f,b} U^2 \tag{5.3}$$

where $c_{f,b}$ is the bed-related resistance coefficient. The two leftmost expressions of Equation 5.3 i.e., $\tau_b = \rho g S R_b$, are commonly referred to as the "depth-slope product". The bed-related hydraulic radius $R_b$ is determined through the side-wall effects correction procedure developed by Vanoni and Brooks (1957), which is further detailed in Appendix A. This procedure is applied to account for the influence of wall effects on the bed shear stress. It is typically employed when the bed roughness associated with the sediment is much different than the roughness of the channel walls. In laboratory setups, flume walls are usually smoother than the bed. Therefore, the correction accounts the increase in shear stress at the bottom and the decrease in shear stress at the wall caused by these side-wall effects. In contrast, in river channels, the opposite effect can occur, with higher shear stress occurring at the walls and lower shear stress at the bed.

According to Einstein and Banks (1950), the total bed resistance can be expressed as the sum of individual resistance components as long as they do not mutually interfere with each other. Einstein and Barbarossa (1952) further proposed that in the presence of bedforms, the total bed resistance can be separated into two components: skin friction and form drag. The skin friction component is associated with grain roughness, representing the resistance to flow caused by the shear stress exerted on individual grains on the riverbed. This component plays a significant role

in determining the bed-load transport rate (van Rijn, 1984a). On the other hand, the form drag component arises due to the pressure gradient along the length of the bedforms and results from the resistance to flow caused by the energy loss in the flow separation zone located at the lee side of the bedforms.

In the field of fluvial hydraulics, researchers have extensively investigated the application of the linear superposition principle in various scenarios, including the presence of vegetation. For instance, Petryk and Bosmajian (1975) applied the linear superposition principle to estimate the total bed shear stress as the sum of vegetation drag and skin friction. They developed an equation in terms of Manning coefficients on the basis of the linear superposition principle which was validated in presence of rigid vegetation and plane bed conditions. However, only a limited number of studies have specifically focused on examining the applicability of the linear superposition principle when dealing with two sources of form drag, such as vegetation and bedforms. It is worth noting that Le Bouteiller and Venditti (2015) calculated the bed shear stress by applying the linear superposition principle, considering the contributions of grain roughness, vegetation drag, and bedforms-related form drag, as shown in Equation 5.4.

$$\tau_b = \tau' + \tau''_d + \tau''_v \tag{5.4}$$

where $\tau'$ is the skin friction related to the grains roughness, $\tau''_d$ is the form drag related to the bedforms and $\tau''_v$ is the vegetation drag.

Moreover, by assuming that the components of bed shear stress can be related to the same average flow velocity, Equation 5.4 can be expressed in terms of resistance coefficients, as:

$$c_{f,b} = c'_f + c''_{f,d} + c''_{f,v} \tag{5.5}$$

where $c'_f$ is the grain resistance coefficient, $c''_{f,d}$ the form drag coefficient related to the dunes and $c''_{f,v}$ the form drag coefficient related to the vegetation. Particularly, $c_{f,T}$ includes also the side-wall roughness.

In their research, Le Bouteiller and Venditti (2015) assumed that the components of bed shear stress do not interact with each other. However, they found that this method provided reliable predictions of grain-related

shear stress and subsequent sediment transport in scenarios involving a ripple bed covered by rigid vegetation.

Despite the widespread adoption of the linear superposition principle, it is important to acknowledge that estimating grain resistance by subtracting vegetative form drag (and additional form drag contributions related to bedforms if present) from the total bed shear stress can introduce errors (Yen, 2002). This is due to the challenges in accurately characterizing complex vegetation morphology and the relatively large magnitudes of both total shear stress and vegetation form drag compared to skin friction (Wang et al., 2023; Nepf, 2012).

This study focuses on a scenario of open channel flow in which both vegetation and bedforms coexist. Such a scenario can occur in floodplains of alluvial rivers or drainage ditches. The presence of vegetation introduces additional drag forces, leading to alterations in flow patterns and sediment transport dynamics. Simultaneously, bedforms contribute roughness elements that further modify the characteristics of the flow. Therefore, a strong interplay between these factors influences the overall flow behavior and sediment transport processes.

The objective of this study is to assess the applicability of the linear superposition principle in such contexts and examine the impacts of mobile bed conditions on flow resistance components.

Building upon the previous work by Le Bouteiller and Venditti (2015), this study aims to extend the analysis of the applicability of the linear superposition principle in the presence of large-scale bedforms, such as dunes, and leafy flexible vegetation. Laboratory experiments were conducted under various conditions, including scenarios with mobile and fixed beds, both with and without vegetation.

To evaluate the contributions of vegetation and bedforms, predictive models available in the literature were utilized, and direct force measurements were performed. This comprehensive approach permitted the assessment of the composition of flow resistance in the presence of multiple sources of form drag.

## 5.1 Shear Stress Estimation

Double-averaged momentum equations are commonly used to investigate the flow field and fluid stress over rough boundary rather than Reynolds equation (i.e., time-averaged Navier Stokes equation) (McLean and Nikora, 2006; Finnigan and Shaw, 2008). Double-averaged momentum equations can be obtained through applying Equation 4.1 to the Reynolds equation. In 2D steady uniform flow, the double-averaged momentum equations can be expressed as (Nikora et al., 2007b, 2004):

$$\rho g S + \frac{1}{\Omega}\frac{d\Omega\tau}{dz} - f_p - f_v = 0 \tag{5.6}$$

where $S$ is the friction slope, $\Omega$ is the fraction of the averaging domain occupied by water, $f_p$ and $f_v$ are the form and viscous drag per unit fluid volume, respectively, resulting from the averaging procedure (Nikora et al., 2007a). $f_v$ is considered to be significant only at the bed level, where viscous stresses play a role in skin friction. Along with pressure drag on the grains, these forces contribute to the movement of the grains (Maddux et al., 2003a; van Rijn, 1984a).

In flows where form drag $f_p$ dominates over the viscous drag $f_v$, such as in a flow over bedforms, $f_p + f_v$ represent the summed contributions of skin friction and form drag due to the pressure gradient associated to the bed topography (Maddux et al., 2003a). Moreover, in presence of bed roughness elements, $f_p + f_v$ can be estimated as the exerted drag force: $(f_p + f_v) \approx 0.5\rho C_D a \langle\overline{u}\rangle^2$ where $C_D$ is the drag coefficient, $a$ is the roughness density, and $\langle\overline{u}\rangle$ the double-averaged velocity (Nikora et al., 2007b).

In Equation 5.6, $\tau$ is the total fluid stress which corresponds to the sum of three components: fluid viscous, turbulent and form-induced (or dispersive) stresses (Nikora et al., 2007a; Aberle et al., 2008; McLean et al., 1999; Nikora et al., 2004):

$$\tau = \rho\left(-\langle\overline{u'w'}\rangle - \langle\tilde{u}\tilde{w}\rangle + \frac{\nu}{\Omega}\frac{d\Omega\langle\overline{u}\rangle}{dz}\right) \tag{5.7}$$

where $\nu$ is the kinematic viscosity. Viscous fluid stress is negligible in high Reynolds number with respect to turbulence stress (Nikora et al., 2007b).

Dispersive stress $-\langle\tilde{u}\tilde{w}\rangle$ can be used to individuate the upper boundary of the roughness layer since in turbulent flow, $\langle\tilde{u}\tilde{w}\rangle$, $f_p$ and $f_v$ are negligible above the roughness tops (Aberle et al., 2008). However, in the presence of three-dimensional (3D) dunes, $\langle\tilde{u}\tilde{w}\rangle$ dominates the entire water depth, which differs from the behavior observed in two-dimensional (2D) dunes (Maddux et al., 2003a). Maddux et al. (2003a) applied Equation 5.6 in presence of 3D dunes assuming that $\langle\overline{w}\rangle \approx 0$, and that the presence of the walls would not affect the flow field (i.e., infinitely large domain). Moreover, in their study, due to the bed topography, the flow resulted periodic and symmetric about the centerline. Whit these assumptions, the spatially averaged streamwise momentum equation becomes:

$$\rho g S \int_z^H A\, dz = -\rho A\langle\overline{u'w'}\rangle - \rho A\langle\tilde{u}\tilde{w}\rangle + \tau' + \tau'' \tag{5.8}$$

where $\tau'$ is the skin friction and $\tau''$ is the form drag. These quantities represent average values over a dune bed (Maddux et al., 2003a). Equation 5.8 neglects the flux of momentum through the sides of the control volume. The control volume in consideration is bounded by the free surface and the $x-y$ plane at an elevation $z$ above the average bed level. At the bed, i.e. at the trough level, the spatially averaged Reynolds stress $-\rho\langle\overline{u'w'}\rangle$ and form-induced stress $-\rho\langle\tilde{u}\tilde{w}\rangle$ vanish in Equation 5.8 due to the no-slip condition (Maddux et al., 2003a), resulting in only the sum of skin friction and form drag, while the term on the left becomes the total boundary shear stress $\tau_b$, which can be determined by calculating the depth-slope product.

Nepf (2012) discusses various methods to estimate the bed shear stress, specifically the skin friction acting on the grains. One method involves defining the bed stress as the spatial average of the viscous stress at the bed. However, this approach necessitates fine-scale velocity measurements within the laminar sub-layer, which is often challenging to obtain due to instrumentation limitations. Another method involves estimating the bed stress based on the maximum near-bed Reynolds stress or by extrapolating the linear profile of Reynolds stress to the bed. In the context of vegetated channels, the method can be adapted by considering the spatially averaged value:

$$\tau' \approx \langle\overline{u'w'}\rangle_{max} \tag{5.9}$$

Maddux et al. (2003a) used Equation 5.8 to estimate the total boundary shear stress in flow over fixed quasi-3D dunes. The authors observed that, unlike 2D dunes, the total boundary shear stress $\tau_b$ in the presence of 3D dunes cannot be predicted solely based on the spatially averaged Reynolds stress. 3D dunes were found to exhibit significantly higher resistance compared to 2D counterparts. This increased resistance was attributed to form-induced stress, associated to the presence of secondary currents. However, considering all terms of the momentum equation, including fluxes through the sides of the control volume (Equation 29 in Maddux et al., 2003a), the complete spatial-averaged momentum equation provided a good approximation of the observed total boundary stress, inferred by using depth-slope product, resulting in a deviation of approximately $\pm 25\%$ from the depth-slope product value and a deviation of approximately $\pm 5\%$ from the sum of skin friction and form drag.

## 5.2 Materials and Methods

In this analysis, the experiments conducted in mobile-bed conditions and previously described in Chapter 3 are considered.

Additional experiments were conducted with the same vegetation elements and the same fixed dunes used in the previous FB experiments (described in Section 4.4.1). The purpose of these new experiments was to directly measure the hydraulic forces both related to the dunes and plants in order to understand the composition of flow resistance.

On the basis of the applied hydraulic conditions, bed shear stress components as skin friction, form drag due to the dunes and due to the plants, were calculated following formulations reported in Section 5.2.1. These components were then summed up and compared with the observed total bed shear stress estimated using the depth-slope product to verify the applicability of the linear superposition principle (Equation 5.4) in the considered conditions.

### 5.2.1 Flow Resistance Prediction

Over the past 60 years, numerous formulations and relationships have been proposed to develop practical procedures for estimating flow resistance in open channel flows.

In this study, we referred to the work of Van der Mark (2009), who conducted a detailed review of existing methods for predicting shear stress associated with grain friction and bedform-related form drag. Van der Mark (2009) identified the best models to be used with alluvial flume data which are presented below.

Van der Mark (2009) suggested to consider the grain friction model proposed by Engelund (1966) for estimating the skin friction, given by the equation:

$$\frac{U}{u'_*} = 6 + \frac{1}{\kappa} ln \frac{u'_*}{g S_f k_s} \tag{5.10}$$

where $\kappa$ is the von Karman constant assumed as $\kappa$=0.4 (e.g.,Coles (1956)), $u'_*$ is the shear velocity due to the grain resistance only and $k_s$ equals $2D_{65}$. By performing an iterative procedure, $u'_*$ can be derived, and the resistance acting on the grains can be estimated as $\tau' = \rho {u'_*}^2$, considering that $c'_f = (u'_*/U)^2$.

Furthermore, in combination with the Engelund (1966) model, Van der Mark (2009) suggested applying the model proposed by Yalin (1964) and Engelund (1966) for calculating bedforms form drag, give by the equation:

$$c''_{f,d} = \alpha \frac{\Delta^2}{2H\lambda} \tag{5.11}$$

where $\Delta$ is the dune height, $\lambda$ is the dune wavelength, $H$ is the water depth. $\alpha = 2.5exp(-2.5\Delta/H)$ is a calibration factor introduced by Engelund (1977) and determined experimentally using the data from Guy et al. (1966). The obtained resistance coefficient $c''_{f,d}$ was used to predict the bedforms-related form drag as $\tau''_d = \rho c''_{f,d} U^2$.

Current models for estimating vegetative drag often rely on the rigid-stem analogy, with only a few models specifically addressing the effects of flexible plants (Vargas-Luna et al., 2015).

For simple-shaped rigid elements, the exerted vegetative drag is typi-

cally estimated using the drag force equation:

$$F_D = \frac{1}{2}\rho C_D A_f U^2 \tag{5.12}$$

where $U$ is the the characteristic approach velocity, $C_D$ is the drag coefficient, $A_f$ denotes the plant frontal area. Thus, the spatially-average bed shear stress related to the vegetation form drag is estimated as (Jalonen et al., 2013; Järvelä, 2004):

$$\tau_v'' = \rho c_{f,v}'' U^2 = \frac{\langle F_D \rangle}{a_x a_y} \tag{5.13}$$

where $a_x$ and $a_y$ represent the spacing between plants in the x and y directions, respectively.

Despite the dominance of wake flow and sheltering effects in the flow structure within a canopy (Schoneboom et al., 2010), it is common practice to assume that $U$ in Equation 5.12 equals the cross-averaged velocity within a vegetation patch (Armanini et al., 2005; Vargas-Luna et al., 2015). When estimating the vegetative drag for leafless conditions, Equation 5.12 is employed with the drag coefficient $C_D$ derived from the equation proposed by Chapman et al. (2015) (Chapter 4).

Moreover, the approach proposed by Järvelä (2004) is considered for estimating the shear stress related to the leafy plants. This approach incorporates the leaf area index ($LAI$) and species-specific parameters, such as the drag coefficient $C_{D_\chi}$ and the Vogel exponent $\chi$, which accounts for streamlining effects. The model equation provides the Darcy-Weisbach friction factor related to vegetation drag, expressed as follows:

$$f_v'' = 4 C_{D_\chi} LAI \left(\frac{U}{U_\chi}\right)^\chi \frac{h_p}{H} \tag{5.14}$$

where $U_\chi$ is the lowest mean velocity in determining $\chi$ and $h_p$ is the deflect plant height. Therefore, the vegetation form drag resistance coefficient can be determined as $c_{f,v}'' = f_v''/8$ (Yen, 2002), which can be utilized in Equation 5.13 to estimate the spatially-averaged bed shear stress related to vegetation drag. Despite the requirement of species-specific coefficients, which need to be determined through appropriate measurements, the formulation proposed by Järvelä (2004) has been proven to provide good estimates in different studies (Jalonen et al., 2013; Box et al., 2021).

Finally, to accurately estimate the total bed shear stress, it is advisable to consider corrections for non-uniformity and side-wall effects in flume data (Guo (2015) and references within). The correction for side-wall effects can be achieved by incorporating the parameter $R_b$, as outlined in Equation 5.3. Regarding non-uniformity, a correction expression can be derived from the 1D depth-integrated Saint-Venant equations, accounting for a convective acceleration term. The resulting equation is as follows:

$$\tau_b = \rho g R_b S_{wse} + \rho U^2 \frac{\partial h}{\partial x} \tag{5.15}$$

Here, $\frac{\partial h}{\partial x} = S_b - S_{wse}$ represents the difference between the average bed slope and the water surface slope. This equation was derived and used by Le Bouteiller and Venditti (2014) and Guo (2015) in their studies.

### 5.2.2 Experimental activities

The analysis presented in this chapter encompasses experimental activities conducted under both mobile-bed and fixed-bed conditions. The mobile-bed data refer to the MB experiments, described in Chapter 3. On the other hand, for the fixed-bed conditions, new experiments were conducted specifically for direct measurements of hydraulic forces (HF), as detailed in the following section.

The physical model of fixed dunes was constructed based on the same digital elevation model derived from the final topography of the mobile-bed experiments (further details in Section 4.4).

The same artificial flexible plants were used in all the experiments conducted in this thesis. A fixed plant density of $m$=25 plants/$m^2$ was used throughout the experiments. All the experiments were conducted under spatially-averaged quasi-uniform flow conditions, in which the plants were just submerged. In experiments without plants, the water depth was kept the same as in the vegetated setup. The plant characteristics such as $LAI$, $C_{D_\chi}$, $u_\chi$ and $\chi$, used to estimate the form drag related to the vegetation, are known from previous studies (e.g., Schoneboom and Aberle (2009); Jalonen et al. (2013); Aberle et al. (2011)) and are reported in Table 5.1.

While estimating the drag force exerted by b●●●● plant setup, which features a complex plant morphology with a bare stem and a blossom on

Table 5.1: Plants species-specific parameters.

| Setup | $LAI$ (-) | $C_{D_\chi}$ (-) | $\chi$ (-) | $u_\chi$ (m/s) | $d_e$ (cm) | $a_z$ ($m^{-1}$) | $A_f$ ($cm^2$) | $h_p$ (m) |
|---|---|---|---|---|---|---|---|---|
| 1234 | 0.93 | 0.47 | -0.82 | 0.13 | 3.73 | 0.933 | 72.0 | 0.19 |
| 123• | 0.59 | 0.52 | -0.85 | 0.14 | 3.45 | 0.863 | 67.0 | 0.19 |
| 12•4 | 0.66 | 0.49 | -0.92 | 0.14 | 2.92 | 0.731 | 57.0 | 0.20 |
| 12•• | 0.32 | 0.36 | -0.73 | 0.21 | 2.19 | 0.547 | 42.0 | 0.19 |
| 1••• | 0.17 | 0.38 | -0.68 | 0.26 | 1.36 | 0.341 | 27.0 | 0.20 |
| b•••• | - | 1.00 | - | - | 0.63 | 0.156 | 12.6 | 0.20 |
| •••• | - | 1.20[a] | - | - | 0.30 | 0.075 | 5.40 | 0.18 |

*a*: $C_D$ value estimated following Chapman et al. (2015).

top, a drag coefficient value of $C_D = 1$ was chosen. This value is commonly used in vegetation studies (Vargas-Luna et al., 2015; Aberle and Järvelä, 2013). Conversely, for the •••• setup, the drag coefficient was determined using the equation proposed by Chapman et al. (2015), which is applicable to flexible cylinders (Table 5.1).

The experimental conditions employed in all the conducted experiments are summarized in Tables 5.2 and 5.3.

### Fixed-bed Experiments for Direct Measurements of Hydraulic Forces (HF)

The experiments were conducted in a 30-m long, 0.4-m deep, and 0.6-m wide tilting flume in the hydraulic laboratory of the Leichtweiß-Institut für Wasserbau (LWI) of the Technische Universität Braunschweig.

The fixed dune physical model used in these experiments was constructed using the same DEM that was previously analyzed and validated in Section 4.4. A 1.5-meter-long section of the DEM was 3D-printed using expanded polystyrene material and installed in the measurement area (Figure 5.1). To ensure fully developed flow conditions in the measurement area, additional sections of the DEM were added upstream and downstream of the printed model.

The extended physical model was replicated using wooden boards, which were shaped to match the extracted cross sections of the DEM.

Table 5.2: Hydraulic conditions applied for the MB experiments. $U$ is the channel averaged velocity as $U = Q/WH$. The average uncertainty of the measured $S_{wse}$ is estimated at $\pm 0.002\%$, while the one related to $S_b$ is estimated as $\pm 0.0009\%$. $R_b$ represents the bed-related hydraulic radius, and the percentage deviation from H is indicated inside the brackets.

| Setup | Q (l/s) | $Q_s$ (g/s) | H (m) | U (m/s) | $Fr$ (-) | $S_b$ (%) | $S_{WSE}$ (%) | $R_b$ (m) |
|---|---|---|---|---|---|---|---|---|
| 1234 | 47.8 | 21.8 | 0.22 | 0.36 | 0.24 | 0.90 | 0.92 | 0.22 (1%) |
| 123• | 51.5 | 26.0 | 0.22 | 0.38 | 0.26 | 0.88 | 0.89 | 0.22 (1%) |
| 12•4 | 53.0 | 22.0 | 0.23 | 0.39 | 0.26 | 0.85 | 0.86 | 0.22 (1%) |
| 12•• | 60.5 | 35.9 | 0.22 | 0.46 | 0.31 | 1.01 | 0.89 | 0.21 (2%) |
| 1••• | 73.4 | 51.6 | 0.22 | 0.55 | 0.37 | 0.98 | 0.86 | 0.21 (2%) |
| b•••• | 94.1 | 76.0 | 0.23 | 0.69 | 0.46 | 0.86 | 0.85 | 0.20 (3%) |
| •••• | 106.1 | 86.5 | 0.22 | 0.81 | 0.55 | 0.76 | 0.76 | 0.20 (5%) |
| bare bed | 130.5 | 204.5 | 0.23 | 0.97 | 0.65 | 0.48 | 0.54 | 0.22 (6%) |

These cross sections were spaced 20 cm apart along the longitudinal direction. Foam was used to fill the gaps between the wooden boards to ensure a smooth and continuous surface. This foam layer was then covered with a manually modeled cement layer to accurately mimic the surface of the DEM. The physical model had an upstream extension of 2.2 meters and a downstream extension of 1.3 meters. Combining these sections with the 1.5-meter-long 3D-printed section, the total length of the fixed dune model reached 5 meters (see Figure 5.1). The extended model was securely attached to the flume using metal plates adhering to the walls (Figure 5.3), while the printed dunes were fixed onto supports within the measurement area using glue, ensuring stability throughout the experiments.

Water discharge was regulated using a valve and measured using a KROHNE 090K inductive flow meter (precision $\pm 0.3\%$). To monitor the water surface elevation, a system consisting of 8 piezometers connected to the flume bottom was employed (Figure 5.3). These piezometers were positioned between 13-17 meters from the inlet section (refer to Figure 5.1). An automatic traverse equipped with a Microsonic mic+130/IU/TC ultrasonic sensor completed the necessary setup for accurate water surface elevation measurements. The ultrasonic sensor, with a precision of approximately $\pm 0.15\%$, moved over the piezometers and measured the wa-

Table 5.3: Applied hydraulic conditions in the HF experiments. The average uncertainty of the measured $S_{wse}$ is estimated at ±0.08%, considering 95% confidence intervals. $R_b$ represents the bed-related hydraulic radius, and the percentage deviation from H is indicated inside the brackets.

| Setup | Q (l/s) | H (m) | U (m/s) | $Fr$ (-) | $S_b$ (%) | $S_{WSE}$ (%) | $R_b$ (m) |
|---|---|---|---|---|---|---|---|
| 1234 | 16.3 | 0.23 | 0.12 | 0.08 | 0.126 | 0.266 | 0.22 (1%) |
| 1234 | 19.7 | 0.23 | 0.15 | 0.10 | 0.159 | 0.305 | 0.22 (1%) |
| 1234 | 23.1 | 0.22 | 0.17 | 0.12 | 0.205 | 0.443 | 0.22 (1%) |
| 1234 | 27.7 | 0.23 | 0.20 | 0.14 | 0.248 | 0.533 | 0.22 (1%) |
| 12•4 | 20.9 | 0.23 | 0.15 | 0.10 | 0.126 | 0.276 | 0.23 (2%) |
| 12•4 | 24.0 | 0.22 | 0.18 | 0.13 | 0.159 | 0.340 | 0.22 (2%) |
| 12•4 | 28.3 | 0.23 | 0.21 | 0.14 | 0.205 | 0.431 | 0.23 (2%) |
| 12•4 | 32.4 | 0.22 | 0.24 | 0.16 | 0.248 | 0.528 | 0.22 (2%) |
| 12•• | 27.6 | 0.23 | 0.20 | 0.14 | 0.126 | 0.258 | 0.22 (3%) |
| 12•• | 33.8 | 0.23 | 0.25 | 0.16 | 0.159 | 0.334 | 0.22 (3%) |
| 12•• | 38.2 | 0.23 | 0.28 | 0.19 | 0.205 | 0.428 | 0.22 (3%) |
| 12•• | 43.6 | 0.22 | 0.32 | 0.22 | 0.248 | 0.546 | 0.22 (3%) |
| •••• | 43.9 | 0.23 | 0.32 | 0.21 | 0.126 | 0.259 | 0.22 (5%) |
| •••• | 48.2 | 0.23 | 0.35 | 0.24 | 0.159 | 0.303 | 0.22 (5%) |
| •••• | 54.8 | 0.23 | 0.41 | 0.27 | 0.205 | 0.408 | 0.21 (5%) |
| •••• | 61.5 | 0.23 | 0.45 | 0.30 | 0.248 | 0.505 | 0.22 (5%) |
| bare bed | 46.3 | 0.21 | 0.37 | 0.26 | 0.126 | 0.264 | 0.21 (6%) |
| bare bed | 50.3 | 0.19 | 0.44 | 0.33 | 0.159 | 0.316 | 0.19 (7%) |
| bare bed | 57.1 | 0.21 | 0.46 | 0.32 | 0.205 | 0.408 | 0.21 (6%) |
| bare bed | 65.1 | 0.21 | 0.53 | 0.37 | 0.248 | 0.492 | 0.21 (6%) |

ter level for a duration of 2 minutes at each location (refer to Figure 5.3). Hence, the total duration of measuring the water surface elevation along the flume was 16 minutes. The collected data from the piezometers were used to calculate the water surface slope, which was subsequently validated by means of a comparison with the readings from five point gauges positioned at various locations along the flume (Figure 5.1).

To determine dune form drag, a shear plate (SP) was employed, while vegetation drag was measured using six drag force sensors (DFSs) (Figure 5.2). Both hydraulic forces were measured over a period of 600 seconds, with a high sampling rate of 1615 Hz.

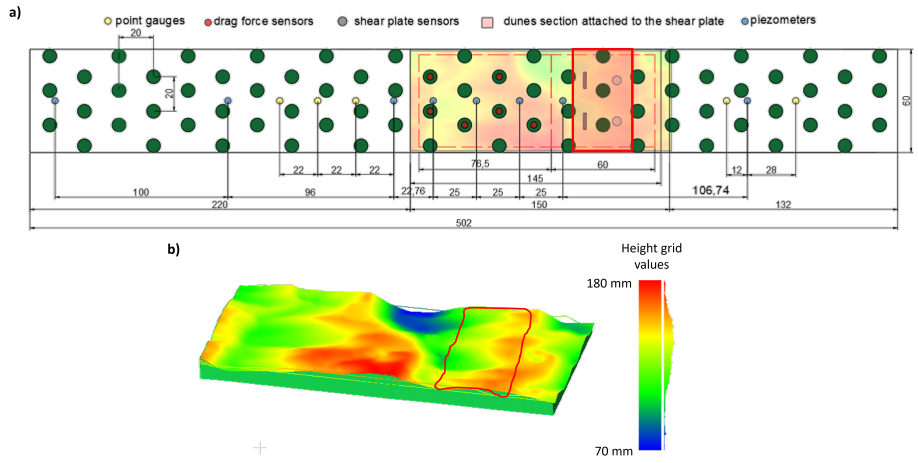


Figure 5.1: LWI flume setup: a) plan view of the measurement area: the red rectangle represents the position where the shear plate is located, the colored area represent the 3D-printed dune model, where the colors indicate the bed elevation, with red representing the highest points and green representing the lowest, the white area indicate the flume section covered by the "hand-made" dune model; b) DEM with the shear plate (SP) area highlighted.

The utilization of drag force sensors (DFSs) to quantify the drag force exerted by plants has been demonstrated as an effective approach in previous studies (Schoneboom et al., 2008; Niewerth et al., 2016; Jalonen et al., 2013; Västilä and Järvelä, 2014). Particularly, the DFS consists of a stainless steel beam measuring 3 mm in thickness, 20 mm in width, and 17 cm in length. Each one is equipped with eight strain gauges configured as two Wheatstone full bridges, positioned at a distance $l$ from each other.

The plants were connected to metal sticks that passed through the dune layer and were then attached to the DFSs (Figure 5.2). Careful openings were made in the dunes layer to prevent any contact between the metal sticks and the dunes during the experiments, ensuring accurate measurements of vegetation-related form drag. When subjected to flow, the plants acted as cantilevers, generating bending moments and compression strains ($\epsilon_1$ and $\epsilon_2$) on the metal beam, which was rigidly connected to a base plane (Figure 5.2). The difference between the measured strains

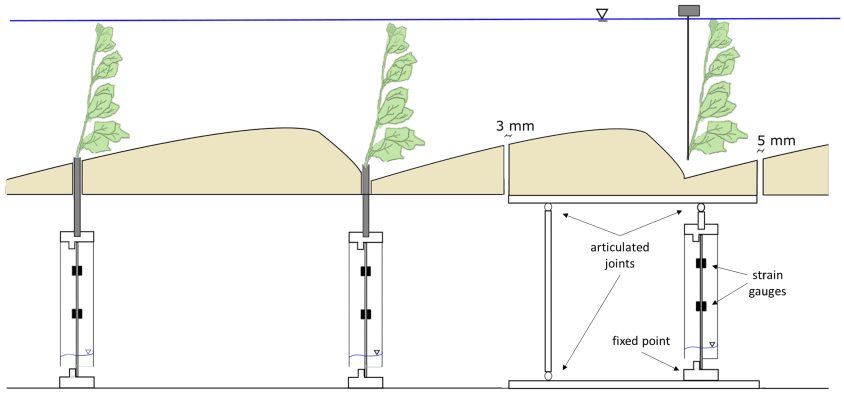


Figure 5.2: Flume setup for direct measurements of hydraulic forces in HF experiments. The depicted bed profile does not accurately represent the actual bed profile, which is reported in Figure 5.1.

are related to the drag force experienced by the plants, as expressed in Equation 5.16.

On the other hand, the form drag associated with the dunes was measured using a shear plate (SP). Other studies on bed shear stress have employed shear plates, each one characterized by the use of different types of sensors or measurement methodology (Tinoco and Cowen, 2013; Park et al., 2019). The specific shear plate used in this work represents a modification of a previous design, reported in Niewerth et al. (2021). The novel shear plate consists of two DFSs connected to a horizontally movable head plate measuring 35 cm in length and 60 cm in width. The measurement mechanism is identical to that of the DFSs, where the resistance offered by the dunes to the flow causes the steel beam to bend. Prior to the experimental runs, the performance of the shear plate instrument was analyzed and validated through additional tests. The detailed results of these tests can be found in Section 5.2.3.

A spacing of 3-5 mm was maintained between the section of the head of the shear plate and the adjacent region (Figure 5.1). These distances were selected to exceed the maximum deflection of the steel beam, which is estimated equal to 0.9 mm for a force of 5 N, overestimating the actual

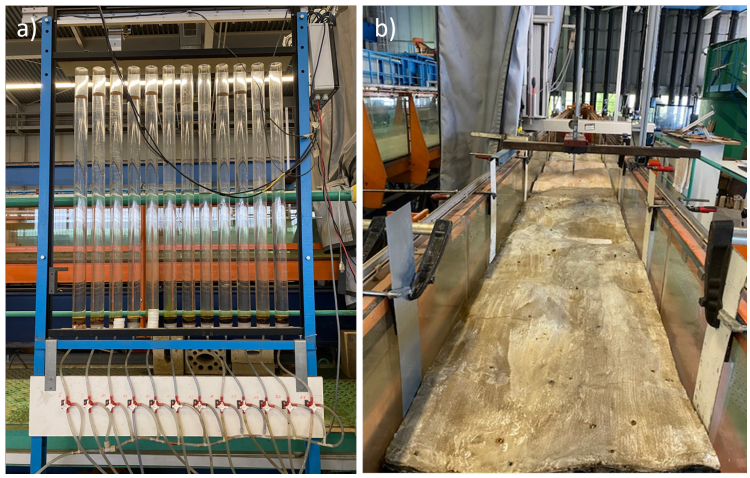


Figure 5.3: a) Eight piezometers were employed to measure the water surface elevation along the flume. A traverse system was installed above the piezometers, facilitating the movement of the ultrasonic sensor over them; b) the flume setup for HF experiments.

measurements. This precaution was used to ensure accurate measurements of dune form drag without interference from the surrounding area of the dunes model.

The length of the SP was set to 0.35 m to minimize the influence of the plants on the SP measurements (Figure 5.1). This configuration enabled the placement of a single row of plants above the shear plate, taking into consideration the spacing between them. The placement of these three plants was facilitated by a rigid extension, a 2 mm thick metal cylinder, affixed to a wooden board that was leaned against the flume walls. This careful setup prevented any contact between the vegetation and the fixed dune model.

This study considered five different plant stages, ranging from fully foliated plants to bare beds, as outlined in Table 5.3. The experimental program consisted of two phases: reference setups without vegetation and setups with vegetation. As in the previous experiments, the plants were arranged in a staggered pattern with a spacing of 20 cm in both directions (Figure 5.1) resulting in a plant density of m= 25 plants/$m^2$/. Each vegetated or bare bed setup experiment was conducted considering each of

four different selected flume slopes. The slopes were chosen based on their suitability for achieving quasi-uniform flow conditions within the limitations of the experimental setup, including the height of the flume walls and the length of the dunes model. Moreover, the accuracy of the SP measurements, as discussed in Section 5.2.3, played a crucial role in determining both the slopes and the hydraulic conditions. Consequently, the selection of slopes was carefully made to ensure accurate SP measurements throughout the experimental runs.

The experiments were conducted under quasi-uniform flow conditions, ensuring that the plants, when present, were just submerged. In all configurations, including both vegetated and non-vegetated setups, the water depth was kept constant for the respective flume slopes.

After setting the flume slope, the flap gate at the end of the flume and the discharge were adjusted in order to achieve quasi-uniform flow conditions, so that the water surface slope matched the flume slope. Any deviation from uniformity was accounted for in the calculation of the total shear stress using Equation 5.15. The water surface sensor was then activated, and after a period of approximately 30 minutes, in which the flow conditions stabilized, the measurements were started. The water sensor remained active for the entire experimental run, and hydraulic forces were measured at regular intervals of around 30 minutes.

To ensure the reliability of the measurements, the same experimental setup was repeated on different days. Specifically, two repetitions were conducted for the vegetated cases, while three repetitions were carried out for the runs without vegetation.

### 5.2.3 Measurements and Validation

The horizontal force (drag force) acting on a DFS can be calculated by determining the difference between the strains measured by the strain gauges ($\epsilon_1$ and $\epsilon_2$) and dividing it by the distance $l$ between the two Wheatstone full bridges.

$$F_D = \frac{\epsilon_1 - \epsilon_2}{l} EW \tag{5.16}$$

In this equation, $E$ represents the elastic modulus with a value of $200 N/mm^2$, and $W$ represents the second modulus of the beam, which is calculated

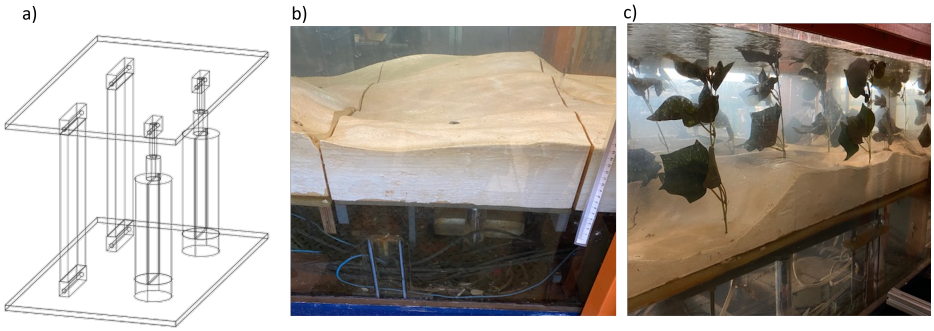


Figure 5.4: Instruments setup for measuring dune form drag and vegetation drag. a): a 3D sketch showing the shear plate with the two drag force sensors (DFSs) and two supports designed to restrict movements primarily in the horizontal direction; b) the shear plate connected to the fixed dunes model through the head plate; c) plants installed over the dunes and connected to the DFSs, which are positioned underneath the flume bottom.

as $wt^2/6$ where $w$ is the width and $t$ is the thickness of the beam. The calibration of the drag force sensors (DFS) aimed to determine the appropriate value for $l$ in order to accurately calculate the drag force using Equation 5.16.

The calibration procedure for the drag force sensors (DFS) involved applying known weights (50 g, 100 g, and 200 g) to a rigid cylinder attached to the head of the DFS. Using a pulley system, the known weights were applied to the rigid cylinder at various vertical distances from the head of the sensor. The distances ranged from 1 cm to 10 cm with a spacing of 1 cm. By analyzing the relationship between the applied forces and the measured forces that were estimated using Equation 5.16, the value of $l$ of the system can be determined through data fitting.

The average value of $l$ obtained from the calibration procedure was found to be 80.85 mm, with a standard deviation of 3.46 mm across the different DFSs. The error in the vegetative drag force, determined as the root mean square error (RMSE) between the measured and applied forces, averaged across the DFSs, was found to be 0.007 N.

Concerning the SP, the strain difference $\Delta\epsilon = \epsilon_1 - \epsilon_2$ is obtained by summing the strain differences measured by the strain gauges of the two

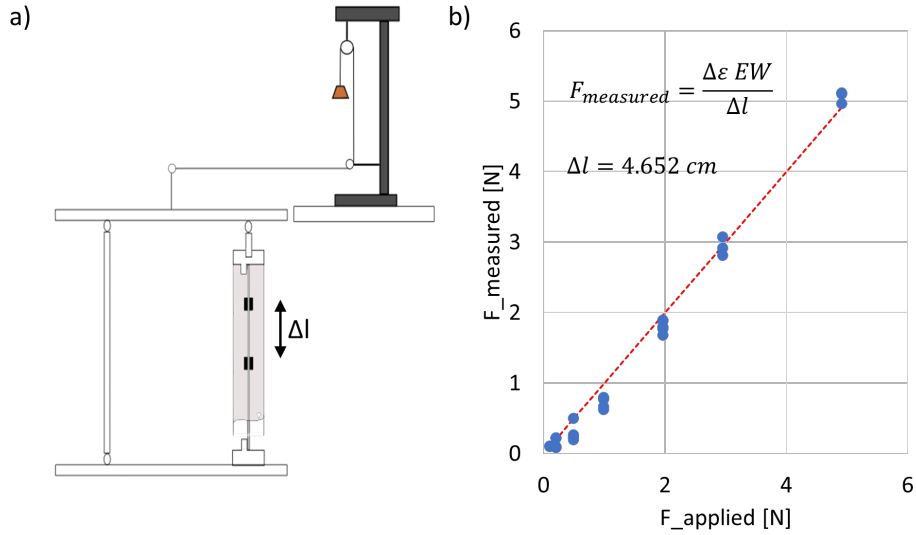


Figure 5.5: SP calibration: a) a simplified sketch illustrating the pulley system employed during the calibration process. The force was applied at two different point on the surface of the SP, using a non-elastic wire. The wire was aligned parallel to the longitudinal axis and connected to rings, from which the loads were hung; b) the linear regression obtained from the calibration procedure. It is evident that the uncertainty of the SP increases for applied forces lower than 1N.

DFSs. The calibration process for the SP was conducted in a similar manner to the DFS calibration. Known weights ranging from 100 g to 700 g were applied to the surface of the SP head plate using a pulley system. The calibration of the SP yielded a value of $l$=46.52 mm with a RMSE estimated in N as 0.176 (Figure 5.5).

Further validation was conducted to assess the reliability of the SP. One of the tests aimed to investigate the potential influence of the angle of force application on the measurements. The calibration procedure was performed with the pulley aligned at the center of the SP, while these additional tests were conducted by varying the point of force application within a range of 5 to 9 cm on both the left and right sides of the SP. These tests were performed both in the presence and absence of water. The applied weights during these tests ranged from 70 g to 500 g.

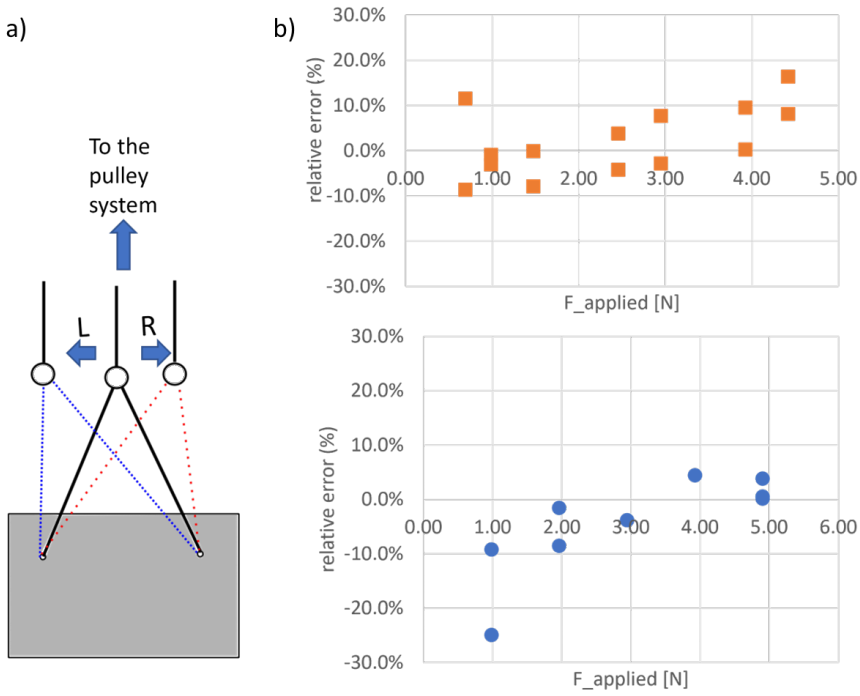


Figure 5.6: SP validation test: a) A sketch illustrating the application of forces to test the effect of the angle of force application; b) The obtained results of the test conducted in the absence of water (represented by orange dots) and in the presence of calm water (represented by blue dots).

The results of the validation tests revealed that the majority of the relative errors between the applied and measured forces were below 10% (Figure 5.6). This finding indicates that the accuracy of the SP measurements is not significantly influenced by the direction of force application, even in the case of potential presence of a strong secondary current.

Furthermore, an additional test was conducted to examine the relationship between the measured drag force and the squared velocity. In this test, a thin metal plate measuring 0.12x0.16 m was attached to the head plate of the shear plate. The plate was subjected to various flow velocities. The hydraulic parameters utilized in this test are provided in Table 5.4. Since the surface of the head plate was smooth, the bed shear

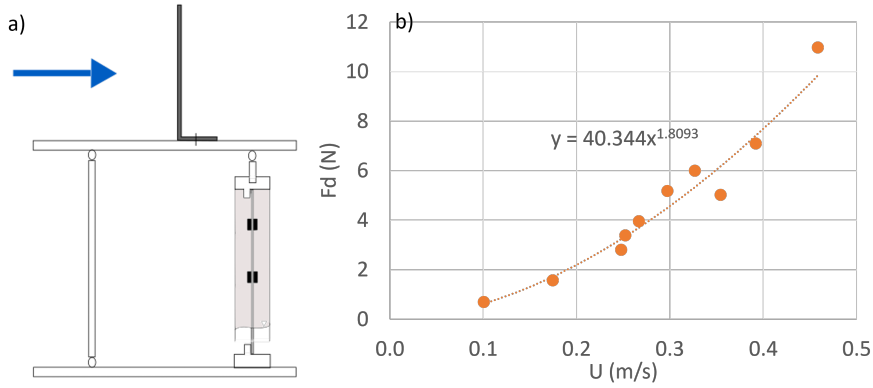


Figure 5.7: SP test: a) sketch showing the test setup utilizing the metal plate, with the measured force highlighted in blue; b) the obtained results of the test.

Table 5.4: Applied hydraulic conditions for the SP test with the metal plate.

| Q (l/s) | H (m) | U (m/s) | $F_{SP}$ (N) |
|---|---|---|---|
| 28.5 | 0.23 | 0.25 | 3.2 |
| 35.0 | 0.28 | 0.25 | 2.6 |
| 50.0 | 0.28 | 0.35 | 4.8 |
| 10.0 | 0.21 | 0.10 | 0.7 |
| 19.0 | 0.23 | 0.17 | 1.5 |
| 29.0 | 0.23 | 0.27 | 3.7 |
| 35.5 | 0.23 | 0.33 | 5.7 |
| 30.0 | 0.21 | 0.30 | 4.9 |
| 60.0 | 0.26 | 0.46 | 10.4 |
| 60.0 | 0.30 | 0.39 | 6.7 |

stress was neglected. The drag force exerted by the plate was measured and plotted against the flow velocity, revealing an approximately squared (power of 1.8) relationship between the measured drag force and velocity, as shown in Figure 5.7. This confirms adherence to the definition of drag force.

### 5.2.4 Data Analysis

In all experiments, the water surface elevation data was fitted with a linear regression to estimate the relative slope. The non-uniformity cor-

rection (Equation 5.15) was applied to all experiments results. This correction was particularly necessary for the fixed-bed experiments. Due to the limitations imposed by the experimental setups, including the limited length of the flume section occupied by the model and the restricted height of the flume walls, it was not possible to achieve perfect uniform flow conditions. Hence, the non-uniformity correction was applied to ensure more accurate and reliable results.

In the HF experiments, the data collected from both the DFSs and the SP were temporally averaged. This averaging process was conducted to ensure that the cumulative mean of each data series reached a stable value within the specified measurement duration of 600 seconds. The noise present in the measurements was effectively eliminated through averaging, as only the time-averaged values were considered in the analysis.

The measured vegetative drag ($\tau_{DFS}$) is estimated as the product of the plant density ($m = 25$ plants/$m^2$) and the spatially-averaged force measured by the six DFSs ($F_{DFS}$). On the other hand, the measured form drag associated with the dunes $\tau_{SP}$ is estimated as the ratio of the force measured by the SP ($F_{SP}$), to the area of the head plate of the shear plate $A_{SP}$.

To analyze the validity and applicability of the linear superposition principle, the comparison will be made between the estimated total bed shear stress using Equation 5.15, $\tau_b$, and the sum of the measurements obtained from the shear plate ($\tau_{SP}$) and drag force sensor ($\tau_{DFS}$). Additionally, the predicted values obtained from the flow resistance estimation models were be compared with $\tau_b$.

The uncertainty related to estimated or measured bed shear stress is calculated using the error propagation law (Muste et al., 2017). Specifically, the uncertainty can be expressed as:

$$u_c^2(\tau_b) = \sum_{i=1}^{N} \frac{\Pi^2}{(X_i)^2} u^2(X_i) \tag{5.17}$$

where $X_i$ is the considered variables (e.g., water depth, slopes), and $\Pi$ is the relationship used to calculate the total shear stress as the slope-depth product or the sum of measurements from the shear plate and drag force

sensors.

$$\Pi = \tau_b = \rho g H S_{wse} + \rho \left( \frac{Q}{WH} \right)^2 (S_b - S_{wse}); \tag{5.18}$$

$$\Pi = \tau_{SP+DFS} = \tau_{SP} + \tau_{DFS} = \frac{F_{SP}}{A_{SP}} + mF_{DFS} \tag{5.19}$$

The uncertainty associated with the bed-related hydraulic radius $u_c(R_b)$ is approximately equivalent to the uncertainty in water depth $u_c(H)$. It is assessed as the RMSE between the measured data ($H$) and the regression line data point ($H_{fit}$):

$$u_c(H) = \sqrt{\frac{\sum_{i=1}^{N} (H(i) - H_{fit}(i))^2}{N}} \tag{5.20}$$

The uncertainty related to the water surface elevation slope ($S_{wse}$) is estimated as the 95% confidence intervals of the linear fit coefficients. For the drag force sensors ($\tau_{DFS}$), the uncertainty is assessed using the sensors-average RMSE between the estimated forces and the applied loads during calibration. For the shear plate ($\tau_{SP}$), the uncertainty is estimated as the ratio of the RMSE of the shear plate forces concerning the calibration procedure to the area of the shear plate head. The resulting values are: $u_c(F_{SP}) = 0.84N$ and $u_c(F_{DFS}) = 0.24N$. Notably, the discrepancies observed in the measured values from the SP and DFSs across the multiple experimental setups, were found to be within the estimated uncertainty range of the measurements.

## 5.3 Results

### 5.3.1 Mobile-bed Experiments (MB)

Prior to examining the applicability of the linear superposition principle for bed shear stress contributions in the presence of dual form drag sources, a thorough validation process was conducted to assess the reliability of the calculated estimates based on the models presented in Chapter 5.2.1. This validation procedure involved comparing the outcomes obtained from the considered models with alternative formulations, ensuring their consistency and accuracy. Additionally, the results derived from the

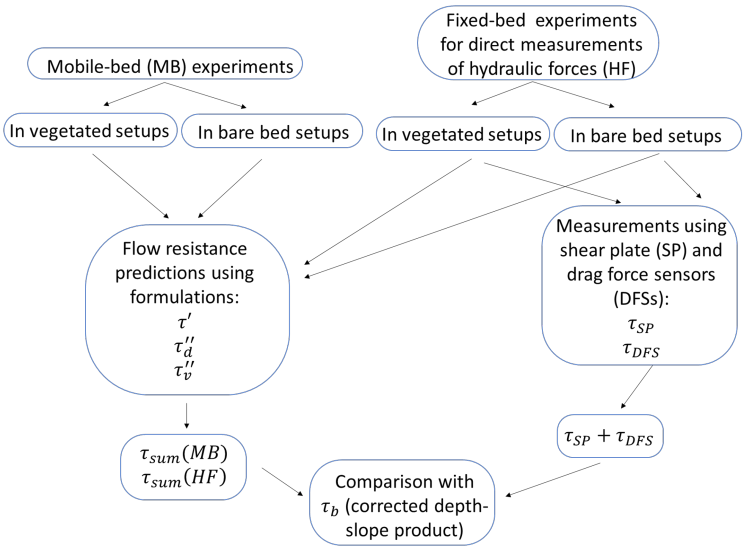


Figure 5.8: Summary diagram depicting the analysis conducted in this study to investigate the validity of the linear superposition principle.

vegetation-related form drag formulations were subsequently validated by means of the measures obtained from the DFSs (in Section 5.3.2). However, it is important to note that the vegetation drag formulations have been successfully applied in numerous studies featuring the same vegetation elements utilized in this study ( e.g., Aberle et al. (2011); Jalonen et al. (2013); Schoneboom et al. (2008)).

Concerning the skin friction, the values calculated using the formulation proposed by Engelund (1966) were considered to determine the flow regime based on the bedforms stability diagram developed by Van den Berg and van Gelder (1993). The diagram classifies the stability fields for flume equilibrium conditions in a $\tau'_*$-$D^*$ plane (see Figure 5.9), where $\tau'_*$ represents the Shields parameter associated with grain roughness only, and $D^* = D_{50}\left(\frac{1.65g}{\nu^2}\right)^{1/3}$ is the dimensionless particle diameter. As result, the occurrence of dunes was predicted in all experimental setups. However bare bed and leafless ●●●● configuration fell within the transition section of the diagram, lying between the dune and upper stage plane bed regimes. This is consistent with the reality because these two setups exhibited a

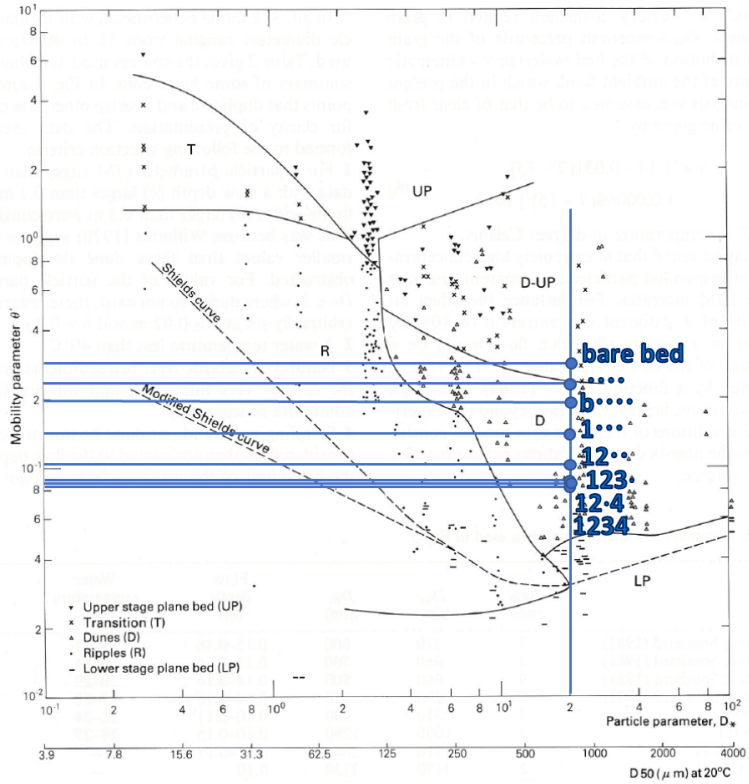


Figure 5.9: Van den Berg and van Gelder (1993) stability diagram showing the conditions resulted during the MB experiments.

higher level of suspended transport compared to the other configurations, as reported in Chapter 3. In these two setups, the average dune height was significantly lower, indicating an important decay process and supporting the classification of the flow regime based on the observed characteristics. Furthermore, the classification made on the basis of Van den Berg and van Gelder (1993) diagram were confirmed by the flow regime determination method proposed by Brownlie (1983). As a result, these observations provide evidence supporting the reliability of the estimated skin friction values, along with the results presented in Chapter 3 regarding the prediction of the bed-load transport rate.

According to Maddux et al. (2003a), the fluid stress estimated using Equation 5.8 over the maximum crest elevation is related only to the turbulent stress $\langle\overline{uv}\rangle$ and the disperse stress $\langle\tilde{u}\tilde{w}\rangle$, as skin friction and form drag are relevant only below the crest line. However, in presence of vegetation, this characteristic flow field structure might change. Nepf (2012) reported that skin friction values can be inferred from the near-bed peak of spatially averaged Reynolds stresses (Equation 5.9). Conversely, Nelson et al. (1995) claimed that this link might not be true in presence of nonuniform flow over dunes.

Velocity measurements were used to estimate fluid stress using Equation 5.7, assuming negligible viscous stress compared to turbulent stress. The predicted skin friction values, obtained from the formulation proposed by Engelund (1966), were then compared with the near-bed peak values of the fluid stress, under mobile-bed conditions.

In absence of vegetation, the profiles in MB experiments exhibited a substantially concave shape, which is a characteristic also confirmed by other studies (Afzalimehr and Anctil, 2000; Song and Chiew, 2001; Afzalimehr, 2010). However, the presence of leafy vegetation introduces a significant impact on the distribution of fluid stress, resulting in a relatively constant distribution along the vertical axis. This observation is consistent with previous studies on vegetated channels (Nepf and Vivoni, 2000; Ghisalberti and Nepf, 2004). Moreover, it is possible to note a significant influence of leaf vegetation gaps with an increase in fluid stress observed in proximity to the leaf gaps of the plants.

Upon comparing the values of these peaks, it was evident that in mobile-bed conditions, they closely matched the skin friction values, with an average deviation lower than 30%, thereby providing further validation for the accuracy of the predicted skin friction values obtained from velocity measurements (Figure 5.11). This finding aligns with the claim made by Nepf (2012) about using double-averaged Reynolds stress near-bed peaks to infer skin friction values. Nevertheless, in this study, the influence of nonuniform flow over dunes was taken into account, and the inclusion of dispersive stress provided more accurate estimates of skin friction values under mobile-bed conditions.

Furthermore, the dune-related form drag values obtained from the

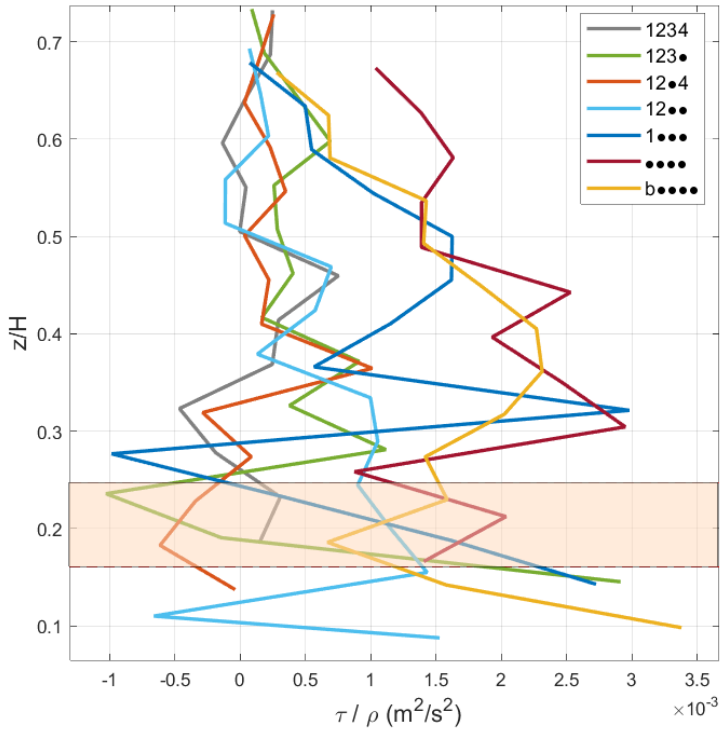


Figure 5.10: Double-averaged fluid stress $\tau$ resulting from MB experiments, estimated using Equation 5.7. The highlighted rectangle represents the range of the maximum bed elevation in the experimental runs.

models proposed by Yalin (1964) and Engelund (1966) were validated by comparing them with the outcomes of models that explicitly estimate the sum of skin friction and form drag of the dunes, namely the models developed by Engelund and Hansen (1967) and van Rijn (1984b).

The explicit empirical models by van Rijn (1984b) is based on determining the equivalent roughness of a movable bed surface in the lower, transitional and upper flow regime (with exception of anti-dunes) as:

$$K_s = 3D_{90} + 1.1\Delta(1 - exp(-25\Delta/\lambda)) \tag{5.21}$$

where $3 * D_{90}$ is the grain roughness related to flat bed conditions. Finally,

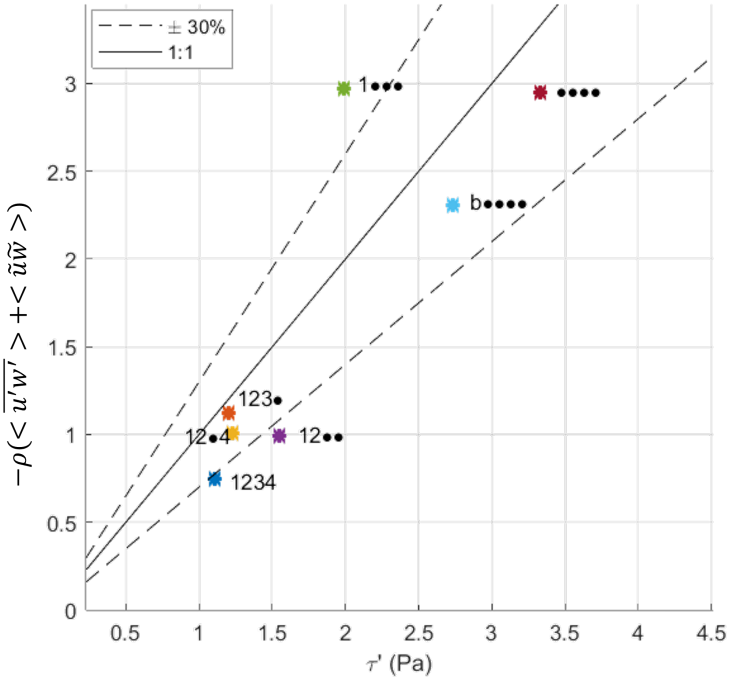


Figure 5.11: Comparison between the predicted skin friction $\tau'$ values and the peaks of the fluid shear stress inferred from velocity measurements as $-\rho(\langle\overline{u'w'}\rangle + \langle\tilde{u}\tilde{w}\rangle)$ for MB experiments.

the resistance coefficient can be computed as:

$$c_{f,VR} = g\left(18log_{10}(\frac{12R_b}{K_s})\right)^{-2} \tag{5.22}$$

The bed shear stress related to both skin friction and dune-related form drag can be calculated as:

$$\tau_{vR} = \rho c_{f,VR} U^2 \tag{5.23}$$

Similarly, Engelund and Hansen (1967) proposed an experimental relationship between the dimensionless shear stress related to the grain roughness $\tau'_*$ and the dimensionless total shear stress $\tau_*$, and it reads:

$$\tau_{*EH} = \sqrt{\frac{\tau'_* - 0.06}{0.4}} \tag{5.24}$$

Consequently, it is possible to derive $\tau_{EH} = \tau_{*EH} g(\rho_s - \rho) D_{50}$.

The comparison between the results of the empirical equations by Engelund and Hansen (1967) $\tau_{EH}$ and van Rijn (1984b) $\tau_{vR}$ and of the sum of $\tau'$ and $\tau''_d$ calculated considering the predictive models suggested by Van der Mark (2009) is shown in Figure 5.12 and is reported in Table 5.5. To quantify the deviation between the models, the percentage difference $Diff$ was calculated as follows (for instance considering $\tau_{EH}$ value):

$$Diff = \frac{|(\tau_{EH} - (\tau' + \tau''_d))|}{(\tau_{EH} + (\tau' + \tau''_d))/2} \tag{5.25}$$

For all the MB experiments, the data exhibit good agreement, particularly with the results obtained from the model proposed by Engelund and Hansen (1967) with a percentage difference between the two estimates lower than 20%. It is noticeable that the model by van Rijn (1984b) appears to be more sensitive to the presence of vegetation. In fact, only bare bed scenario demonstrates nearly perfect agreement, while the other setups deviate from the identity line as the frontal area of plants increases. However, based on this comparison and the validation of $\tau'$, it can be asserted that the estimates of $\tau''_d$ can be considered reliable.

After the validation, all the components of the bed shear stress predicted using the models presented in Chapter 5.2.1, were summed according to the linear superposition principle (Equation 5.4). This sum ($\tau_{sum}$) was then compared with the total bed shear stress estimated using the corrected depth-slope product (Equation 5.15). The comparison aimed to assess the validity of the linear superposition principle in predicting the total bed shear stress.

Figure 5.13 provides a summary of the results obtained from the MB experiments. The comparison highlights that, in setups characterized by the absence of leaves, the linear superposition principle appears to be valid, as there is a close agreement between the estimated and actual total bed shear stress values. However, when leaves are present, it is reasonable to hypothesize that a deviation from linearity occurs in the combined contribution of bedforms and vegetation to the overall total stress. This suggests that the presence of leaves may introduce non-linear effects that affect the interaction between bedforms and vegetation, potentially altering the validity of the linear superposition principle.

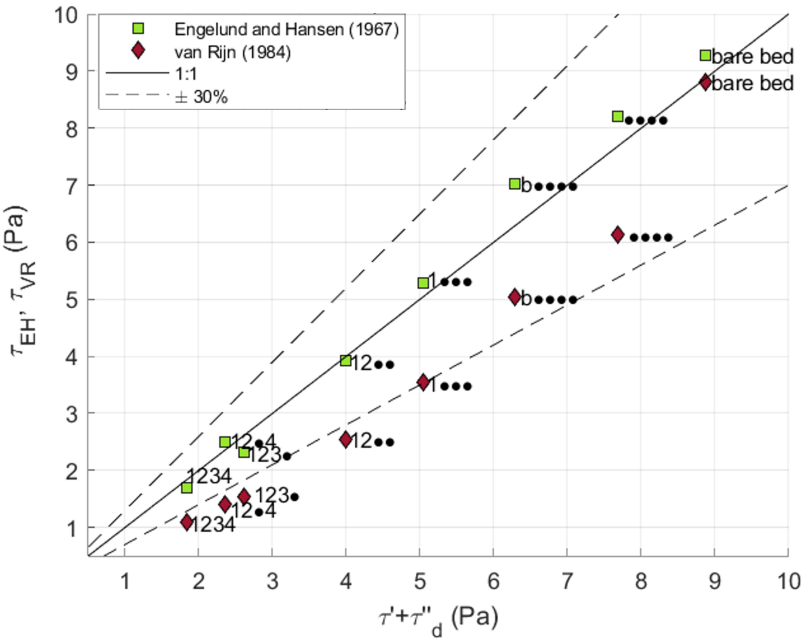


Figure 5.12: Comparison between the results of the empirical equations and $\tau'$ and $\tau''_d$ from models suggested by Van der Mark (2009) for MB experiments.

### 5.3.2 Fixed-bed Experiments for Direct Measurements of Hydraulic Forces (HF)

Following the same methodology used in the analysis of the MB experiments, the selected predictive models presented in Chapter 5.2.1 were used to estimate the values of skin friction and form drag for the HF experiments. The predicted values were then summed up to calculate the total bed shear stress, denoted as $\tau_{sum}$. Since the fixed dunes model was not covered by sand but by a layer of mortar cement, the skin friction was estimated considering the roughness of the mortar cement using a Manning coefficient $n = 0.015 s/m^{1/3}$, as reported in Chow (1959). The observed total bed shear stress, denoted as $\tau_b$, was estimated using the uniform-corrected depth-slope product (Equation 5.15). A comparison between the measured and predicted total bed shear stress values reveals that the measured values consistently exceed the predicted values by a

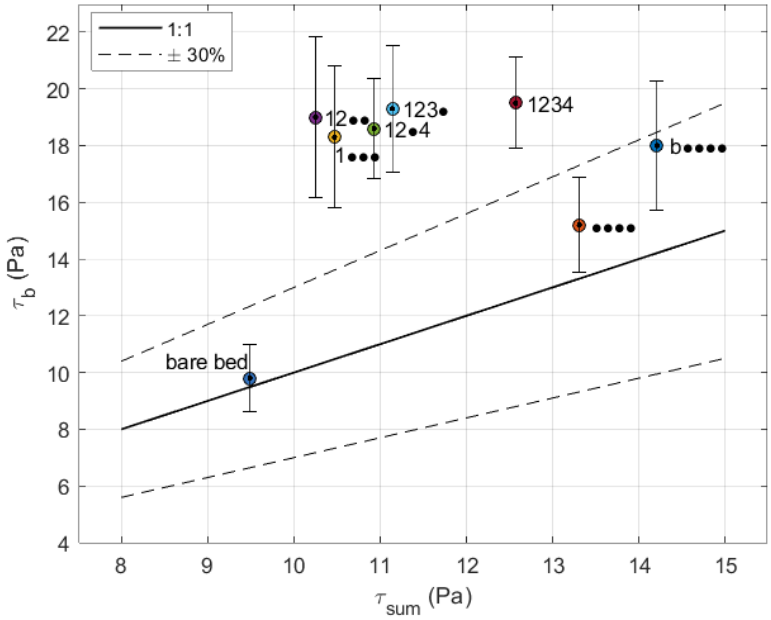


Figure 5.13: Linear superposition principle validation for MB experiments: comparison of total bed shear stress $\tau_b$ estimated as depth-slope product and the sum of the components of flow resistance $\tau_{sum}$; the vertical bars represent the uncertainty related to the estimation of the water depth and the water surface slope.

factor of 2÷3.5, as indicated in Table 5.6.

Concerning the form drag related to the dunes, it is noteworthy that the predicted values of $c''_{f,d}$ obtained from the formulation proposed by Yalin (1964) and Engelund (1966), ranging between 0.0075 and 0.0069, exhibit magnitudes that are one or two orders of magnitude smaller than the derived $c''_{SP}$ values obtained by linear regression of the SP measurements ($\tau_{SP}$) (reported in Table 5.7). The values of $\tau_{SP}/\rho$ were plotted against the squared mean velocity and the $c''_{SP}$ values values were inferred from the slope of the fitting lines, $\tau_{SP}/\rho = c''_{SP}U^2$, which are shown in Figure 5.14a. In this context, $c''_{SP}$ is assumed to represent the form drag due to the dunes, considering that the contribution of skin friction is negligible.

The discrepancy between the predicted $c''_{f,d}$ and inferred $c''_{SP}$ values is

Table 5.5: MB experiment results in terms of flow resistance components.

| Setup | $\tau'_*$ (-) | $\tau'$ (Pa) | $\tau''_d$ (Pa) | $Diff$(EH) (%) | $Diff$(vR) (%) | $\tau''_v$ (Pa) | $\tau_{sum}$ (Pa) | $\tau_b$ (Pa) | Diff($\tau_b$) (%) |
|---|---|---|---|---|---|---|---|---|---|
| 1234 | 0.082 | 1.11 | 0.94 | 10 | 58 | 10.73 | 12.79 | 19.55 | 42 |
| 123• | 0.088 | 1.20 | 1.64 | 3 | 56 | 8.30 | 11.14 | 19.29 | 54 |
| 12•4 | 0.090 | 1.23 | 1.34 | 13 | 55 | 8.36 | 10.93 | 18.61 | 52 |
| 12•• | 0.114 | 1.55 | 2.72 | 13 | 48 | 5.98 | 10.25 | 19.03 | 60 |
| 1••• | 0.146 | 1.99 | 3.40 | 1 | 39 | 5.08 | 10.47 | 18.34 | 55 |
| b•••• | 0.200 | 2.73 | 4.02 | 8 | 28 | 7.46 | 14.21 | 17.96 | 13 |
| •••• | 0.244 | 3.33 | 4.89 | 16 | 27 | 5.10 | 13.31 | 15.22 | 23 |
| bare bed | 0.289 | 3.95 | 5.52 | 19 | 10 | 0.00 | 9.47 | 9.81 | 4 |

significant and can potentially be attributed to the 3D geometry of the fixed dunes used in the experimental setup. The influence of 3D bedforms on bed resistance is a topic of conflicting findings in the literature, as the planimetric pattern of the bedforms can result in either an increase or a decrease in bed resistance. This discrepancy may arise from the significant role played by the shape of the crestline in determining the resulting bed shear stress (Venditti, 2007). Therefore, the observed deviation between the predicted and measured values can be attributed to the limitations of existing models in accurately estimating the form drag associated with the 3D geometry of the dunes.

Furthermore, the measured vegetative drag $\tau_{DFS}$ was compared with the estimated values using the Järvelä (2004) model, as illustrated in Figure 5.14b. The comparison reveals a generally good agreement between the estimated and measured vegetative drag, with all data points falling within a 30% deviation from the agreement line. These findings indicate that the Järvelä (2004) model provides satisfactory estimations of vegetative drag, demonstrating its effectiveness. However, it is important to note a significant deviation observed in the case of the plant configuration 12••, where the difference between the estimated and measured vegetative drag reaches 40%. This deviation can potentially be attributed to the combined presence of vegetation with a complex morphology, such as in the 12•• configuration, along with the presence of dunes in this specific setup. It is worth noting that the Järvelä (2004) formulation was derived under plane bed conditions, and the presence of dunes can alter the flow

Table 5.6: Measured and estimated bed shear stress contributions for HF experiments.

| Setup | $\tau_{SP}$ (Pa) | $\tau_{DFS}$ (Pa) | $\tau'$ (Pa) | $\tau''_d$ (Pa) | $\tau''_v$ (Pa) | ${}^a\tau_{sum}$ (Pa) | $Diff(\tau''_v)$ (%) | $(\tau_{DFS}+\tau_{SP})/\tau_{sum}$ (-) |
|---|---|---|---|---|---|---|---|---|
| 1234 | 4.35 | 3.71 | 0.06 | 0.11 | 3.37 | 3.54 | 10 | 2.27 |
| 1234 | 5.02 | 4.91 | 0.09 | 0.16 | 4.20 | 4.45 | 16 | 2.23 |
| 1234 | 6.55 | 6.04 | 0.13 | 0.23 | 5.15 | 5.51 | 16 | 2.29 |
| 1234 | 7.65 | 7.40 | 0.18 | 0.32 | 6.30 | 6.80 | 16 | 2.21 |
| 12•4 | 4.63 | 3.97 | 0.10 | 0.18 | 3.53 | 3.82 | 12 | 2.25 |
| 12•4 | 5.89 | 4.87 | 0.15 | 0.26 | 4.26 | 4.68 | 13 | 2.30 |
| 12•4 | 7.18 | 5.53 | 0.19 | 0.33 | 4.88 | 5.40 | 13 | 2.35 |
| 12•4 | 8.89 | 6.59 | 0.25 | 0.45 | 5.70 | 6.41 | 14 | 2.42 |
| 12•• | 5.21 | 2.72 | 0.18 | 0.32 | 2.44 | 2.94 | 11 | 2.70 |
| 12•• | 6.23 | 4.07 | 0.26 | 0.46 | 3.11 | 3.84 | 27 | 2.68 |
| 12•• | 9.12 | 5.03 | 0.35 | 0.61 | 3.71 | 4.67 | 30 | 3.03 |
| 12•• | 10.04 | 6.61 | 0.46 | 0.80 | 4.39 | 5.65 | 40 | 2.95 |
| •••• | 4.89 | 1.04 | 0.45 | 0.78 | 1.29 | 2.53 | -22 | 2.35 |
| •••• | 5.48 | 1.28 | 0.55 | 0.96 | 1.51 | 3.02 | -17 | 2.24 |
| •••• | 7.01 | 1.61 | 0.72 | 1.26 | 1.89 | 3.87 | -16 | 2.23 |
| •••• | 9.57 | 1.82 | 0.89 | 1.57 | 2.24 | 4.70 | -21 | 2.42 |
| bare bed | 5.97 | 0.00 | 0.61 | 1.11 | - | 1.72 | - | 3.47 |
| bare bed | 6.75 | 0.00 | 0.89 | 1.65 | - | 2.54 | - | 2.65 |
| bare bed | 8.30 | 0.00 | 0.95 | 1.72 | - | 2.67 | - | 3.11 |
| bare bed | 11.41 | 0.00 | 1.24 | 2.24 | - | 3.47 | - | 3.28 |

*a*: $\tau_{sum}$ represent the sum of the predicted values by means of the predictive models of Section 5.2.1.

characteristics, leading to deviations between the measured and estimated vegetative drag specifically for this configuration.

The validity of the linear superposition principle was proved by conducting a comparison between the estimated total bed shear stress $\tau_b$, calculated using the depth-slope product (Equation 5.15), and the sum of the measurements obtained from the shear plate and drag force sensors $\tau_{SP}+\tau_{DFS}$. For the analysis, the SP measurements were assumed to represent the combined contribution of bed skin friction and form drag due to the dune, and thus, the value of $\tau_{SP}+\tau_{DFS}$ was compared with $\tau_b$. Figure 5.15 and Table 5.8 illustrate this comparison, revealing that the measured values align within a 30% difference from the estimated total bed shear stress for leafless setups only. Notably, as the complexity of the plant morphology increases, the deviation between the measured and predicted bed shear stress also increases. The most significant deviation

Table 5.7: Resistance coefficient $c''_{SP}$.

| Setup | $c''_{SP}$ |
|---|---|
| 1234 | 0.2132 |
| 12•4 | 0.1648 |
| 12•• | 0.1057 |
| •••• | 0.0453 |
| bare bed | 0.0394 |

is observed in the 12•• setup, reaching a maximum of 44%. This observation may be attributed to the flow behavior occurring in the presence of the 12•• plant configuration. In this case, the flow is separated into two distinct layers. The upper layer, characterized by the presence of leaves, introduces additional flow resistance, slowing down the flow. Meanwhile, the lower layer experiences accelerated flow, resulting in an increased form drag exerted by the dunes.

## 5.4 Discussion

Particularly for the HF experiments, the composition of flow resistance in terms of bed shear stress was investigated by examining both the predictions from the selected models and the direct measures from SP and DFSs. The comparison is shown in Figure 5.16). A notable disparity is observed between the measured and predicted compositions of flow resistance. This significant contrast suggests that the primary hydraulic forces are predominantly associated with the form drag exerted by the dunes, rather than the contribution of vegetation as predicted by the models. These findings strongly suggest that the presence of vegetation plays a pivotal role in enhancing the resistance exerted by the bedforms.

Furthermore, the inferred $c''_{SP}$ values, reported in Table 5.7, were analyzed to investigate a potential correlation between the vegetation foliage stage and the form drag exerted by the bedforms. The values exhibit variations depending on the specific vegetation setups. The observations made, considering the same fixed bed morphology used in the experiments, suggest a strong correlation between the characteristics of the vegetation elements and the enhancement of bed shear stress induced by the dunes.

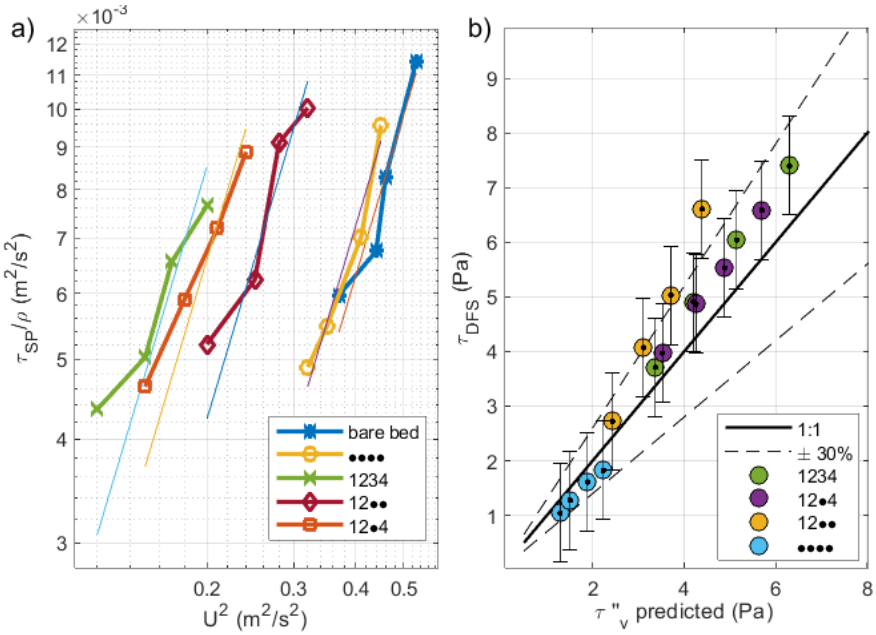


Figure 5.14: Measured form drag a) due to the dunes; b) due to the vegetation. The vertical error bars are related to the DFS uncertainty.

Remarkably, an increase in the frontal area of the vegetative elements corresponds to a concurrent increase in the value of $c''_{SP}$, indicating that the presence and distribution of leaf mass substantially amplifies the bed shear stress exerted by the dunes.

Additionally, when comparing the results obtained from the HF and MB experiments, a notable increase in the deviation between the measured and predicted total bed shear stress, denoted as $Diff(\tau_b)$, is observed (as shown in Table 5.5 and 5.6). Specifically, for the 12•• setup, the deviation increases from 40% in the HF case to 60% in the MB case. This significant difference suggests that the discrepancy observed in the MB experiments may be attributed to an additional resistance associated with the mobile bed condition.

It is important to note that this additional resistance can not be directly attributed to the sediment transport rate $Q_s$. This is evident from the fact that the deviation decreases while $Q_s$ increases. In particular,

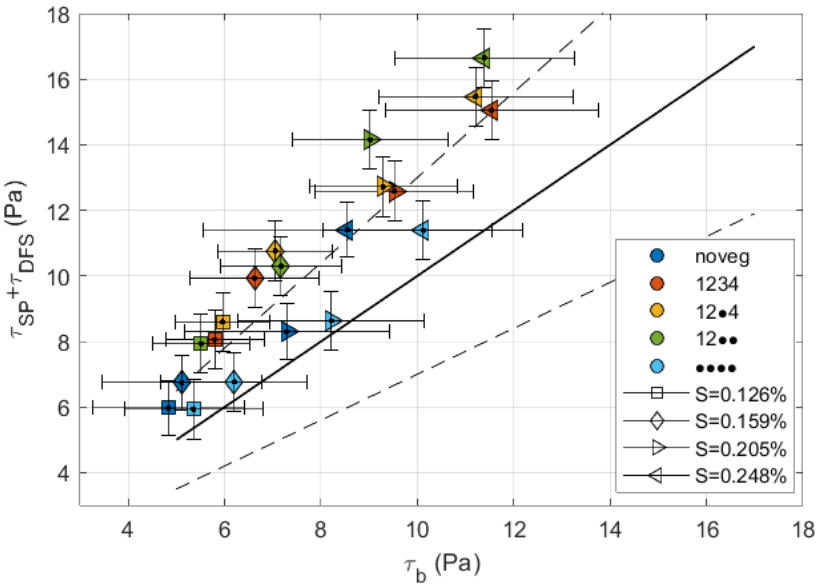


Figure 5.15: Comparison of observed $\tau_b$, estimated as depth-slope product, and the sum of measurements obtained from both SP and DFSs. The vertical error bars refer to the uncertainty related to the instruments, while the horizontal ones to the estimation of water depth and water surface slope.

a more uniform distribution of leaves along the plant stems, as in 1234 setup, results in a lower $Diff(\tau_b)$ in comparison with the 12•• setup, for both HF and MB cases. Thus, it is evident that the foliage distribution along the plant stem plays a crucial role in enhancing this extra resistance.

The analysis presented in this study reveals a clear relationship between the characteristics of vegetation elements and the bed shear stress exerted by the dunes. This finding aligns with the results reported by Duan and Al-Asadi (2022), who also observed an increase in form drag related to the dunes with an increase in vegetation density, modeled as rigid cylinders.

However, it is important to note that these results contrast with findings from other studies, such as Nepf (2012), López and García (1998) and Jordanova and James (2003), who claimed that the presence of vegetation reduces bed shear stress. It is worth mentioning that these observations

Table 5.8: Validation of the linear superposition principle for HF experiments.

| # | Setup | $\tau_{DFS} + \tau_{SP}$ (Pa) | $\tau_b$ (Pa) | $Diff(\tau_b)$ (%) |
|---|---|---|---|---|
| 1 | 1234 | 8.06 | 5.80 | 33 |
| 2 | 1234 | 9.93 | 6.62 | 40 |
| 3 | 1234 | 12.59 | 9.52 | 28 |
| 4 | 1234 | 15.05 | 11.54 | 26 |
| 5 | 12•4 | 8.60 | 5.96 | 36 |
| 6 | 12•4 | 10.76 | 7.05 | 42 |
| 7 | 12•4 | 12.72 | 9.29 | 31 |
| 8 | 12•4 | 15.47 | 11.21 | 32 |
| 9 | 12•• | 7.93 | 5.51 | 36 |
| 10 | 12•• | 10.30 | 7.17 | 36 |
| 11 | 12•• | 14.15 | 9.02 | 44 |
| 12 | 12•• | 16.65 | 11.39 | 37 |
| 13 | •••• | 5.93 | 5.35 | 10 |
| 14 | •••• | 6.77 | 6.20 | 9 |
| 15 | •••• | 8.63 | 8.21 | 5 |
| 16 | •••• | 11.39 | 10.12 | 12 |
| 17 | bare bed | 5.97 | 4.83 | 21 |
| 18 | bare bed | 6.75 | 5.11 | 28 |
| 19 | bare bed | 8.30 | 7.29 | 13 |
| 20 | bare bed | 11.41 | 8.55 | 29 |

may be more applicable in plane bed conditions and when dealing with rigid cylinders as vegetation elements. The complex interaction between dunes and vegetation with varying morphologies can lead to different outcomes, as demonstrated in this study.

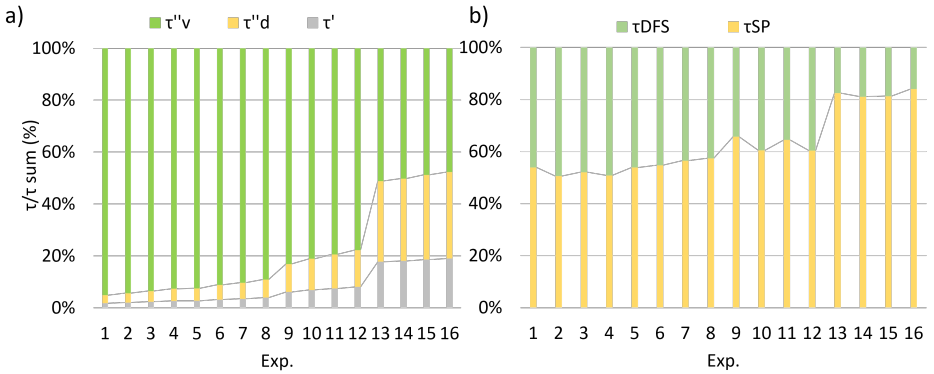


Figure 5.16: Composition of flow resistance components for HF experiments: a) according with the predictive models; b) contributions measured through the shear plate and drag force sensors.

## 5.5 Summary and Conclusions

In conclusion, this part of the thesis investigated the composition of flow resistance in the presence of leafy flexible vegetation and dune, in both mobile and fixed-bed conditions. The results highlight the significant influence of plant foliage stage on the control of total bed shear stress.

The analysis of the data collected from mobile-bed experiments revealed a deviation from the linear superposition principle in setups with leafy plants, while setups without vegetation or with leafless plants demonstrated better agreement. This suggests the introduction of non-linear effects in the combined contribution of leafy flexible plants and large-scale bedforms, potentially challenging the validity of the linear superposition principle.

Furthermore, the analysis of the measured hydraulic forces indicated that the morphology of plants, particularly the distribution of leaf mass along the plant stem, plays a crucial role in determining total bed shear stress. In particular, complex plant morphologies were found to enhance the form drag exerted by bedforms. The existing formulations for predicting bedform form drag might be inadequate when leafy flexible vegetation is present, as they do not account for the interconnected effects between plants and dunes. Direct measurements of total bed shear stress,

as sum of individual hydraulic forces associated with both dunes and plants, yielded values 2÷3.5 times higher than those predicted by existing methods. These findings suggest potential inaccuracies in parameterizing particularly bedform-related resistance, highlighting the importance of considering the combined effects of leafy vegetation and bedforms when estimating total bed shear stress.

It is noteworthy that the investigation of the applicability of the linear superposition principle revealed an interesting difference between the MB and HF experiments, particularly for vegetated setups. Specifically, in the MB experiments, a significant increase of approximately 20% in the deviation between the predicted and observed total bed shear stress was observed compared to the same plant configuration of the HF experiments. This significant difference suggests that the discrepancy may be attributed to an additional resistance associated with the mobile bed condition. However, it is important to note that the deviation observed in the MB experiments, depends to predicted values obtained from existing models whose validity remains uncertain in the current study.

Furthermore, the study exposes the limitations of current predictive models, which fail to account for the interconnected linkages between vegetation and bedforms. This results in an underestimation of the form drag associated with bedforms, as evidenced by the direct measurements. Additionally, existing models for predicting bedform form drag might be inadequate in presence the three-dimensionality of bedform geometry.

These findings highlight that the underlying physical processes governing flow in environments with flexible vegetation and large-scale bedforms remain inadequately understood. The limitations of current formulations in predicting bedform form drag in the presence of leafy vegetation might lead to potential failure of river restoration projects if these effects are not properly considered.

# Chapter 6

# Conclusions

Recalling the specific aims presented in Chapter 2, the results of this PhD research are here presented by answering to the specific research questions (RQ).

1. **How does leafy flexible vegetation impact sediment transport processes and the bedforms characteristics?**
   The analysis of the experimental data obtained from the mobile-bed experiments highlights the limitations of current models in accurately predicting sediment transport and bedform characteristics in scenarios with dunes covered by leafy flexible vegetation. By comparing the measured bed-load transport rates with predictive models based on bed shear stress, the study reveals that predictions are reliable, within a 30% error, for setups characterized by lower vegetation density (with $\langle a \rangle_z H < 0.08$). On the other hand, in the presence of leafy vegetation, the bed load transport rate deviates by approximately 80% from the predicted values using common bed-shear-stress-based models. This discrepancy suggests that the existing models fail to fully account for the complex interactions between dense vegetation and sediment transport, particularly in scenarios with leafy vegetation.

   Moreover, the data collected in the study provides valuable insights into the influence of vegetation on bedform characteristics. The presence of vegetation appears to result in a reduction in the average

dune wavelength, signifying a modification of the bedform geometry. Additionally, the study reveals that the celerity of the dunes can be influenced by the plant roughness density, displaying an increase with denser vegetation. Moreover, the measured celerity showed a good correlation with the observed sediment transport. These findings highlight the role of vegetation in shaping the dynamic behavior of the bedforms and consequently sediment transport.

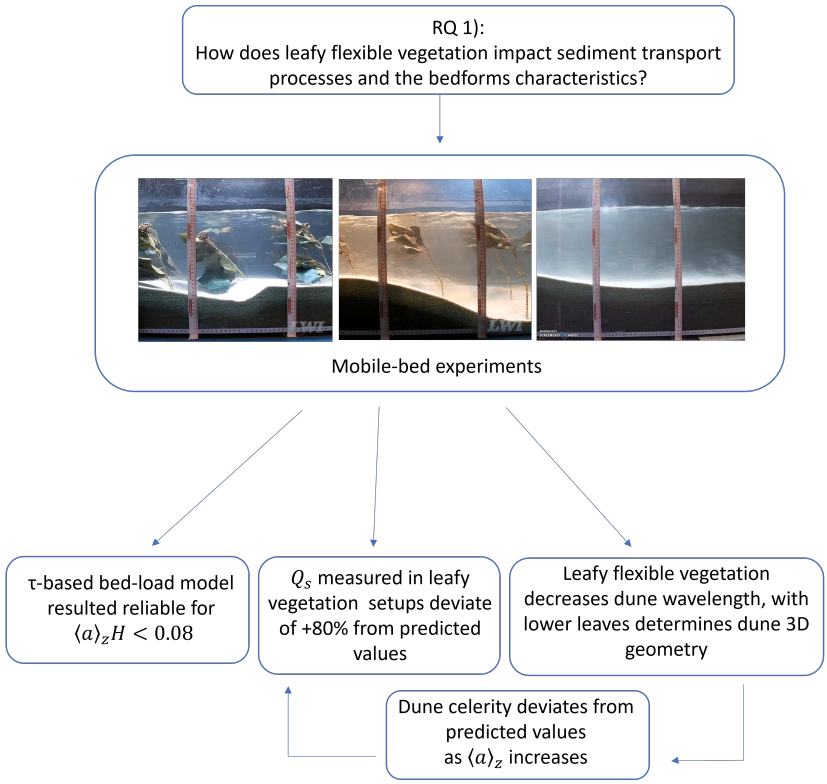


Figure 6.1: Summary of conclusion for RQ1.

2. **What is the combined influence of leafy flexible vegetation and bedforms on the flow field, considering both mobile and fixed bed conditions?**
   The interactions among vegetation, bedform geometry, and turbulent flow characteristics were examined through velocity measure-

ments under various conditions, including mobile and fixed beds, with and without the presence of leafy flexible vegetation.

The presence of vegetation was found to dampen the flow separation zone of dunes, thereby altering the scour and erosion patterns downstream of the dunes. This alteration may have important consequences for sediment transport dynamics in river environments.

The analysis of data collected from mobile-bed experiments revealed that spatially averaged turbulence intensity can be expressed as a function of bedform geometry, suggesting that bedform geometry plays a dominant role in controlling turbulence.

A novel comparison was conducted between fixed-bed and mobile-bed conditions, utilizing a digital elevation model (DEM) that accurately represents the topography resulted from mobile-bed experiments. This approach provided valuable insights into the impact of bed mobility on flow dynamics, revealing distinct differences in velocity profiles and turbulence intensity between the two conditions. In the fixed bed experiments, the double-averaged velocity profiles exhibited a noticeable acceleration at the elevation corresponding to the missing branches. This acceleration, however, was not observed in the velocity profiles resulted from the mobile bed experiments. Moreover, the mobile-bed experiments displayed turbulence intensity approximately $2 \div 3$ times higher than that of the fixed-bed experiments. These variations highlight the importance of taking into account the distinct flow dynamics associated with fixed-bed conditions, rather than mobile bed conditions, when studying and modeling river systems.

The application of the Xu and Nepf (2020) model to predict depth-averaged turbulent kinetic energy showed reasonable agreement for setups with low vegetation roughness density, but tended to overestimate it for denser vegetation setups. This discrepancy is likely due to the complex influence of leaves and their interconnections on sediment dynamics, bedform morphology, and consequently, flow field.

This study also identified limitations in existing turbulence-based

models for predicting bed-load transport rates in vegetated flows. Particularly, the Yang and Nepf (2018) model exhibits reasonable accuracy when applied to setups with low vegetation roughness density. However, when considering setups characterized by high vegetation roughness density ($C_D ah > 0.19$), the model tends to underestimate bed-load transport rates. This discrepancy can likely be attributed to the fact that the development of the original model primarily focused on rigid vegetation and small-scale ripples.

To address the limitations and extend the validity of the Yang and Nepf (2018) model, a modified model has been proposed. This modified model takes into account the influence of both leafy flexible vegetation and the presence of bedforms of turbulence field, aiming to improve the accuracy of predictions for sediment transport rates in vegetated flows. However, the model requires further validation and refinement using extensive experimental data to ensure its reliability and applicability across various environmental conditions.

Overall, these findings shed light on the importance of developing advanced models that comprehensively incorporate the combined influences of vegetation and mobile bedforms. Further research in this field will significantly enhance the understanding of the intricate involved dynamics and facilitate the development of more accurate models to predict bed load transport rates.

3. **What is the flow resistance composition in the presence of both vegetation and bedforms? The linear superposition principle is still valid?**
   The experimental data emphasizes the significant influence of the plant foliage stage on controlling the total bed shear stress. In fact, the study results demonstrate that the complexity of plant morphology has a direct influence on the form drag exerted by the bedforms. Specifically, when the plant morphology is more complex (i.e., with lower leaves missing), the form drag exerted by the dunes was found to be more enhanced. This indicates that the presence and arrangement of leaves on plant stem significantly affect the overall flow re-

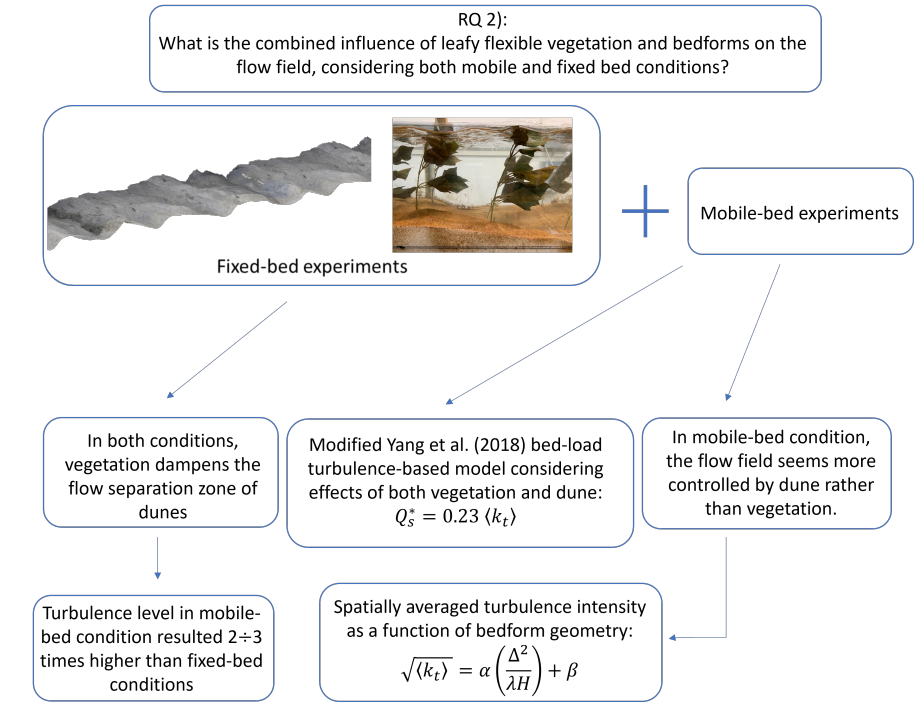


Figure 6.2: Summary of conclusion for RQ2.

sistance and bed shear stress in environments with vegetation and dunes. Furthermore, the predicted composition of flow resistance, based on the existing models, differed from the actual measurements, conducted in fixed-bed conditions. When estimating the total bed shear stress by summing the individual hydraulic forces associated with both dunes and plants, the measured values were found to be 2-3.5 times higher than the predictions made by the predictive methods. According to the measured data, the primary hydraulic forces are predominantly associated with the form drag exerted by the dunes rather than the contribution of vegetation, as predicted by the models. On the other hand, no significant difference was found between the measured and predicted form drag due to vegetation. This implies that the predictive models used in this study were able to accurately capture the overall influence of vegetation

on form drag, even in the presence of dune bed.

The analysis of data collected from mobile-bed experiments revealed deviations from the linear superposition principle in setups with leafy plants. On the other hand, setups without vegetation or with leafless plants showed better agreement, indicating the introduction of non-linear effects in the presence of leafy vegetation. The complexity of plant morphology further enhanced the deviation from the validity of the linear superposition principle. Similar conclusions can be drawn from direct measurements of the hydraulic forces in fixed-bed conditions. Notably, the deviation from the linear superposition principle is 20% higher in mobile-bed rather than fixed-bed conditions, considering the same plant configuration. The results strongly suggests that the presence of a mobile bed introduces additional effects that contribute to the observed deviation, where the presence and arrangement of leaves on plants significantly contribute to enhancing the bed shear stress, specifically the form drag related to the dunes.

The observed potential inaccuracies in parameterizing vegetation and bedform-related resistance highlight the need for comprehensive consideration of the combined effects of leafy vegetation and bedforms when estimating total bed shear stress. These findings highlight the importance of incorporating the influence of plant morphology and leaf arrangement into predictive models for flow resistance.

## 6.1 Limitation of the Results and Outlook

The findings and conclusions presented in this study are subject to limitations that should be acknowledged. The specific hydraulic conditions investigated in this research may not capture the full range of complexities associated with flow, vegetation, and sediment transport in natural environments. Variations in vegetation characteristics, such as type, foliage configuration, relative submergence, density, and spatial distribution, can significantly influence the dynamics of flow and sediment transport. Therefore, caution should be exercised when generalizing the results pre-

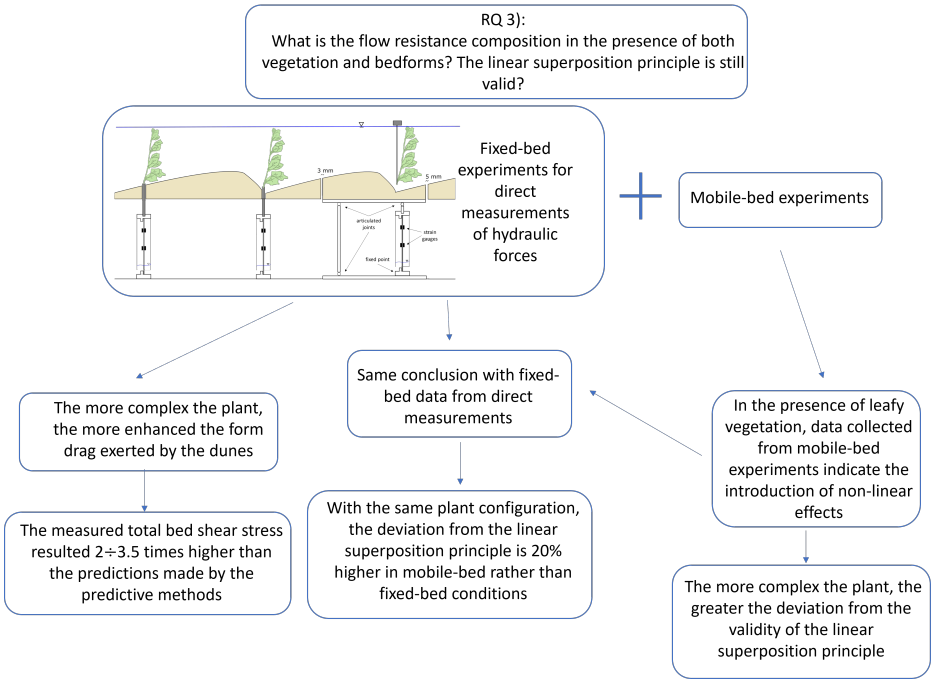


Figure 6.3: Summary of conclusion for RQ3.

sented herein to different conditions.

Future researches should address these limitations by conducting investigations across a wider range of relative submergence and canopy densities. Such studies might investigate also the presence of roots, that in this thesis work are considered to have a negligible impact on sediment transport and flow resistance. To further validate and generalize the conclusions of this study, additional works considering different hydraulic conditions beyond those examined in this research would be necessary. Expanding the investigation will provide a more detailed understanding of the complex interactions between vegetation, bedforms, and flow dynamics, ultimately contributing to improved predictive models.

Furthermore, future research efforts should focus on characterizing turbulence characteristics of flow over dunes in the presence of vegetation. Moreover, given the scarcity of studies on mobile bed conditions with real-like vegetation, conducting research in these configurations will yield

valuable insights into the complex interactions among flow dynamics, vegetation characteristics, and sediment processes.

Indeed, exploring the concept of linear superposition in relation to turbulent kinetic energy in scenarios where leafy flexible vegetation coexists with bedforms holds great potential for gaining deeper insights into the complex interactions among flow dynamics, turbulent energy transfer, and the combined effects of vegetation and bedforms on flow resistance and sediment transport.

Investigating these scenarios will provide valuable information on how vegetation influences turbulent energy dissipation and redistribution over bedforms, which, in turn, affects flow resistance and sediment transport. Understanding the interplay between turbulence, vegetation, and bedforms will contribute to the development of more accurate and reliable predictive models for sediment transport in natural environments with diverse vegetation and bedform configurations.

Such research efforts will be crucial in advancing our knowledge of flow processes in these complex environments and will have important implications for river management and restoration projects.

# Appendix A

## A.1 Side-wall correction

This method considers narrow channels as $B/H < 5$ (B is the width of the free surface, and H the water depth). It must be applied when the bed roughness (sediment) is higher than the wall roughness (glass or Plexiglas). This mirrors in increased shear stress at the bottom and decreased at the wall. The walls closeness affects the bed shear stress amount.The method proposed by Vanoni and Brooks (1957) provides a separation of the shear stress related to the bed and walls.

Hypothesis:

1. The wetted area can be divided in the sub-area concerning to the bed $A_b$ and on the walls $A_w$. Boundaries between bed and wall sections are considered zero shear surfaces.

2. The mean flow velocity U is the same both on $A_b$ and $A_w$.

3. The energy slope S is is the same both on $A_b$ and $A_w$.

Procedure:
Using Darcy-Weisbach relationship for each sub-area:

$$f_b = \frac{8gR_bS}{U^2}; f_w = \frac{8gR_wS}{U^2}; f = \frac{8gRS}{U^2} \tag{A.1}$$

With $P = P_b + P_w$

Considering hypothesis 2 and 3:

$$\frac{U^2}{S} = \frac{8gA}{fP} = \frac{8gA_b}{f_b P_b} = \frac{8gA_w}{f_w P_w} \tag{A.2}$$

With $A = A_b + A_w$ so should be $Pf = P_b f_b + P_w f_w$

And consequently

$$f_b = \frac{Pf}{P_b} - \frac{P_w f_w}{P_b} \tag{A.3}$$

Knowing the geometry of the section ($P$, $P_w$ , $P_b$), $f_b$ can be estimate with

f (from experimental data = Q, h, S, geometry) and $f_w$ :

Defining Reynolds number for each area:

$$Re_b = \frac{4R_b U}{\nu}; Re_w = \frac{4R_w U}{\nu}; Re = \frac{4RU}{\nu} \tag{A.4}$$

Plugging the hydraulic radius from Equation (A.1) and substituting in Equation (A.4):

$$\frac{Re_b}{f_b} = \frac{Re_w}{f_w} = \frac{Re}{f}$$

Re f can be estimate with experimental data Q, h, S, section geometry.

$f_w$ is estimated with Prandtl-Von Karman formula that is valid for hydraulic smooth wall:

$$\frac{1}{\sqrt{f_w}} = -2\log\left(\frac{2.51}{\frac{Re}{f} f_w^{\frac{3}{2}}}\right)$$

That can be solved by trial and error. Or it can be solved considering the explicit form reported in Cheng (2011).

Finally the whole procedure can be summarise in:

1. Evaluate Re and f from the experimental data, there is a graph of f vs Re/f. so $\frac{Re}{f} = \frac{Re_w}{f_w}$
2. Evaluate
$$f_w = \frac{1}{\sqrt{f_w}} = -2\log\left(\frac{2.51}{\frac{Re}{f} f_w^{\frac{3}{2}}}\right) \tag{A.5}$$
3. Estimate $f_b = \frac{Pf}{P_b} - \frac{P_w f_w}{P_b}$

4. Estimate $R_b$ from $f_b = \frac{8gR_bS}{U^2}$
5. $u*_b = \sqrt{gR_bS}$
6. $\tau_b = \rho u*_b^2$

# Appendix B

# Publications

This research activity has led to several contributions in international conferences and articles, that are either submitted or in preparation for submission.

### International Journals

1. **Artini, Giada**, Francalanci, S., Solari, L., and Aberle J. Effects of Leafy Flexible Vegetation on Bed-Load Transport and Dune Geometry, *submitted*

2. **Artini, Giada**, Francalanci, S., Solari, L., and Aberle J. Effects of Leafy Flexible Just-submerged Vegetation and Dunes on Flow Field, *to be submitted*

3. **Artini, Giada**, Francalanci, S., Solari, L., and Aberle J. Flow Resistance Decomposition in Vegetated Channels with Dunes, *to be submitted*

### International Conferences

1. **Artini, Giada**, Aberle, J., Francalanci, S. and Solari., L. Influence of vegetation and large-scale bed forms on sediment transport. *Symposium on River, Coastal and Estuarine Morphodynamics (RCEM 2023)*. Urbana, IL (USA). Oral presentation.

2. **Artini, Giada**, Francalanci, S., Solari, L. and Aberle, J. Influence Of Leafy Flexible Vegetation On 3d Dunes Geometry, in *International Conference on Fluvial Sedimentology (ICFS 2023)*, Riva del Garda, Italy. Oral presentation.

3. **Artini, Giada**, Francalanci, S., Solari, L. and Aberle, J. Influence of flexible leafy vegetation on sediment transport and morphodynamics: does the linear superposition principle work?, in *Yalin Memorial Colloquium (YMC 2023)*, Palermo (Italy), 2023. Oral presentation.

4. **Artini, Giada**, Aberle, J., Francalanci, S. and Solari, L. Flow resistance in open channels with leafed flexible vegetation and large-scale bedforms in *River Flow, 2022*, online. Oral presentation.

# Bibliography


Aberle, J., Coleman, S. E., and Nikora, V. I. (2012). Bed load transport by bed form migration. *Acta Geophysica*, 60(6):1720–1743.

Aberle, J. and Järvelä, J. (2013). Flow resistance of emergent rigid and flexible floodplain vegetation. *Journal of Hydraulic Research*, 51(1):33–45.

Aberle, J. and Järvelä, J. (2015). *Hydrodynamics of vegetated channels*, chapter in: Rowiński, P., Radecki-Pawlik, A. (eds) *Rivers-physical, fluvial and environmental processes*, pages 519–541. GeoPlanet: Earth and Planetary Sciences, Springer, Berlin, Springer.

Aberle, J., Koll, K., and Dittrich, A. (2008). Form induced stresses over rough gravel-beds. *Acta Geophysica*, 56:584–600.

Aberle, J., Schoneboom, T., and Rhiner, B. (2011). Influence of leaf mass on drag forces in vegetated flows. In *Proceedings of the 34th World Congress of the International Association for Hydro-Environment Research and Engineering: Hydrology and Water Resources Symposium and Conference on Hydraulics in Water Engineering*, pages 2744–2751. Engineers Australia Barton, ACT.

Afzalimehr, H. (2010). Effect of non-uniformity of flow on velocity and turbulence intensities over a cobble-bed. *Hydrological Processes: An International Journal*, 24(3):331–341.

Afzalimehr, H. and Anctil, F. (2000). Accelerating shear velocity in gravel-bed channels. *Hydrological sciences journal*, 45(1):113–124.

Afzalimehr, H., Maddahi, M. R., Sui, J., and Rahimpour, M. (2019). Impacts of vegetation over bedforms on flow characteristics in gravel-bed rivers. *Journal of Hydrodynamics*, 31:986–998.

Allen, J. (1968). *Current Ripples: Their Relation to Patterns of Water and Sediment Motion*. North-Holland Publishing Company.

Allen, J. (1985). Loose-boundary hydraulics and fluid mechanics: selected advances since 1961. *Geological Society, London, Special Publications*, 18(1):7–28.

Arcement, G. J. and Schneider, V. R. (1989). *Guide for selecting Manning's roughness coefficients for natural channels and flood plains*. US Government Printing Office Washington, DC.

Armanini, A. and Cavedon, V. (2019). Bed-load through emergent vegetation. *Advances in Water Resources*, 129:250–259.

Armanini, A., Righetti, M., and Grisenti, P. (2005). Direct measurement of vegetation resistance in prototype scale. *Journal of Hydraulic Research*, 43(5):481–487.

Artini, G. (2023). Side-view videos. Available at https://doi.org/10.5281/zenodo.7882869.

Baas, J. H. (1994). A flume study on the development and equilibrium morphology of current ripples in very fine sand. *Sedimentology*, 41(2):185–209.

Bagnold, R. A. (1973). The nature of saltation and of bed-load transport in water. *Proceedings of the Royal Society of London. A. Mathematical and Physical Sciences*, 332(1591):473–504.

Baptist, M., Babovic, V., Rodríguez Uthurburu, J., Keijzer, M., Uittenbogaard, R., Mynett, A., and Verwey, A. (2007). On inducing equations for vegetation resistance. *Journal of Hydraulic Research*, 45(4):435–450.

Baranya, S., Fleit, G., Muste, M., Tsubaki, R., and Józsa, J. (2023). Bedload estimation in large sand-bed rivers using acoustic mapping velocimetry (AMV). *Geomorphology*, 424:108562.

Bennett, S. and Best, J. (1995). Mean flow and turbulence structure over fixed, two-dimensional dunes: implications for sediment transport and bedform stability. *Sedimentology*, 42(3):491–513.

Best, J. (2005). The fluid dynamics of river dunes: A review and some future research directions. *Journal of Geophysical Research: Earth Surface*, 110(F4):F04S02.

Best, J. and Kostaschuk, R. (2002). An experimental study of turbulent flow over a low-angle dune. *Journal of Geophysical Research: Oceans*, 107(C9):18–1.

Beudin, A., Kalra, T. S., Ganju, N. K., and Warner, J. C. (2017). Development of a coupled wave-flow-vegetation interaction model. *Computers & Geosciences*, 100:76–86.

Bonilla-Porras, J. A., Armanini, A., and Crosato, A. (2021). Extended einstein's parameters to include vegetation in existing bedload predictors. *Advances in Water Resources*, 152:103928.

Box, W., Järvelä, J., and Västilä, K. (2021). Flow resistance of floodplain vegetation mixtures for modelling river flows. *Journal of Hydrology*, 601:126593.

Branß, T. and Aberle, J. (2022). Combined effect of a mobile bed and floodplain edge vegetation on compound channel conveyance. *Journal of Hydraulic Research*, 60(5):826–834.

Branß, T., Núñez-González, F., and Aberle, J. (2022). Fluvial levees in compound channels: a review on formation processes and the impact of bedforms and vegetation. *Environmental Fluid Mechanics*, 22(2-3):559–585.

Bridge, J. S. and Best, J. L. (1988). Flow, sediment transport and bedform dynamics over the transition from dunes to upper-stage plane beds: implications for the formation of planar laminae. *Sedimentology*, 35(5):753–763.

Brown, C. B. (1950). Sediment transportation. *Engineering Hydraulics*, 12:769–857.

Brownlie, W. R. (1983). Flow depth in sand-bed channels. *Journal of Hydraulic Engineering*, 109(7):959–990.

Calvani, G., Carbonari, C., and Solari, L. (2022). Stability analysis of submerged vegetation patterns in rivers. *Water Resources Research*, 58(8):e2021WR031901.

Camporeale, C., Perucca, E., Ridolfi, L., and Gurnell, A. (2013). Modeling the interactions between river morphodynamics and riparian vegetation. *Reviews of Geophysics*, 51(3):379–414.

Cao, Z., Pender, G., and Meng, J. (2006). Explicit formulation of the shields diagram for incipient motion of sediment. *Journal of Hydraulic Engineering*, 132(10):1097–1099.

Caroppi, G., Västilä, K., Gualtieri, P., Järvelä, J., Giugni, M., and Rowiński, P. M. (2021). Comparison of flexible and rigid vegetation induced shear layers in partly vegetated channels. *Water Resources Research*, 57(3):e2020WR028243.

Caroppi, G., Västilä, K., Järvelä, J., Lee, C., Ji, U., Kim, H. S., and Kim, S. (2022). Flow and wake characteristics associated with riparian vegetation patches: Results from field-scale experiments. *Hydrological Processes*, 36(2):e14506.

Caroppi, G., Västilä, K., Järvelä, J., Rowiński, P. M., and Giugni, M. (2019). Turbulence at water-vegetation interface in open channel flow: Experiments with natural-like plants. *Advances in Water Resources*, 127:180–191.

Chanson, H., Trevethan, M., and Aoki, S.-i. (2008). Acoustic doppler velocimetry (adv) in small estuary: field experience and signal post-processing. *Flow Measurement and Instrumentation*, 19(5):307–313.

Chapman, J. A., Wilson, B. N., and Gulliver, J. S. (2015). Drag force parameters of rigid and flexible vegetal elements. *Water Resources Research*, 51(5):3292–3302.

Chen, S.-C., Chan, H.-C., and Li, Y.-H. (2012). Observations on flow and local scour around submerged flexible vegetation. *Advances in Water Resources*, 43:28–37.

Cheng, N.-S. (2011). Revisited vanoni-brooks sidewall correction. *International Journal of Sediment Research*, 26(4):524–528.

Chow, V. T. (1959). *Open Channel Hydraulics.* McGraw-Hill, New York.

Cilli, S., Billi, P., Schippa, L., Grottoli, E., and Ciavola, P. (2021). Bedload transport and dune bedforms characteristics in sand-bed rivers supplying a retreating beach of the northern Adriatic Sea (Italy). *Journal of Hydrology: Regional Studies*, 37:100894.

Coleman, S. E. and Melville, B. W. (1994). Bed-form development. *Journal of Hydraulic Engineering*, 120(5):544–560.

Coleman, S. E., Nikora, V. I., and Aberle, J. (2011). Interpretation of alluvial beds through bed-elevation distribution moments. *Water Resources Research*, 47(11):W11505.

Coles, D. (1956). The law of the wake in the turbulent boundary layer. *Journal of Fluid Mechanics*, 1(2):191–226.

Delecluyse, K., Troch, P., and Blanckaert, K. (2010). The effect of migrating dune forms on the flow field of an alluvial river. In *5th International conference*

*on Fluvial Hydraulics (River Flow 2010)*, pages 913–919. Bundesanstalt für Wasserbau.

Dey, S., Paul, P., Fang, H., and Padhi, E. (2020). Hydrodynamics of flow over two-dimensional dunes. *Physics of Fluids*, 32(2):025106.

Dietrich, W. E. (1982). Settling velocity of natural particles. *Water Resources Research*, 18(6):1615–1626.

D'Ippolito, A., Calomino, F., Dey, S., Gaudio, R., and Penna, N. (2023). Bedload transport through emergent vegetation: current status and its future prospect. *Environmental Fluid Mechanics*, 23:711–733.

Doroudian, B., Bagherimiyab, F., and Lemmin, U. (2010). Improving the accuracy of four-receiver acoustic doppler velocimeter (ADV) measurements in turbulent boundary layer flows. *Limnology and Oceanography: Methods*, 8(11):575–591.

Duan, J. G. and Al-Asadi, K. (2022). On bed form resistance and bed load transport in vegetated channels. *Water*, 14(23):3794.

Einstein, H. and Banks, R. (1950). Fluid resistance of composite roughness. *Eos, Transactions American Geophysical Union*, 31(4):603–610.

Einstein, H. A. (1950). The bed-load function for sediment transportation in open channel flows. Technical Report 1026, US Department of Agriculture.

Einstein, H. A. and Barbarossa, N. L. (1952). River channel roughness. *Transactions of the American Society of Civil Engineers*, 117(1):1121–1132.

Engelund, F. (1966). Hydraulic resistance of alluvial streams. *Journal of the Hydraulics Division*, 92(2):315–326.

Engelund, F. (1977). Hydraulic resistance for flow over dunes. Technical report, *Progress Report 44*, Institute for Hydrodynamic and Hydraulic Engineering, Tech. Univ. Denmark.

Engelund, F. and Fredsoe, J. (1982). Sediment ripples and dunes. *Annual Review of Fluid Mechanics*, 14(1):13–37.

Engelund, F. and Hansen, E. (1967). A monograph on sediment transport in alluvial streams. *Technical University of Denmark 0stervoldgade 10, Copenhagen K.*

European Commission and Directorate General for Environment (2000). *The EU Water Framework Directive (2000/60/EC)*. Publications Office.

Faranda, D., Dubrulle, B., Daviaud, F., and Pons, F. M. E. (2014). Probing turbulence intermittency via autoregressive moving-average models. *Physical Review E*, 90(6):061001.

Ferraro, D. and Dey, S. (2015). *Principles of mechanics of bedforms*, chapter in Rivers-Physical, Fluvial and Environmental Processes, pages 79–98. Springer.

Finnigan, J. J. and Shaw, R. H. (2008). Double-averaging methodology and its application to turbulent flow in and above vegetation canopies. *Acta Geophysica*, 56:534–561.

Follett, E. M. and Nepf, H. M. (2012). Sediment patterns near a model patch of reedy emergent vegetation. *Geomorphology*, 179:141–151.

Gao, P. and Abrahams, A. D. (2004). Bedload transport resistance in rough open-channel flows. *Earth Surface Processes and Landforms*, 29(4):423–435.

Ghisalberti, M. and Nepf, H. (2004). The limited growth of vegetated shear layers. *Water Resources Research*, 40(7).

Ghisalberti, M. and Nepf, H. (2006). The structure of the shear layer in flows over rigid and flexible canopies. *Environmental Fluid Mechanics*, 6:277–301.

Ghisalberti, M. and Nepf, H. (2009). Shallow flows over a permeable medium: the hydrodynamics of submerged aquatic canopies. *Transport in Porous Media*, 78:309–326.

Goring, D. G. and Nikora, V. I. (2002). Despiking acoustic doppler velocimeter data. *Journal of Hydraulic Engineering*, 128(1):117–126.

Guo, J. (2015). Sidewall and non-uniformity corrections for flume experiments. *Journal of Hydraulic Research*, 53(2):218–229.

Gurnell, A. (2014). Plants as river system engineers. *Earth Surface Processes and Landforms*, 39(1):4–25.

Guy, H. P., Simons, D. B., and Richardson, E. V. (1966). Sediment transport in alluvial channels, 1963-65. Technical report, U.S. Geological Survey *Professional Paper 462-I*.

Hanmaiahgari, P. R. and Balachandar, R. (2016). Turbulence characteristics of open channel flow over non-equilibrium 3-d mobile dunes. *Sādhanā*, 41:1019–1037.

Hejazi, K., Falconer, R. A., and Seifi, E. (2016). Denoising and despiking adv velocity and salinity concentration data in turbulent stratified flows. *Flow Measurement and Instrumentation*, 52:83–91.

Heydari, H., Zarrati, A., and Karimaee Tabarestani, M. (2014). Bed form characteristics in a live bed alluvial channel. *Scientia Iranica*, 21(6):1773–1780.

Hofland, B. and Battjes, J. A. (2006). Probability density function of instantaneous drag forces and shear stresses on a bed. *Journal of Hydraulic Engineering*, 132(11):1169–1175.

Hoppenreijs, J. H., Eckstein, R. L., and Lind, L. (2022). Pressures on boreal riparian vegetation: A literature review. *Frontiers in Ecology and Evolution*, 9:806130.

Hou, J., Zhang, C., Wang, D., Li, F., Yu, Z., and Zhou, Q. (2019). Fixed-bed and mobile-bed resistance of channels with steep gradients in mountainous areas. *Water*, 11(4):681.

Huai, W., Zhang, J., Katul, G. G., Cheng, Y.-g., Tang, X., and Wang, W.-j. (2019). The structure of turbulent flow through submerged flexible vegetation. *Journal of Hydrodynamics*, 31:274–292.

Huai, W.-x., Li, S., Katul, G. G., Liu, M.-y., and Yang, Z.-h. (2021). Flow dynamics and sediment transport in vegetated rivers: A review. *Journal of Hydrodynamics*, 33(3):400–420.

Huang, C., Qiao, F., and Ma, H. (2020). Noise reduction of acoustic doppler velocimeter data based on kalman filtering and autoregressive moving average models. *Acta Oceanologica Sinica*, 39:106–113.

Jalonen, J. and Järvelä, J. (2014). Estimation of drag forces caused by natural woody vegetation of different scales. *Journal of Hydrodynamics*, 26(4):608–623.

Jalonen, J., Järvelä, J., and Aberle, J. (2013). Leaf area index as vegetation density measure for hydraulic analyses. *Journal of Hydraulic Engineering*, 139(5):461–469.

Jalonen, J., Järvelä, J., Koivusalo, H., and Hyyppä, H. (2014). Deriving floodplain topography and vegetation characteristics for hydraulic engineering applications by means of terrestrial laser scanning. *Journal of Hydraulic Engineering*, 140(11):04014056.

Järvelä, J. (2004). Determination of flow resistance caused by non-submerged woody vegetation. *International Journal of River Basin Management*, 2(1):61–70.

Jordanova, A. A. and James, C. (2003). Experimental study of bed load transport through emergent vegetation. *Journal of Hydraulic Engineering*, 129(6):474–478.

Kabiri, F., Afzalimehr, H., and Sui, J. (2017). Flow structure over a wavy bed with vegetation cover. *International Journal of Sediment Research*, 32(2):186–194.

Kalman, R. E. et al. (1960). A new approach to linear filtering and prediction problems. *Journal of Basic Engineering*, 82(1):35–45.

Kouwen, N., Li, R.-M., and Simons, D. B. (1981). Flow resistance in vegetated waterways. *Transactions of the ASAE*, 24(3):684–0690.

Krick, J. and Sukhodolov, A. (2014). Turbulent flow over fast moving dunes: Improved method for studies in natural streams. In *Proceedings of the International Conference on Fluvial Hydraulics, River Flow 2014*, pages 321–326.

Lai, C. C. and Socolofsky, S. A. (2018). Evaluation of linear autoregressive models for estimation of energy spectra in gappy turbulent velocity data. *Limnology and Oceanography: Methods*, 16(1):1–21.

Le Bouteiller, C. and Venditti, J. (2015). Sediment transport and shear stress partitioning in a vegetated flow. *Water Resources Research*, 51(4):2901–2922.

Le Bouteiller, C. and Venditti, J. G. (2014). Vegetation-driven morphodynamic adjustments of a sand bed. *Geophysical Research Letters*, 41(11):3876–3883.

Leary, K. C. and Buscombe, D. (2020). Estimating sand bed load in rivers by tracking dunes: a comparison of methods based on bed elevation time series. *Earth Surface Dynamics*, 8(1):161–172.

Lei, J. and Nepf, H. (2021). Evolution of flow velocity from the leading edge of 2-d and 3-d submerged canopies. *Journal of Fluid Mechanics*, 916:A36.

Lightbody, A. and Nepf, H. (2006). Prediction of near-field shear dispersion in an emergent canopy with heterogeneous morphology. *Environmental Fluid Mechanics*, 6:477–488.

Lightbody, A. F., Kui, L., Stella, J. C., Skorko, K. W., Bywater-Reyes, S., and Wilcox, A. C. (2019). Riparian vegetation and sediment supply regulate the morphodynamic response of an experimental stream to floods. *Frontiers in Environmental Science*, 7:40.

Lin, M. C.-Y. and Venditti, J. G. (2013). An empirical model of subcritical bedform migration. *Sedimentology*, 60(7):1786–1799.

Lisimenka, A. and Kubicki, A. (2017). Estimation of dimensions and orientation of multiple riverine dune generations using spectral moments. *Geo-Marine Letters*, 37:59–74.

Liu, C. and Nepf, H. (2016). Sediment deposition within and around a finite patch of model vegetation over a range of channel velocity. *Water Resources Research*, 52(1):600–612.

Lokin, L., Warmink, J., Bomers, A., and Hulscher, S. (2022). River dune dynamics during low flows. *Geophysical research letters*, 49(8):e2021GL097127.

López, F. and García, M. (1998). Open-channel flow through simulated vegetation: Suspended sediment transport modeling. *Water Resources Research*, 34(9):2341–2352.

Lyn, D. (1993). Turbulence measurements in open-channel flows over artificial bed forms. *Journal of Hydraulic Engineering*, 119(3):306–326.

Maddux, T., McLean, S., and Nelson, J. (2003a). Turbulent flow over three-dimensional dunes: 2. fluid and bed stresses. *Journal of Geophysical Research: Earth Surface*, 108(F1):6010.

Maddux, T., Nelson, J., and McLean, S. (2003b). Turbulent flow over three-dimensional dunes: 1. free surface and flow response. *Journal of Geophysical Research: Earth Surface*, 108(F1):6009.

Martin, V., Fisher, T., Millar, R., and Quick, M. (2002). ADV data analysis for turbulent flows: Low correlation problem. In *in Proceedings Hydraulic Measurements and Experimental Methods*, pages 1–10.

Maza, M., Adler, K., Ramos, D., Garcia, A. M., and Nepf, H. (2017). Velocity and drag evolution from the leading edge of a model mangrove forest. *Journal of Geophysical Research: Oceans*, 122(11):9144–9159.

McLean, S., Nelson, J., and Wolfe, S. (1994). Turbulence structure over two-dimensional bed forms: Implications for sediment transport. *Journal of Geophysical Research: Oceans*, 99(C6):12729–12747.

McLean, S. and Nikora, V. (2006). Characteristics of turbulent unidirectional flow over rough beds: Double-averaging perspective with particular focus on sand dunes and gravel beds. *Water resources research*, 42(10):W10409.

McLean, S., Wolfe, S., and Nelson, J. (1999). Predicting boundary shear stress and sediment transport over bed forms. *Journal of Hydraulic Engineering*, 125(7):725–736.

McLean, S. R., Nikora, V. I., and Coleman, S. E. (2008). Double-averaged velocity profiles over fixed dune shapes. *Acta Geophysica*, 56:669–697.

McLelland, S. J. and Nicholas, A. P. (2000). A new method for evaluating errors in high-frequency adv measurements. *Hydrological Processes*, 14(2):351–366.

Mendoza, C. and Wen Shen, H. (1990). Investigation of turbulent flow over dunes. *Journal of Hydraulic Engineering*, 116(4):459–477.

Meyer-Peter, E. and Müller, R. (1948). Formulas for bed-load transport. In *IAHSR 2nd meeting, Stockholm, appendix 2*. IAHR.

Moore, B. (2012). Kalman Filter Package, https://www.mathworks.com/matlabcentral/ fileexchange/38302-kalman-filter-package (accessed: 08.01.2023).

Morgan, J. A., Brogan, D. J., and Nelson, P. A. (2017). Application of structure-from-motion photogrammetry in laboratory flumes. *Geomorphology*, 276:125–143.

Muste, M., Lyn, D. A., Admiraal, D., Ettema, R., Nikora, V., and García, M. H. (2017). *Experimental Hydraulics: Methods, Instrumentation, Data Processing and Management: Volume I: Fundamentals and Methods*. CRC Press.

Naqshband, S. (2014). *Morphodynamics of river dunes: suspended sediment transport along mobile dunes and dune development towards upper stage plane bed*. PhD thesis, University of Twente, Netherlands.

Naqshband, S., Hoitink, A., McElroy, B., Hurther, D., and Hulscher, S. J. (2017). A sharp view on river dune transition to upper stage plane bed. *Geophysical Research Letters*, 44(22):11–437.

Naqshband, S., Ribberink, J. S., and Hulscher, S. J. (2014). Using both free surface effect and sediment transport mode parameters in defining the morphology of river dunes and their evolution to upper stage plane beds. *Journal of Hydraulic Engineering*, 140(6):06014010.

Nelson, J. M., Shreve, R. L., McLean, S. R., and Drake, T. G. (1995). Role of near-bed turbulence structure in bed load transport and bed form mechanics. *Water Resources Research*, 31(8):2071–2086.

Nepf, H., Ghisalberti, M., White, B., and Murphy, E. (2007). Retention time and dispersion associated with submerged aquatic canopies. *Water Resources Research*, 43(4):W04422.

Nepf, H. M. (1999). Drag, turbulence, and diffusion in flow through emergent vegetation. *Water Resources Research*, 35(2):479–489.

Nepf, H. M. (2012). Hydrodynamics of vegetated channels. *Journal of Hydraulic Research*, 50(3):262–279.

Nepf, H. M. and Vivoni, E. (2000). Flow structure in depth-limited, vegetated flow. *Journal of Geophysical Research: Oceans*, 105(C12):28547–28557.

Niewerth, S., Koll, K., Asher, S., Moltchanov, S., and Shavit, U. (2016). Methods to assess drag force in flow through irregularly arranged roughness elements. In *River Flow 2016: Iowa City, USA, July 11-14, 2016*, pages 365–371. CRC Press.

Niewerth, S., Núñez-González, F., Lull, T., and Lempa, S. (2021). A novel shear plate for direct measurements of bottom shear stress induced by a model ship propeller. *Publications of the Institute of Geophysics, Polish Academy of Sciences; Geophysical Data Bases, Processing and Instrumentation*, 434(E-11):47–49.

Nikora, V. and Goring, D. (2000). Flow turbulence over fixed and weakly mobile gravel beds. *Journal of Hydraulic Engineering*, 126(9):679–690.

Nikora, V., Goring, D., McEwan, I., and Griffiths, G. (2001). Spatially averaged open-channel flow over rough bed. *Journal of Hydraulic engineering*, 127(2):123–133.

Nikora, V., Koll, K., McEwan, I., McLean, S., and Dittrich, A. (2004). Velocity distribution in the roughness layer of rough-bed flows. *Journal of Hydraulic Engineering*, 130(10):1036–1042.

Nikora, V., McEwan, I., McLean, S., Coleman, S., Pokrajac, D., and Walters, R. (2007a). Double-averaging concept for rough-bed open-channel and overland flows: Theoretical background. *Journal of Hydraulic Engineering*, 133(8):873–883.

Nikora, V., McLean, S., Coleman, S., Pokrajac, D., McEwan, I., Campbell, L., Aberle, J., Clunie, D., and Koll, K. (2007b). Double-averaging concept for rough-bed open-channel and overland flows: Applications. *Journal of Hydraulic Engineering*, 133(8):884–895.

Nikora, V. I. and Goring, D. G. (1998). Adv measurements of turbulence: Can we improve their interpretation? *Journal of Hydraulic Engineering*, 124(6):630–634.

Nortek, A. (2018). The comprehensive manual for velocimeters. *Nortek AS: Rud, Norway*.

O'Briain, R. (2019). Climate change and european rivers: An eco-hydromorphological perspective. *Ecohydrology*, 12(5):e2099.

Palmer, M. A., Bernhardt, E., Allan, J., Lake, P. S., Alexander, G., Brooks, S., Carr, J., Clayton, S., Dahm, C., Follstad Shah, J., et al. (2005). Standards for ecologically successful river restoration. *Journal of Applied Ecology*, 42(2):208–217.

Park, H. and Hwang, J. H. (2021). A standard criterion for measuring turbulence quantities using the four-receiver acoustic doppler velocimetry. *Frontiers in Marine Science*, 8:681265.

Park, J. H., Do Kim, Y., Park, Y. S., and Jung, D. G. (2019). Direct measurement of bed shear stress using adjustable shear plate over a wide range of froude numbers. *Flow Measurement and Instrumentation*, 65:122–127.

Parker, G. (2003). Persistence of sediment lumps in approach to equilibrium in sediment-recirculating flumes. In *XXX International Association of Hydraulic Research Congress, Thessaloniki, Greece*.

Perillo, M. M., Best, J. L., Yokokawa, M., Sekiguchi, T., Takagawa, T., and Garcia, M. H. (2014). A unified model for bedform development and equilibrium under unidirectional, oscillatory and combined-flows. *Sedimentology*, 61(7):2063–2085.

Petryk, S. and Bosmajian, G. (1975). Analysis of flow through vegetation. *Journal of the Hydraulics Division*, 101(7):871–884.

Poggi, D., Ridolfi, L., and Katul, G. (2007). Mean flow inside aquatic vegetation on gentle complex beds: Experiments and analytical models. In *Proceedings of the 32nd IAHR World Congress (Venice, 2007)*, volume 32, page 151.

Pope, S. B. and Pope, S. B. (2000). *Turbulent flows*. Cornell University, New York.

Popiel, C. and Wojtkowiak, J. (1998). Simple formulas for thermophysical properties of liquid water for heat transfer calculations (from 0 c to 150 c). *Heat Transfer Engineering*, 19(3):87–101.

Przyborowski, Ł., Łoboda, A. M., and Bialik, R. J. (2018). Experimental investigations of interactions between sand wave movements, flow structure, and individual aquatic plants in natural rivers: A case study of potamogeton pectinatus l. *Water*, 10(9):1166.

R2019b (2019). Matlab version: 9.13.0 (r2019b).

Rebai, D., Berzi, D., Ballio, F., and Matousek, V. (2022). Experimental comparison of inclined flows with and without intense sediment transport: Flow resistance and surface elevation. *Journal of Hydraulic Engineering*, 148(12):04022026.

Recking, A., Frey, P., Paquier, A., Belleudy, P., and Champagne, J.-Y. (2008). Feedback between bed load transport and flow resistance in gravel and cobble bed rivers. *Water Resources Research*, 44(5):W05412.

Richardson, D. M., Holmes, P. M., Esler, K. J., Galatowitsch, S. M., Stromberg, J. C., Kirkman, S. P., Pyšek, P., and Hobbs, R. J. (2007). Riparian vegetation: degradation, alien plant invasions, and restoration prospects. *Diversity and distributions*, 13(1):126–139.

Rowiński, P. M., Västilä, K., Aberle, J., Järvelä, J., and Kalinowska, M. B. (2018). How vegetation can aid in coping with river management challenges: A brief review. *Ecohydrology & Hydrobiology*, 18(4):345–354.

Schindler, R. J. and Robert, A. (2005). Flow and turbulence structure across the ripple–dune transition: an experiment under mobile bed conditions. *Sedimentology*, 52(3):627–649.

Schoneboom, T. (2011). *Widerstand flexibler Vegetation und Sohlenwiderstand in durchströmten Bewuchsfeldern*. PhD thesis, Dissertation, Braunschweig, Technische Universität Braunschweig.

Schoneboom, T. and Aberle, J. (2009). Influence of foliage on drag force of flexible vegetation. In *33rd IAHR Congress, Vancouver, Canada, Papers on CD-Rom*.

Schoneboom, T., Aberle, J., and Dittrich, A. (2010). Hydraulic resistance of vegetated flows: Contribution of bed shear stress and vegetative drag to total hydraulic resistance. In *Proceedings of River Flow 2010, Braunschweig, Germany*, pages 269–276.

Schoneboom, T., Aberle, J., and Dittrich, A. (2011). *Spatial variability, mean drag forces, and drag coefficients in an array of rigid cylinders*, chapter in *Experimental Methods in Hydraulic Research*, pages 255–265. GeoPlanet: Earth and Planetary Sciences, Springer, Berlin, Springer.

Schoneboom, T., Aberle, J., Wilson, C. A., and Dittrich, A. (2008). Drag force measurements of vegetation elements. In *ICHE 2008. Proceedings of the 8th International Conference on Hydro-Science and Engineering, September 9-12, 2008, Nagoya, Japan*.

Shumway, R. H., Stoffer, D. S., and Stoffer, D. S. (2000). *Time series analysis and its applications*, volume 3. Springer.

Simons, D. and Richardson, E. (1961). Forms of bed roughness in alluvial channels. *Journal of the Hydraulics Division*, 87(3):87–105.

Simons, D. B. and Richardson, E. V. (1966). *Resistance to flow in alluvial channels*, chapter in Geological Survey Professional Paper (422-J). US Government Printing Office.

Simons, D. B., Richardson, E. V., and Nordin, C. F. (1965). *Bedload equation for ripples and dunes*. USGS. Washington (Geological Survey Professional Paper, 462-H).

Smith, J. D. and McLean, S. (1977). Spatially averaged flow over a wavy surface. *Journal of Geophysical Research*, 82(12):1735–1746.

Song, T. and Chiew, Y. (2001). Turbulence measurement in nonuniform open-channel flow using acoustic Doppler velocimeter (ADV). *Journal of Engineering Mechanics*, 127(3):219–232.

Song, T., Chiew, Y., and Chin, C. (1998). Effect of bed-load movement on flow friction factor. *Journal of Hydraulic Engineering*, 124(2):165–175.

Southard, J. B. and Boguchwal, L. A. (1990). Bed configuration in steady unidirectional water flows; part 2, synthesis of flume data. *Journal of Sedimentary Research*, 60(5):658–679.

Stapleton, K. and Huntley, D. (1995). Seabed stress determinations using the inertial dissipation method and the turbulent kinetic energy method. *Earth Surface Processes and Landforms*, 20(9):807–815.

Tal, M. and Paola, C. (2007). Dynamic single-thread channels maintained by the interaction of flow and vegetation. *Geology*, 35(4):347–350.

Tang, C., Yi, Y., Jia, W., and Zhang, S. (2020). Velocity and turbulence evolution in a flexible vegetation canopy in open channel flows. *Journal of Cleaner Production*, 270:122543.

Tang, H., Hao, W., Liang, D., Lv, S., and Yan, L. (2013). Incipient motion of sediment in the presence of emergent rigid vegetation. *Journal of Hydro-Environment Research*, 7(3):202–208.

Tang, X. and Knight, D. W. (2006). Sediment transport in river models with overbank flows. *Journal of Hydraulic Engineering*, 132(1):77–86.

Tanino, Y. and Nepf, H. M. (2008a). Laboratory investigation of mean drag in a random array of rigid, emergent cylinders. *Journal of Hydraulic Engineering*, 134(1):34–41.

Tanino, Y. and Nepf, H. M. (2008b). Lateral dispersion in random cylinder arrays at high Reynolds number. *Journal of Fluid Mechanics*, 600:339–371.

Termini, D. (2015). Flexible vegetation behaviour and effects on flow conveyance: experimental observations. *International Journal of River Basin Management*, 13(4):401–411.

Tinoco, R. O. and Coco, G. (2016). A laboratory study on sediment resuspension within arrays of rigid cylinders. *Advances in Water Resources*, 92:1–9.

Tinoco, R. O. and Cowen, E. A. (2013). The direct and indirect measurement of boundary stress and drag on individual and complex arrays of elements. *Experiments in Fluids*, 54:1–16.

Unsworth, C., Parsons, D., Hardy, R., Reesink, A., Best, J., Ashworth, P., and Keevil, G. (2018). The impact of nonequilibrium flow on the structure of turbulence over river dunes. *Water Resources Research*, 54(9):6566–6584.

Van den Berg, J. and van Gelder, A. (1993). A new bedform stability diagram, with emphasis on the transition of ripples to plane bed in flows over fine sand and silt. *Spec. Publs. Int. Ass.Sediment*, 17:11–21.

Van der Mark, C. (2009). *A semi-analytical form drag model for river bedforms.* PhD thesis, University of Twente, Netherlands.

Van der Mark, C. and Blom, A. (2007). A new and widely applicable tool for determining the geometric properties of bedforms. *Civil Eng. & Man. Res. Reports 2007R-003/WEM-002*, (1568-4652).

van Dijk, W. M. (2013). *Meandering rivers: feedbacks between channel dynamics, floodplain and vegetation.* PhD thesis, Utrecht University.

van Rijn, L. C. (1984a). Sediment transport, part I: bed load transport. *Journal of Hydraulic Engineering*, 110(10):1431–1456.

van Rijn, L. C. (1984b). Sediment transport, part III: bed forms and alluvial roughness. *Journal of Hydraulic Engineering*, 110(12):1733–1754.

Vanoni, V. A. and Brooks, N. H. (1957). Laboratory studies of the roughness and suspended load of alluvial streams. Technical Report Report E-68, Sedimentation Laboratory, California Institute of Technology.

Vargas-Luna, A., Crosato, A., and Uijttewaal, W. S. (2015). Effects of vegetation on flow and sediment transport: comparative analyses and validation of predicting models. *Earth Surface Processes and Landforms*, 40(2):157–176.

Vargas-Luna, A., Duró, G., Crosato, A., and Uijttewaal, W. (2019). Morphological adaptation of river channels to vegetation establishment: A laboratory study. *Journal of Geophysical Research: Earth Surface*, 124(7):1981–1995.

Västilä, K. and Järvelä, J. (2014). Modeling the flow resistance of woody vegetation using physically based properties of the foliage and stem. *Water Resources Research*, 50(1):229–245.

Västilä, K. and Järvelä, J. (2018). Characterizing natural riparian vegetation for modeling of flow and suspended sediment transport. *Journal of Soils and Sediments*, 18:3114–3130.

Venditti, J. G. (2007). Turbulent flow and drag over fixed two-and three-dimensional dunes. *Journal of Geophysical Research: Earth Surface*, 112(F4).

Venditti, J. G. and Bennett, S. J. (2000). Spectral analysis of turbulent flow and suspended sediment transport over fixed dunes. *Journal of Geophysical Research: Oceans*, 105(C9):22035–22047.

Venditti, J. G., Church, M., and Bennett, S. J. (2005). On the transition between 2d and 3d dunes. *Sedimentology*, 52(6):1343–1359.

Vogel, S. (1994). *Life in moving fluids: the physical biology of flow-revised and expanded second edition*. Princeton University Press.

Voulgaris, G. and Trowbridge, J. H. (1998). Evaluation of the acoustic doppler velocimeter (ADV) for turbulence measurements. *Journal of Atmospheric and Oceanic Technology*, 15(1):272–289.

Wahl, T. L. (2000). Analyzing ADV data using WinADV. In *in Proceedings Building Partnerships - Joint Conference on Water Resource Engineering and Water Resources Planning and Management*.

Wang, X., Gualtieri, C., and Huai, W. (2023). Grain shear stress and bed-load transport in open channel flow with emergent vegetation. *Journal of Hydrology*, 618:129204.

Wong, M. and Parker, G. (2006). Reanalysis and correction of bed-load relation of meyer-peter and müller using their own database. *Journal of Hydraulic Engineering*, 132(11):1159–1168.

Wu, W. and He, Z. (2009). Effects of vegetation on flow conveyance and sediment transport capacity. *International Journal of Sediment Research*, 24(3):247–259.

Xu, Y. and Nepf, H. (2020). Measured and predicted turbulent kinetic energy in flow through emergent vegetation with real plant morphology. *Water Resources Research*, 56(12):e2020WR027892.

Yager, E. and Schmeeckle, M. (2013). The influence of vegetation on turbulence and bed load transport. *Journal of Geophysical Research: Earth Surface*, 118(3):1585–1601.

Yalin, M. S. and Karahan, E. (1979). Steepness of sedimentary dunes. *Journal of the Hydraulics Division*, 105(4):381–392.

Yalin, S. (1964). On the average velocity of flow over a movable bed. *La Houille Blanche*, (1):45–51.

Yang, J., Chung, H., and Nepf, H. (2016). The onset of sediment transport in vegetated channels predicted by turbulent kinetic energy. *Geophysical Research Letters*, 43(21):11–261.

Yang, J. Q., Kerger, F., and Nepf, H. M. (2015). Estimation of the bed shear stress in vegetated and bare channels with smooth beds. *Water Resources Research*, 51(5):3647–3663.

Yang, J. Q. and Nepf, H. M. (2018). A turbulence-based bed-load transport model for bare and vegetated channels. *Geophysical Research Letters*, 45(19):10–428.

Yang, J. Q. and Nepf, H. M. (2019). Impact of vegetation on bed load transport rate and bedform characteristics. *Water Resources Research*, 55(7):6109–6124.

Yen, B. C. (2002). Open channel flow resistance. *Journal of Hydraulic Engineering*, 128(1):20–39.

Zanke, U. and Roland, A. (2021). On ripples − A boundary layer theoretical definition. *Water*, 13(7):892.

Zinke, P. (2012). Application of porous media approach for vegetation flow resistance. In *Proceedings of River Flow 2012 San Jose (Costa Rica) 5-7 September*, pages 301–310.

Zonta, F., Marchioli, C., and Soldati, A. (2012). Modulation of turbulence in forced convection by temperature-dependent viscosity. *Journal of Fluid Mechanics*, 697:150–174.